Light Detectors for the XENON100 and XENON1T Dark Matter Search Experiments

Dissertation

zur

Erlangung der naturwissenschaftlichen Doktorwürde

(Dr. sc. nat.)

vorgelegt der Mathematisch-naturwissenschaftlichen Fakultät

der

Universität Zürich

von

Annika Behrens

aus

Deutschland

Promotionskomitee:

Prof. Dr. Laura Baudis

Prof. Dr. Marc Schumann

Dr. Alfredo Ferella

Zürich, 2014

Abstract

One of the most exciting mysteries of modern physics is that of dark matter. While there is a multitude of evidence for its existence, its nature remains unknown. Today, numerous experiments search for weakly interacting massive particles (WIMPs) which could be the constituents of dark matter. Among these is the XENON project. XENON uses a time projection chamber filled with liquid xenon as target, detecting both the prompt scintillation light and the ionisation charge that is created when a particle such as a WIMP scatters off a xenon atom.

The XENON100 detector has been taking science data since 2010, leading to the most stringent exclusion limit on spin-independent WIMP-nucleon interactions at the time of writing this thesis, with a minimum of $2 \cdot 10^{-45}$ cm^2 at 55 GeV/c^2. Its successor, XENON1T is currently being constructed and expected to begin commissioning by the end of 2014. Using 2.2 t of liquid xenon as target it aims on improving upon the sensitivity of XENON100 by two orders of magnitude, with a background expectation of less than one event in a total exposure of 2 t·y.

The focus of this thesis lies on the photomultiplier tubes (PMTs) that are used in the XENON100 detector and those that will be used in XENON1T. While XENON100 had already been fully assembled before the start of this PhD project, its 242 PMTs have been subject to a weekly calibration with LED light throughout the entire time the detector was taking science data. This allowed to monitor and ensure the stability of various PMT parameters, namely the gain and the dark count rate. The results of these calibrations and their impact on the science run of 2011/2012 are presented in Chapter 5.

For XENON1T a new, larger (3 inch in diameter) type of PMT will be used. To be used in this experiment a PMT must fulfil a multitude of requirements: It must be able to detect single photons with good resolution as well as large light signals of several

tens of thousands of photons, which can, during calibration of the detector, occur at a repetition rate of several hundred hertz. At the same time it must be stable over long time periods at the conditions of a cryogenic time projection chamber. It is also necessary that the radioactive contamination of the PMT contributes as little as possible to the overall background of the experiment, and that it does not introduce too much heat into the detector.

The PMT has therefore been thoroughly tested, including a long-time stability test in liquid xenon and a test with several cooling cycles. A description of these tests and the results can be found in Chapter 6. The PMT has been found to be suitable for XENON1T and will now be used to instrument the detector.

Some of the properties of the PMT behaviour do not only originate from the PMT itself, but also from its voltage divider base. The development of a circuit layout for this base that is optimised for the requirements of XENON1T is described in Chapter 7. The main difficulty was to find a compromise between linearity, which can be improved by increasing the base current and using additional capacitors, power dissipation and the total amount of material, which has to be minimised in order to not introduce additional radioactive background. The selection of the materials that will be used for the bases in XENON1T is also presented.

Contributions to the analysis of the electromagnetic background spectrum of the XENON100 experiment are also a part of this thesis. The spectrum has been compared to data from Monte Carlo simulations based on the known radioactivity of the detector materials, showing good agreement. While studying the background, the need for an additional position-dependent correction of the light signals proportional to the ionisation charge was also discovered. This is described in Chapter 3.

Zusammenfassung

Dunkle Materie ist eines der spannendsten Rätsel der modernen Physik. Obwohl es zahlreiche Hinweise auf ihre Existenz gibt, ist ihre Beschaffenheit noch völlig unbekannt. Es gibt heute verschiedenste Experimente die nach schwach wechselwirkenden massiven Teilchen (weakly interacting massive particles, WIMPs) suchen, aus welchen die dunkle Materie bestehen könnte. Eines dieser Experimente ist das XENON-Projekt. XENON verwendet eine mit flüssigem Xenon gefüllte Zeitprojektionskammer und beobachtet sowohl das Szintillationslicht als auch die Ionisationsladung die entstehen wenn ein Teilchen, beispielsweise ein WIMP, an einem Xenonatom streut.

Der XENON100-Detektor nimmt seit 2010 Daten, die zu einem Ausschlusslimit für die spinabhängige Streuung von WIMPs an Kernen geführt haben. Zum Zeitpunkt des Schreibens dieser Arbeit ist dieses das stärkste unter allen experimentellen Ergebnissen, mit einem Minimum von $2 \cdot 10^{-45}$ cm^2 bei 55 GeV/c^2. XENON1T, der Nachfolger von XENON100, wird zur Zeit gebaut und soll ab 2014 in Betrieb genommen werden. Mit 2.2 t flüssigem Xenon als Detektormaterial wird eine Verbesserung der Sensitivität um zwei Grössenordnungen gegenüber XENON100 angestrebt. Der erwartete Untergrund soll dabei auf weniger als ein Ereignis während der Gesamtexposition von 2 t·y reduziert werden.

Der Schwerpunkt der vorliegenden Arbeit liegt auf den Photoelektronenvervielfachern (photomultiplier tubes, PMTs), welche in XENON100 verwendet werden, sowie jenen, die in XENON1T eingesetzt werden sollen. Zwar war der XENON100 Detektor zu Beginn dieses Projekts bereits vollständig zusammengebaut, jedoch wurden seine 242 PMTs während der gesamten Messzeit wöchentlich mit LED-Licht kalibriert. Dies erlaubte die Überwachung der Stabilität verschiedener PMT-Parameter, insbesondere des Verstärkungsfaktors und des Dunkelstroms. Die Ergebnisse dieser Kalibrierungen und

ihre Bedeutung für die Messperiode 2011/2012 werden in Kapitel 5 vorgestellt.
Für XENON1T wird ein neuer, grösserer PMT-Typ mit einem Durchmesser von 3 inch verwendet werden. Um in diesem Experiment einsetzbar zu sein muss er eine Vielzahl von Bedingungen erfüllen: Er muss einzelne Photonen mit guter Auflösung detektieren können, aber auch Lichtsignale mit mehreren zehntausend Photonen, welche im Zuge von Kalibrierungen auch mit einer Wiederholungsrate von mehreren hundert Hertz auftreten können. Gleichzeitig muss die PMT über lange Zeiträume in der Umgebung der kryogenen Zeitprojektionskammer stabil bleiben. Es ist ausserdem notwendig, dass die PMT so wenig wie möglich zum Gesamtuntergrund im Experiment beiträgt. Zudem darf sie nur sehr wenig Wärme erzeugen.
Die PMT ist daher sehr gründlich getestet worden, inklusive eines Langzeitstabilitätstests in flüssigem Xenon und einem Test mit mehreren Kühlzyklen. Eine Beschreibung dieser Tests und ihrer Ergebnisse findet sich in Kapitel 6. Die PMT hat sich als für den Einsatz in XENON1T geeignet erwiesen und wird nun dort auch verwendet werden.
Einige Punkte des PMT-Verhaltens hängen nicht nur von der PMT selber, sondern auch von ihrer Spannungsteilerbasis ab. Die Entwicklung eines Schaltplans für diese Basis, welches in Hinblick auf die Bedingungen in XENON1T optimiert ist, wird in Kapitel 7 beschrieben. Die Hauptschwierigkeit war dabei, einen Kompromiss zwischen der Linearität, welche sich durch einen höheren Basisstrom und den Einsatz von zusätzlichen Kondensatoren verbessern lässt, der Leistungsabgabe sowie der Gesamtmaterialmenge, welche zwecks Reduzierung des radioaktiven Untergrundes möglichst klein bleiben sollte. Die Auswahl der geeigneten Materialien für diese Basis wird ebenfalls vorgestellt.
Einen weiteren Teil dieser Arbeit stellen Beiträge zur Analyse des elektromagnetischen Untergrundspektrum im XENON100-Experiment dar. Dieses Spektrum wurde mit Daten von Monte-Carlo-Simulationen, welche auf der bekannten Radioaktivität der einzelnen Detektorkomponenten basieren, mit guter Übereinstimmung verglichen. Im Zuge dieser Untersuchung wurde auch die Notwendigkeit einer zusätzlichen positionsabhängigen Korrektur der Lichtsignale, welche proportional zur Ionisationsladung sind, entdeckt. Dies ist in Kapitel 3 beschrieben.

Contents

Chapter 1

Dark Matter

1.1 Evidence for Dark Matter

The term "dark matter" was coined by Swiss physicist Fritz Zwicky who observed the velocities of the galaxies in the Coma cluster. He used the virial theorem to estimate the total mass in the cluster and compared it to the mass estimate derived from the luminosities of the galaxies. The two values did not agree - the gravitation from the luminous matter alone would not be enough to keep the cluster together given the observed velocity distribution. There had to be some other type of matter that was not luminous: the dark matter [1] [2]. In the following years, similar observations were made for other clusters, such as the Virgo cluster [3] or the Local Group [4].
Additional evidence for the existence of dark matter came from studies of the rotation curves of spiral galaxies [5] [6]. From the distribution of the luminous matter alone it was expected that the velocities of stars outside the centre of the galaxy would follow Kepler's laws. Instead, the rotation curves stayed flat far beyond the visible borders of the galaxies, hinting to the existence of a dark matter halo [7].
One of the most recent indications for dark matter is the cluster merger 1E0657-558, where the distribution of the X-ray emissions of the hot gas, which holds the majority of the baryonic mass, did not match the distribution of the mass as obtained from weak lensing maps [8]. This discrepancy is often seen as direct proof for the existence of particle dark matter, because, unlike the previous observations, it can not be explained by modifications to the theory of gravitation, such as MOND (Modified Newtonian Dynamics [9]).

The total amount of dark matter in the universe can be derived from studies of the cosmic microwave background (CMB). Such measurements have been performed by COBE [10], WMAP [11] and most recently by the Planck experiment [12]. According to these measurements the baryonic matter accounts for only $\sim 5\%$ of the total energy density of the universe, while $\sim 25\%$ come from dark matter and the other $\sim 70\%$ are dark energy. Despite the amount of evidence for the existence of dark matter, its nature is still unknown. In order to fit the observations, a dark matter particle could interact only gravitationally and possibly weakly with other matter. Its lifetime would have to be stable compared to the age of the universe. Such a particle is generally referred to as a weakly interacting massive particle (WIMP). Due to their limited interaction, detection of WIMPs would be very difficult, but not impossible, as explained in the following sections.

1.2 Direct Detection

Numerous experiments are searching for direct evidence for particle dark matter. There are three channels through which dark matter particles could be observed [13]: indirectly by looking for the signature of dark matter annihilation, directly by searching for interactions between a dark matter particle and a target mass, and through production in a particle accelerator.

WIMP annihilation could be detected by observing the annihilation products. Those could be γ-rays, neutrinos or antimatter [13]. In the first case two photons would be created at the energy of the WIMP's rest mass, that could be detected by satellites or Cherenkov telescopes such as Fermi [14], MAGIC [15] or H.E.S.S. [16]. If neutrinos were created as dark matter annihilation products they could be detected by neutrino telescopes such as IceCube [17] and ANTARES [18]. Antimatter could be seen by satellites such as PAMELA [19] or AMS [20]. No definite signal has been observed in the dark matter annihilation channel to date.

Dark matter production could also be observed at colliders such as the Large Hadron Collider (LHC), where dark matter particles would show up in the form of missing momentum. So far only exclusion limits have been set in this channel, which are the strongest limits in the low-mass range where other experiments are less sensitive [21] [22].

1.2.1 Interaction Rate

The third possibility would be direct detection of a dark matter particle interacting with a target. The interaction rate for WIMP-nucleon scattering is given as

$$R = \sigma(E_{nr}, v) N_T \frac{\rho_0}{m_\chi} < v > . \tag{1.1}$$

$\sigma(E_{nr}, v)$ is the cross-section which depends on the recoil energy E_{nr} and the velocity v of the incoming WIMPs, N_T is the number of target nuclei, ρ_0 is the assumed WIMP density at the location of the Earth, m_χ is the WIMP mass and $< v >$ is the mean WIMP velocity.
The latter is derived assuming a galactic halo model and comparing galactic N-body simulations to data from rotation curve measurements. Results from different dark matter experiments are usually compared for a value of $\rho_0 = 0.3 \ \frac{\mathrm{GeV}}{\mathrm{cm}^3}$ [23].
In order to compare different experiments the interaction rate is usually given in its differential form normalised to units of $\frac{1}{\mathrm{kg \cdot keV \cdot d}}$ (differential rate unit dru) [24]. The differential rate is then given as

$$\frac{1}{M_T} \frac{dR}{dE_{nr}} = \frac{\rho_0}{m_T m_\chi} \frac{d\sigma(E_{nr}, v)}{dE_{nr}} < v >, \tag{1.2}$$

where M_T is the total mass of the target and m_T that of one target nucleus.
If the WIMP velocity follows a probability distribution $f(v)$, Eq. 1.2 can be written as

$$\frac{1}{M_T} \frac{dR}{dE_{nr}} = \frac{\rho_0}{m_T m_\chi} \int_{v_{min}}^{v_{esc}} v \cdot f(v) \frac{d\sigma(E_{nr}, v)}{dE_{nr}} dv. \tag{1.3}$$

For the WIMP velocity distribution a Maxwellian function [24] with a mean velocity of $v_0 = (220 \pm 20) \frac{\mathrm{km}}{\mathrm{s}}$ [25] is used which corresponds to the assumption of the WIMPs forming an isothermal sphere centered in the rest frame of the Galaxy. A Galilean transformation is necessary to account for the movement of the Earth in the Galaxy's rest frame. Because the Earth is orbiting around the sun this results in an annual modulation of the expected WIMP velocity [26] with an amplitude of $v_E = 30 \frac{\mathrm{km}}{\mathrm{s}}$ [27] which is used by some direct detection experiments to discriminate possible WIMP interactions from background events.
$v_{esc} = 544 \frac{\mathrm{km}}{\mathrm{s}}$ [28] is the escape velocity for WIMPs from the dark matter halo. $v_{min}(E_{nr})$

is the minimal velocity at which the energy E_{nr} can be transferred in WIMP-nucleus scattering:

$$v_{min}(E_{nr}) = \sqrt{\frac{m_n E_{nr}}{2\mu}}, \tag{1.4}$$

corresponding to 180° backscattering with $\mu = \frac{m_n m_\chi}{m_n + m_\chi}$ being the reduced WIMP-nucleon mass.

The cross-section $\sigma(E_{nr}, v)$ depends on how the WIMP couples to the quarks in the target nucleus. If one assumes axial-vector coupling the cross-section will depend on the spin (SD), while it is spin-independent (SI) for scalar coupling.

For scalar coupling the cross-section can be written as [23]

$$\frac{d\sigma^{SI}}{dE_{nr}} = \frac{m_n}{2\mu^2 v^2} F^2(E_{nr}) \sigma_0^{SI}. \tag{1.5}$$

$F(E_{nr})$ is a nuclear form factor. σ_0^{SI} is the cross-section in the limit of no energy transfer and given as

$$\sigma_0^{SI} = \lim_{E_{nr} \to 0} \sigma(E_{nr})^{SI} = \frac{4\mu^2}{\pi} (Z f_p + (A - Z) f_n)^2. \tag{1.6}$$

Z is the atomic number of the target nucleus, A is its atomic mass, and f_p and f_n are the proton and neutron particle density functions, which depend on the particular model that is used. It is $f_p \approx f_n$ [23] which gives

$$\sigma_0^{SI} \approx \frac{4\mu^2}{\pi} (A f_p)^2. \tag{1.7}$$

The cross-section scales with A^2, which makes heavier target materials, such as xenon, so attractive. Because the exact value of f_p is model dependant the cross section is usually normalised to the cross-section of a WIMP with a single proton $\sigma_p^{SI} = \frac{4\mu_p^2}{\pi} f_p^2$:

$$\sigma_0^{SI} \approx A^2 \frac{\mu^2}{\mu_p^2} \sigma_p^{SI}, \tag{1.8}$$

where μ_p is the reduced WIMP-proton mass.

Using Eqs. 1.5 and 1.8 together with Eq. 1.3 the total interaction rate for SI coupling becomes

$$\frac{1}{M_T} \frac{dR}{dE_{nr}} = \frac{\rho_0 A^2}{2\mu_p^2 m_\chi^2} F^2(E_{nr}) \sigma_p^{SI} \int_{v_{min}(E_{nr})}^{v_{esc}} \frac{f(v)}{v} dv \tag{1.9}$$

For spin-dependent scattering one has to look more thoroughly at the nuclear structure. The cross-section in the limit of zero energy transfer is given as [29]

$$\sigma_0^{SD} = \frac{32}{\pi} G_F^2 m_r^2 (a_p < S_p > + a_n < S_n >)^2 \frac{J+1}{J}, \tag{1.10}$$

where G_F is the Fermi constant, a_p and a_n denote the spin-dependent coupling of the WIMP to the proton and neutron, respectively, $< S_p >$ and $< S_n >$ are the spin content of protons and neutrons in the nucleus and J is the spin of the nucleus. Because the coupling of the WIMP to the proton can no longer be assumed identical to that of the WIMP to the neutron, normalisation is done once assuming the WIMP would only couple to protons and once assuming it would only couple to neutrons. The nuclear form factor becomes also more complicated and highly model dependent in the case of axial-vector coupling.

Direct detection experiments generally define an energy seach region $[E_{min}, E_{max}]$ in which all events are counted. This is then compared to the expected number of interactions within this region for a given model:

$$N(m_\chi, \sigma) = TM \int_{E_{min}}^{E_{max}} \frac{dR}{dE_{nr}} dE_{nr} \tag{1.11}$$

where T is the total measurement time, M is the total target mass, and σ can be either σ_p^{SI}, σ_p^{SD} or σ_n^{SD}. The result is then typically shown as either a discovery (in case of observation) or an exclusion region (in case of non-observation) in the (m_χ,σ) space which allows to easily compare the findings of different experiments.

1.2.2 Direct Dark Matter Search Experiments

Today there are several ongoing direct dark matter detection experiments, looking for either heat, scintillation or ionisation or a combination of these as evidence for a WIMP interaction in the target material. A WIMP signal could be found in the form of the annual modulation of the interaction rate as the Earth orbits the sun, leading to a modulation in the WIMP velocity.

Such a signal modulation has been observed by the DAMA/LIBRA experiment [30], which is looking for scintillation in NaI crystals, and the CoGeNT experiment [31], which is looking for ionisation with germanium detectors. These findings do however not agree with

the results of other experiments.
The use of more than one observation channel allows to discriminate between nuclear recoils, as they would occur in WIMP interactions, and electronic recoils, which stem from other background radiation. Two experiments that are detecting ionisation and phonons simultaneously are CDMS and EDELWEISS. Both have put strong exclusion limits for spin-independent WIMP-nucleon interactions [32] [33] [34], although CDMS has recently also observed a signal that would be compatible with a low-mass WIMP [35].
An experiment detecting both phonons and scintillation is CRESST [36]. It uses $CaWO_4$ crystals, which offers the possibility to use the different nuclear recoil signatures of the three elements to further constrain the mass and cross-section of a WIMP. CRESST has seen a signal above the expected background, which however could also stem from a sputtering effect in the copper clamps. The clamp material has therefore now been changed in a new run to test this hypothesis.
Another group of single-channel experiments is based on bubble chambers, such as PICASSO [37], SIMPLE [38] or COUPP [39].
Many direct detection experiments use liquid noble gases as target material, observing either only the scintillation light (e. g. XMASS [40], DEAP-3600 [41], MiniCLEAN [42]) or the combination of scintillation and ionisation (e. g. XENON [43] [44], ZEPLIN [45], LUX [46], DarkSide [47]). The advantage of using liquid noble gases is that the size of the detectors is easily scalable. One of these experiments, XENON, is the topic of this thesis and will be described in detail in Chapter 2.

Chapter 2

The XENON Dark Matter Search Project

The XENON100 experiment has been taking science data since 2010, leading to the currently most stringent exclusion limits for spin-independent WIMP-nucleon coupling for WIMPs with a mass of 55 GeV/c^2 down to $2 \cdot 10^{-45}$cm^2 [43]. Like its predecessor, XENON10, it is located in the Laboratori Nazionali de Gran Sasso (LNGS) underground laboratory in Italy, which shields the detector from cosmic radiation with 1400 m of rock, equivalent to 3700 m of water.
In this chapter the detector set-up is briefly described (more information can be found in [48]) and the main results [43] [44] of the 225 live days science run are presented. The chapter is concluded with a short section on the next-generation detectors XENON1T and DARWIN.
The work described here is that of the whole XENON collaboration. I was involved in detector operation and data analysis. Some of the analysis that I performed is detailed in Chapter 3. The analysis of the weekly calibration of the XENON100 PMTs I performed can be found in Chapter 5.

2.1 Detection Principle

The XENON100 experiment makes use of a double-phase (liquid-gas) xenon time projection chamber (TPC) for the detection of both scintillation light and ionisation charge to

identify WIMP candidates. A schematic drawing of this principle is shown in Fig. 2.1. When a WIMP scatters off a xenon nucleus in the TPC volume the xenon gets ionised and excited. An exited xenon atom can form an excimer together with a surrounding xenon atom, which will then emit scintillation light with a mean wavelength of 178 nm when decaying to the ground state [49]:

$$Xe^* + Xe \rightarrow Xe_2^* \tag{2.1}$$

$$Xe_2^* \rightarrow 2Xe + \gamma \tag{2.2}$$

Depending on the applied drift field, a part of the ionised atoms can recombine, leading to more excited atoms and consequently to further scintillation light:

$$Xe^+ + Xe \rightarrow Xe_2^+ \tag{2.3}$$

$$Xe_2^+ + e^- \rightarrow Xe^{**} + Xe \tag{2.4}$$

$$Xe^{**} \rightarrow Xe^* + heat \tag{2.5}$$

The remaining ionisation charge is drifted along the electric field in the TPC and extracted into the gas phase, where a second light signal, S2, is created proportionally to the ionisation charge. Both the S1 and the S2 signal are detected by two arrays of photomultiplier tubes (PMTs).
The ratio between S2 and S1 is smaller for nuclear recoils (caused by WIMPs or neutrons) than for electronic recoils (caused by beta or gamma background events) and allows for discrimination between signal and background [50].
The charge drift time, which is given by the time difference between the S1 and the S2 signal, is used for the determination of the interaction point along the z-axis of the detector. The x- and y-coordinates are derived from the lateral distribution of the measured S2 signal over the different PMTs of the top array. This 3-D position reconstruction of the event allows for fiducialisation of the detector volume to reduce background events that are more prominent towards the edges of the detector due to the self-shielding properties of the liquid xenon.

2.2 Detector Design

This section is based on [48].
The design of the XENON100 detector is shown in Fig. 2.2. The TPC itself contains

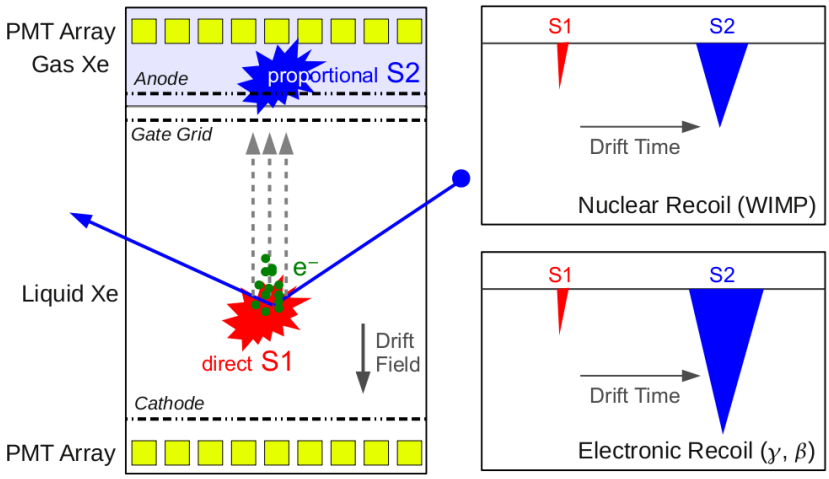

Figure 2.1: Detection principle of the XENON experiment. Drawing taken from [48].

62 kg of liquid xenon in a cylindrical volume with a height of 30.5 cm and 15.3 cm radius. It is confined by the cathode at the bottom, the anode at the top and polytetrafluoroethylene (PTFE) panels at the sides. Two arrays of PMTs are situated above the anode and below the cathode.

The cathode consists of a 2.5 mm thick low radioactivity stainless steel circular frame and a 75 µm thick stainless steel etched mesh. The hexagonal cell structure of the cathode mesh, with a cell opening of 5.35 mm, was selected for the uniform electrical drift field and the mechanical stability of the electrode. The cathode is mounted 17 mm above the bottom PMTs. It is supplied with a high voltage of up to – 16 kV. 12 mm below the cathode a 50 µm thick screening mesh is placed in order to protect the PMTs, which are set to voltages between – 700 and –900 V, from the electric field. The anode at the top of the TPC consists of a 125 µm thick mesh stacked between two grounded meshes. It is supplied with a high voltage of + 4.5 kV, creating an extraction field of $\sim$ 12 kV/cm, obtaining an extraction efficiency close to 100%. A homogeneous drift field along the TPC is created through 40 equidistant field shaping electrodes made of thin copper wires. A total of 242 Hamamatsu R8520 PMTs are used in the detector: 80 PMTs which have been selected for highest quantum efficiency ($\sim$ 32 %) in the bottom array and 98 PMTs in the top array. The remaining 64 PMTs are instrumenting the veto volume. The PMTs in the bottom array are arranged in a way that maximises light collection, as they are

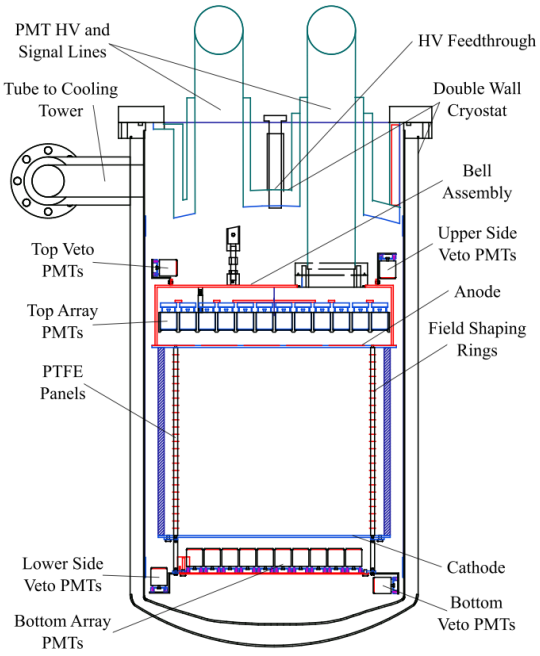

Figure 2.2: Design of the XENON100 detector. Drawing taken from [48].

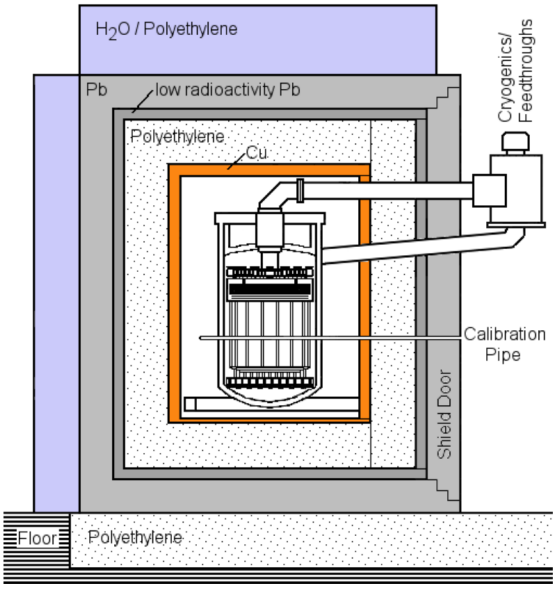

Figure 2.3: Shield design of the XENON100 detector. Drawing taken from [48].

crucial in detecting the (small) S1 signal. The PMTs in the top array on the other hand are arranged in a pattern optimised for position reconstruction, which is done on the larger S2 signal.

The TPC sits in a double-walled low-radioactivity 315Ti stainless steel cryostat, which is shielded (see Fig. 2.3) with 5 cm of OFHC copper, surrounded by 20 cm of polyethylene and 20 cm of lead, of which the innermost 5 cm consist of ancient lead with a contamination of 26 Bq/kg from ^{210}Pb. The whole shield sits on a 25 cm high base of polyethylene. On the top and on three sides the detector is additionally shielded by 20 cm of water.

The muon flux is already reduced by a factor of 10^6 by the shielding of the Gran Sasso rock, equivalent to 3700 m of water. To minimise contamination with radon the inner shield is constantly purged with nitrogen gas.

The XENON100 detector is operated at – 91 °C and 2.2 atm. The boil-off xenon gas lead to a cold-finger outside the detector shield (see Fig. 2.4) cooled by an Iwatani PC150

pulse tube refrigerator (PTR) with a cooling power of 300 W, where it condenses and is lead back into the inner detector vessel above the liquid level. The temperature of the liquefied xenon is finely controlled using electrical heaters between the cold-head of the PTR and the cold-finger, coupled to two temperature sensors above and below the heater. In case of emergency (e. g. power failures or failing of the PTR) the xenon can also be cooled with liquid nitrogen which is then led into a copper coil around the cold-finger. It has been shown that it is possible to keep the detector stable for 24 hours using only this emergency cooling system without human intervention.
In order to keep the xenon clean from electronegative impurities which would reduce the maximum drift time due to charge loss it is constantly recirculated and purified. Xenon is extracted from the liquid phase at the bottom of the detector at a rate of 4 liters per minute and pushed through a SAES MonoTorr PS3-MT3-R/N-1/2 high temperature zirconium getter before returning the cleaned gas into the bell above the top PMT array. The bell is used to control the liquid level just above the gate grid, similar to a diving bell. This mechanism allows to cover the outside of the TPC with $\sim$ 4 cm of liquid xenon in order to fill the volume used for active liquid xenon veto.

2.3 Data Acquisition

This section is based on [48].
A schematic drawing of the data acquisition (DAQ) system can be found in figure 2.5. All individual PMT signals are first amplified by a factor of 10 using Phillips 776 NIM amplifier modules and then digitised with CAEN VME V1724 Flash ADCs. These ADC modules provide 100 MHz sampling, 14 bit digital resolution over a full scale of 2.25 V, 40 MHz bandwidth and a 512 kB circular buffer for each channel, which allows data taking with virtually no dead time at the typical background event rate of 1 Hz.
All PMT signals are sampled continuously, but only stored in case of a trigger. For the science run reported in [51] the trigger signal has been created from the signals from the top PMTs and the 16 PMTs in the centre of the bottom array, which have been summed with linear Fan-In/Fan-Out modules. The combined signal has then been amplified, integrated with a time constant of 1 µs and shaped with an ORTEC 450 spectroscopy amplifier and

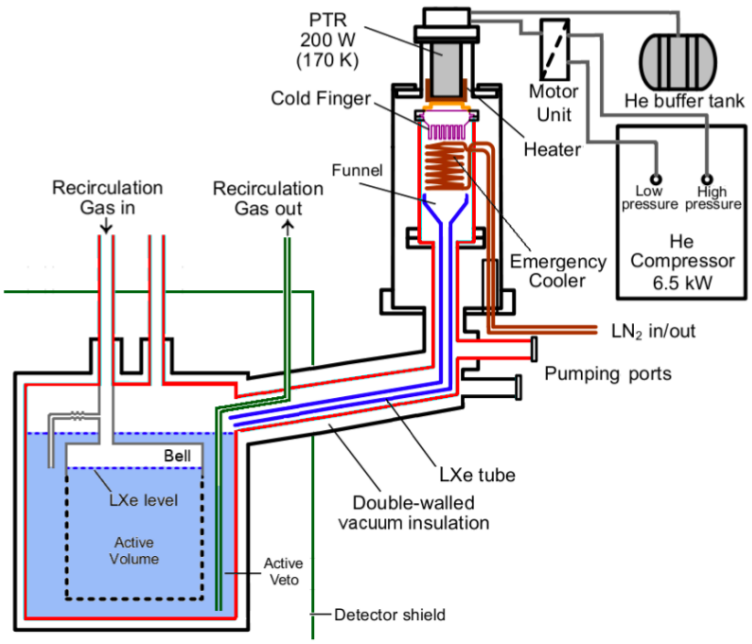

Figure 2.4: The cryogenic recirculation system of the XENON100 experiment. Drawing taken from [48].

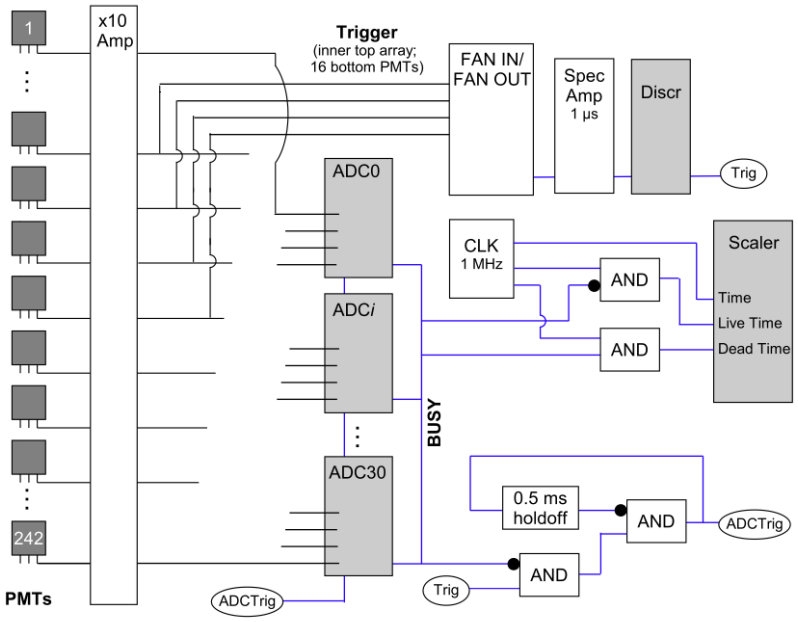

Figure 2.5: Schematics of the DAQ set-up in XENON100. Drawing taken from [48].

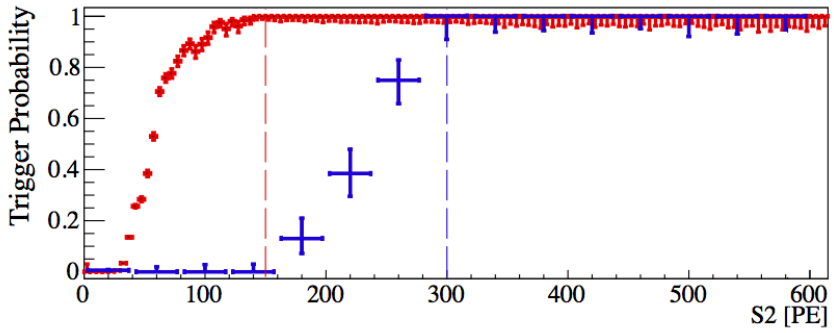

Figure 2.6: Directly measured trigger probability as a function of S2 signal size for run8 (blue) and run10 (red). Figure taken from [52].

finally been fed into a low threshold discriminator, which sent the digital trigger signal to all 31 ADC modules simultaneously. This method has been found to have an effective trigger probability of $> 99\%$ for S2 signals above 300 PE (Fig. 2.6).
After run8 the trigger has been improved. Every ADC generates now an analogue square output signal for every channel exceeding a threshold of ~ 0.5 PE. These signals are summed and integrated over 1 µs and fed into the low threshold discriminator that generates the trigger signal. This modification has been found to lead to an effective trigger probability of $> 99\%$ already for S2 signals above 150 PE (Fig. 2.6).
If data taking is triggered, the waveforms of all PMTs are stored into a custom indexed file format. 200 µs before and after the trigger position are saved, more than twice the maximum drift time in the detector of 176 µs at the drift field of 0.53 kV/cm in order to not loose any information of the event. Triggering is then inhibited for 500 µs after the recorded event to prevent any overlapping. A trigger hold-off is also used when the ADCs are busy or after a high energy veto. The high energy veto is used to restrict data taking to the low-energy region that is of interest for dark matter search, and is useful especially during calibration of the detector. It inhibits recording of events triggered by S1 signals which are identified by their narrow peak width. The total dead time during dark matter taking has been measured to be ~ 1 %.

When storing waveforms, on-board FPGAs are used for zero-length encoding (ZLE) in which only parts of the waveforms (in the following called subwaveforms) around peaks exceeding a certain threshold are saved together with their position in time. The thresh-

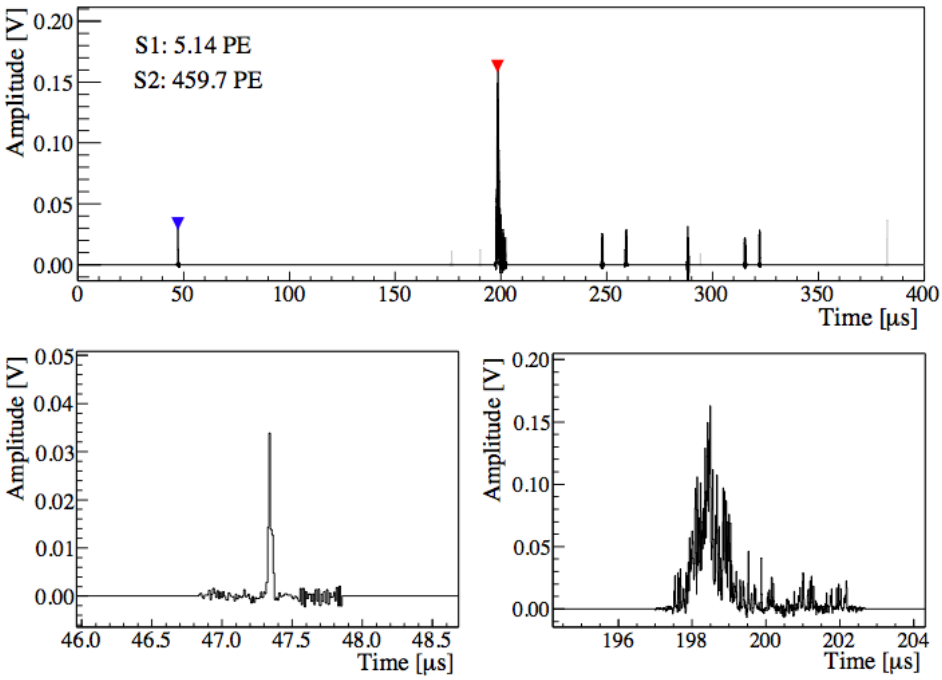

Figure 2.7: Example of the waveform of a low-energy event. The top figure shows the whole waveform. The S1 peak was found at $\sim$ 47 µs (lower left figure and marked blue in the top figure) and has a size of 5.1 photoelectrons. The S2 peak is at $\sim$ 200 µs consisting of 460 photoelectrons (lower right figure and marked red in the top figure). It is followed by S2 signals from single electrons. Figure taken from [48].

old is set for each channel individually depending on the noise level. For most PMTs it is set to 4 mV ($\sim$ 0.3 PE). This allows to decrease the size of the data files by a factor of > 10. For high-energy γ-sources calibration rates of up to 30 Hz are possible with this mode.

Further processing of the stored data is performed at a later stage, as discussed in section 2.4.

2.4 Data Analysis

2.4.1 Preprocessing

This section is based on [48].
The recorded raw data is processed off-line with the XENON Raw Data Processor (xerawdp) software, a ROOT [53] based C++ program. Each event consists of the subwaveforms of all 242 PMTs around the peaks within the 400 µs acquisition window with their position. In a first step the data is converted from ADC counts to volts. The baseline in every subwaveform is computed and the waveforms from all PMTs observing the TPC (ignoring malfunctioning PMTs, such as those which exhibit very high dark current) are combined into one total waveform (Fig. 2.7). The same is done with the veto channels. A low-pass filter is used for filtering out high-frequency noise and peak finding. The S2 signal candidates are identified first, considering all peaks surpassing a threshold of 10 mV for at least 600 ns where the average signal in the 210 ns before and afterwards has to be smaller than 25 % of the maximum height of the candidate peak. Afterpulses, S2 signals from single electrons and multiple scattering can lead to more than one S2 signal in the event. All peaks with a FWHM of at least 350 ns are considered as S2 candidates.
After identifying the S2 signal candidates the processor looks for S1 signals in the unfiltered waveform in the region before the first S2 peak candidate to exceed a threshold of 300 PE. All peaks with a height exceeding 3 mV ($\sim$ 0.3 PE) are considered, comparing them with their immediate surrounding to differentiate valid peak candidates from baseline fluctuations or electronic noise. The detection efficiency is 80 % for single photoelectrons, 95 % for double photoelectrons and 99 % for signals from three photoelectrons.
For every S1 and S2 peak candidate a variety of parameters such as their width, height, area, position and PMT coincidence level are calculated and stored in a ROOT tree. The position is also determined: the z component from the drift time and the position in the x-y plane from the hit pattern on the top PMT array (see Fig. 2.8). Three different methods are employed: one mimimising the χ^2-value comparing the hit pattern to Monte Carlo simulation results, one based on a support vector machine (SVM) and one using a neural network (NN), that have both been trained on simulation data. All three algorithms give consistent results, but the NN algorithm has been found to give the most homogeneous response and to agree best with the expectations from Monte Carlo simulations and is

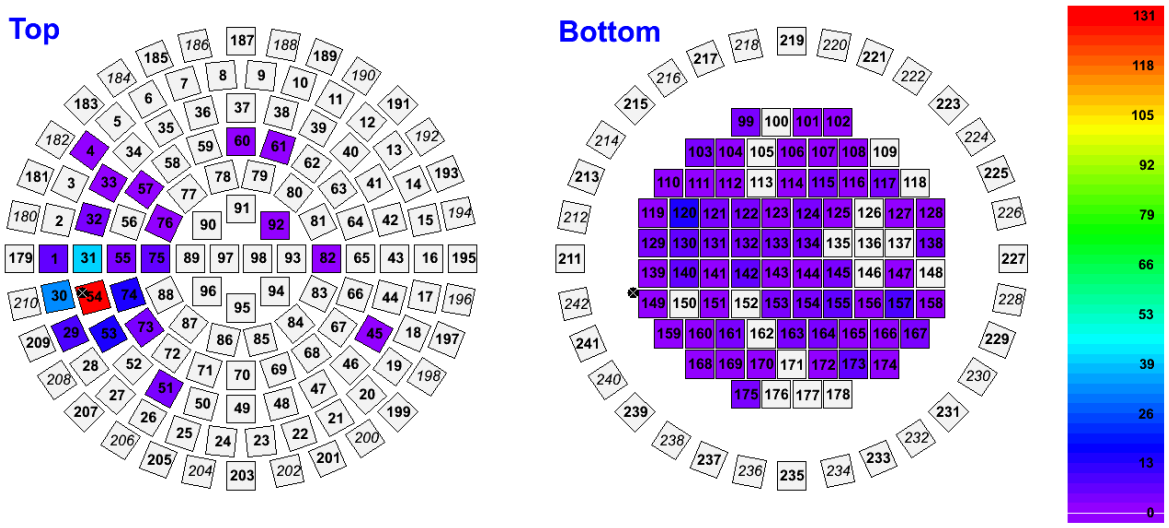

Figure 2.8: Hit pattern of the S2 signal of the event shown in 2.7. Indicated is the reconstructed position of the event as it was determined by the NN algorithm. Figure taken from [48].

therefore used as the primary position reconstruction method, while the other two are used for cross-checks.

2.4.2 Data Selection Criteria

Once the data has been processed, several selection criteria are used to ensure data quality. Here a short summary of some of the selection criteria is given. A more in-depth description can be found in [52].

To avoid dark counts or other noise being mistaken as an S1 signal the signal must be detected by at least two PMTs above a threshold of 0.35 PE within 20 ns. PMTs that are known for their especially high dark count rate are excluded from this coincidence count. Similarly, the largest contribution of a single PMT to the S2 peak has to be above the threshold of 150 PE.

Waveforms with a lot of noise are rejected by a cut based on the signal-to-noise ratio, requiring that the total integral of the waveform be determined mainly by the largest S1 and S2 peak.

A signal is also rejected if one PMT contributes more than 65 % to the total S2 signal.

WIMP events are expected to be single scatter events, while multiple scatters are possible for background events. To restrict the analysis to single scatter events both the number of S1 and S2 peaks are considered. Only one valid S1 peak within the waveform is allowed. However, it is possible that the S2 peak is followed by one or several small pulses, for example from single electrons. To exclude multiple scatters the cut therefore requires for the second largest S2 signal to be much smaller than the largest peak.
The width of the S2 peak is compared to the expectations from the drift time. If there is no good agreement, as it can happen for example if the event was produced in the gas phase of the TPC, the event is rejected.
As has been mentioned before, most background events are found at the border of the TPC. Using the reconstructed position of the event within the detector, only interactions within an inner volume are used for analysis. The exact cut is defined depending on the size of the intended fiducial volume.

2.4.3 Discrimination between electronic and nuclear recoils

Measuring scintillation light and ionisation charge simultaneously allows discrimination between electronic and nuclear recoils [50]. Electronic recoils refer to interactions of particles or radiation with the electrons of a xenon atom. They are background events which lead to large ionisation charges and often multiple scatters within the xenon target. Nuclear recoils on the other hand are interactions between a neutral particle such as a WIMP or a neutron and the xenon nucleus. They deposit only a small fraction of the energy in ionisation.
To distinguish between nuclear and electronic recoils, events are viewed in the so-called discrimination space (Fig. 2.9). The x-axis corresponds to the number of photoelectrons in the S1 signal and the y-axis denotes the discrimination parameter $log_{10}(S2/S1)$. Often the mean of the electronic recoil band as obtained from calibration (see Section 3.1) is subtracted from this discrimination parameter in order to obtain the so-called flattened discrimination space (Fig. 2.10).

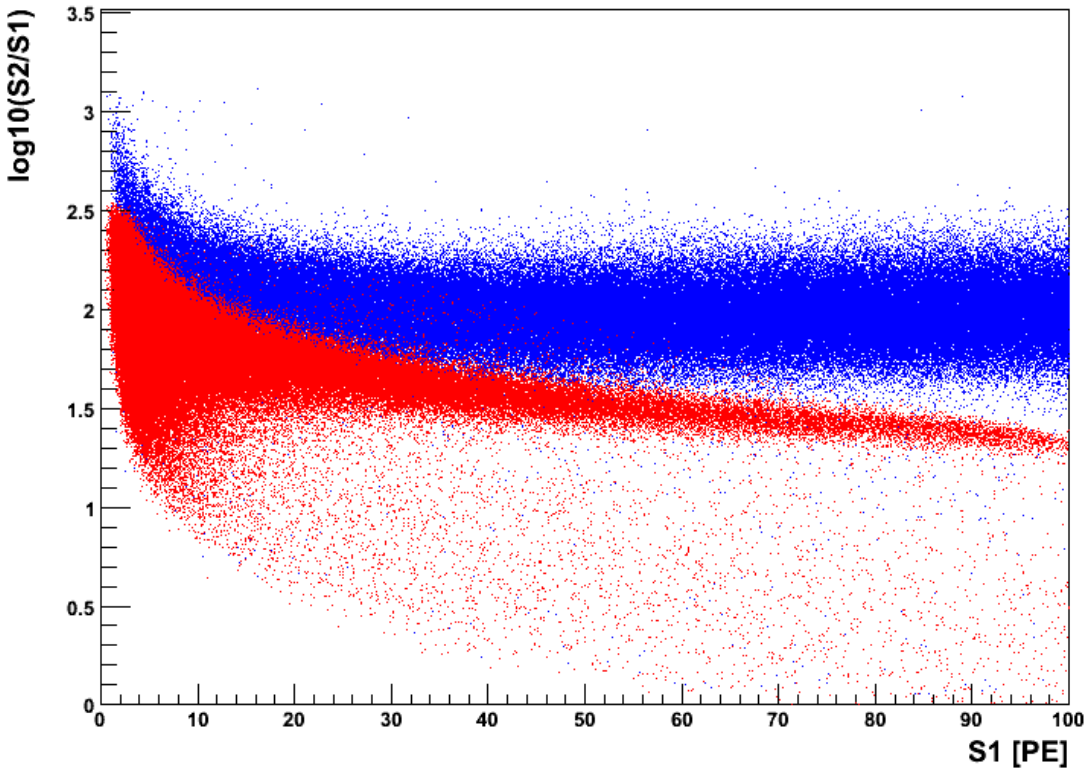

Figure 2.9: Distribution of the nuclear (red) and electronic (blue) recoil bands at the beginning of run10 in the discrimination space. Electronic recoil data is collected from ^{60}Co and ^{232}Th calibrations and nuclear recoil data is obtained from calibrations with AmBe. The recoil bands are explained in more detail in Section 3.1.

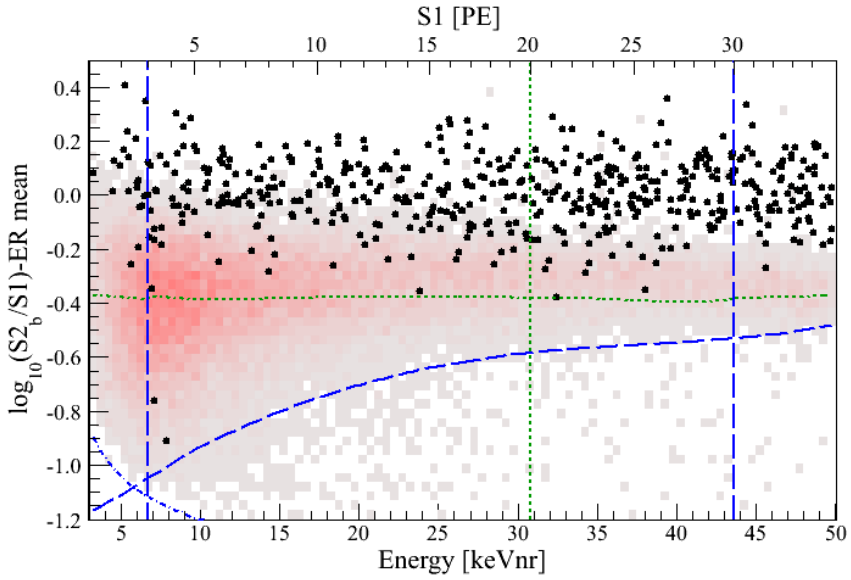

Figure 2.10: Event distribution in 225 live days after unblinding. Indicated is the WIMP search region in the flattened discrimination space, defined by a lower analysis threshold at 3 photoelectrons, a lower border along 97 % nuclear recoil acceptance (dashed blue), an upper border at 99.75 % electronic recoil rejection (dotted green) and an S2 threshold at 150 photoelectrons (dashed-dotted blue). There are two valid invents within this benchmark region. The red-grey histogram shows the nuclear recoil band obtained from the AmBe calibration. Figure taken from [43].

2.5 Results

Results of the XENON100 experiment have been published for three data taking periods of 11 [54], 100 [51] and 225 live days [43] [44]. Here the results of the longest run, run10, will be discussed, as described in [43].
Run10 was started in September 2010 and finished in May 2012. Neutron calibrations with an AmBe source have been performed at the start and again at the end of the data taking period. Additional calibrations with blue light from light-emitting diodes (LEDs) and with γ-radiation from ^{60}Co, ^{232}Th and ^{137}Cs have been performed on a weekly basis throughout the entire run.
Dark matter data was blinded in the region from 2 - 100 photoelectrons in S1. The benchmark WIMP search region was defined by the energy range from 3 - 20 photoelectrons (6.6 - 30.5 keV), by an upper 99.75 % electronic recoil rejection line in the discrimination space, a lower line at $\sim$ 97 % acceptance of the nuclear recoil band and a line corresponding to S2 signals larger than 150 photoelectrons (Fig. 2.10) [43]. A fiducial volume corresponding to 34 kg of liquid xenon has been used.
The background expectation from nuclear recoil events in this region was determined from Monte Carlo simulations, using the measured radioactivity from all detector materials. The number of expected events from electronic recoil in the search region was estimated by scaling the results from the ^{60}Co and ^{232}Th calibrations to the observed background outside the blinded region.
A total background of (1.0 ± 0.2) events was expected in the benchmark region, composed from (0.79 ± 0.16) electron recoil events and $0.17^{+0.12}_{-0.07}$ nuclear recoil events [43].
After unblinding there were two potential WIMP events observed (Fig. 2.10), one with a nuclear recoil energy of 7.1 keV and the other with 7.8 keV. This is compatible with the background-only hypothesis. A profile likelihood analysis yielded the most stringent WIMP exclusion limit for spin independent scattering for WIMP masses > 8 GeV/c^2 to date, down to a cross-section of $\sigma = 2 \cdot 10^{-45}$cm^2 for a WIMP mass of 55 GeV/c^2 at 90 % confidence level (Fig. 2.11). The existence of xenon isotopes with non-zero spin, namely ^{129}Xe (spin 1/2) with an abundance of 26.2 % and ^{131}Xe (spin 3/2) with an abundance of 21.8 % in the XENON100 detector allows also for a spin-dependent analysis. The nuclear shell model from [64] was used for the structure function. Analogously to the spin-independant analysis exclusion limits have been set, both for WIMP-proton cou-

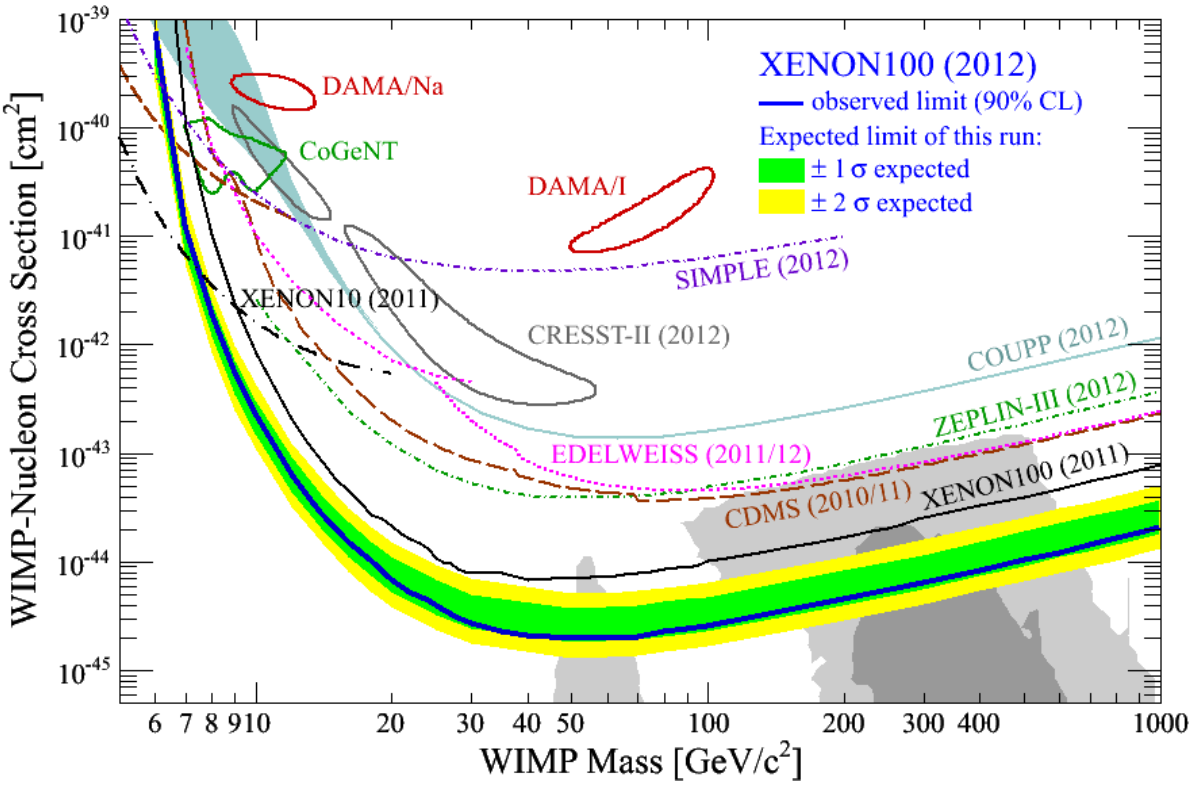

Figure 2.11: WIMP exclusion limit from 225 live days for SI coupling. XENON100 set the most stringent exclusion limit to date for spin-independent WIMP-nucleon scattering for WIMP masses > 8 GeV/c^2. Also shown are experimental results from [33] [34] [36] [38] [45] [55] [56] [57] [58] [59] [60] . The grey region is the region preferred by supersymmetric models [61] [62] [63]. Figure taken from [43].

.

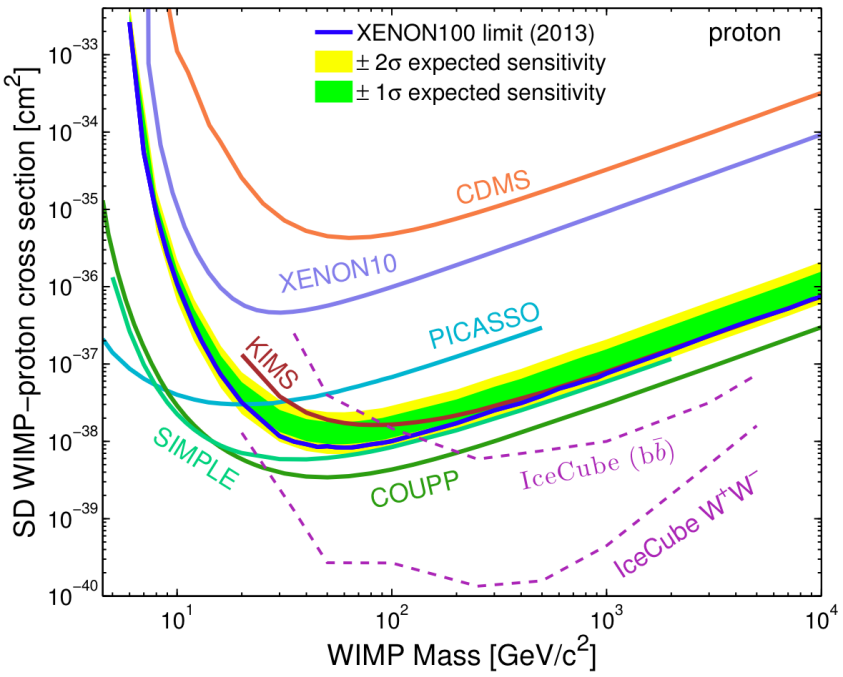

Figure 2.12: WIMP exclusion limit from 225 live days for spin dependent coupling to protons. Figure taken from [44].

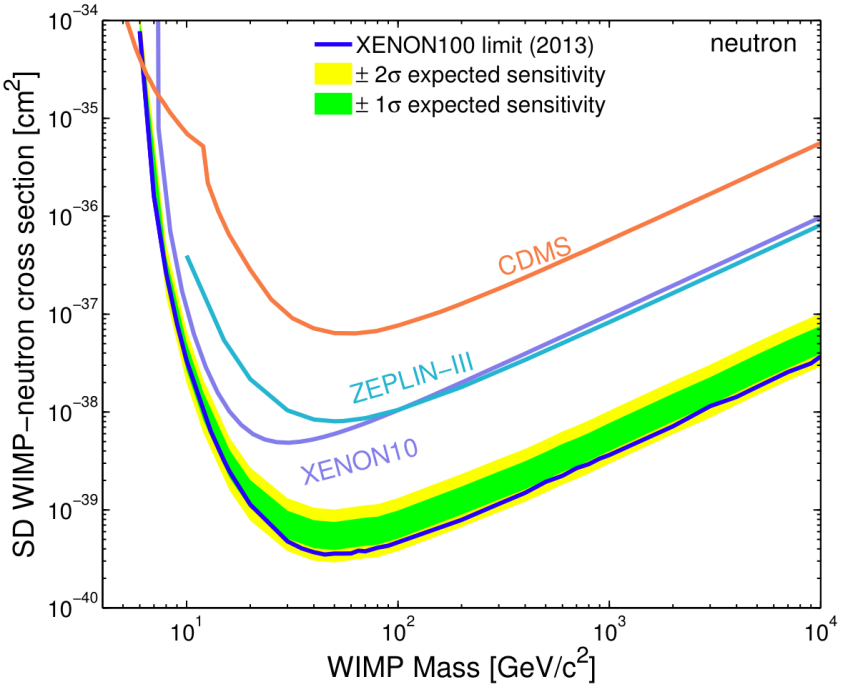

Figure 2.13: WIMP exclusion limit from 225 live days for spin dependent coupling to neutrons. Figure taken from [44].

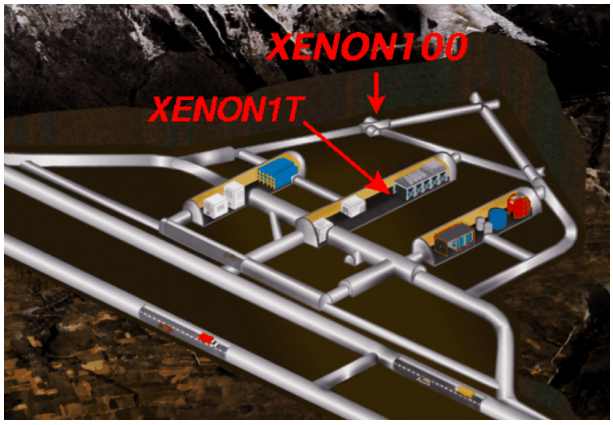

Figure 2.14: Position of the XENON100 and the XENON1T detector in the LNGS underground laboratory. Figure taken from [65].

pling (Fig. 2.12) and WIMP-neutron coupling (Fig. 2.13). For WIMP-neutron coupling the most stringent exclusion limit was set for WIMP masses above 6 GeV/c^2, down to a cross-section of $\sigma = 3.5 \cdot 10^{-40}$cm^2 at a WIMP mass of 45 GeV/c^2 at 90 % confidence level [44].

2.6 Future Detectors

2.6.1 XENON1T

The XENON1T experiment is the successor of the XENON100 experiment. Using 3.5 t of liquid xenon it aims at improving the sensitivity for detecting dark matter by two orders of magnitude. Like XENON100 it will be situated at the LNGS underground laboratory (Fig. 2.14). Construction has started in summer 2013, and commissioning is expected for the end of 2014.
Naturally, increasing the target mass leads to a bigger overall detector. The TPC will have a height of 1 m and 1 m diameter. Additionally, the detector will be immersed in a water tank with a diameter of 9.6 m and a height of 10 m. This water shield will be instrumented with 84 high QE PMTs in order to act also as an active muon veto.
The number of PMTs inside the TPC will not change substantially. Instead the sensitive area of each individual PMT will be increased by replacing the 1 ” square R8520 PMTs,

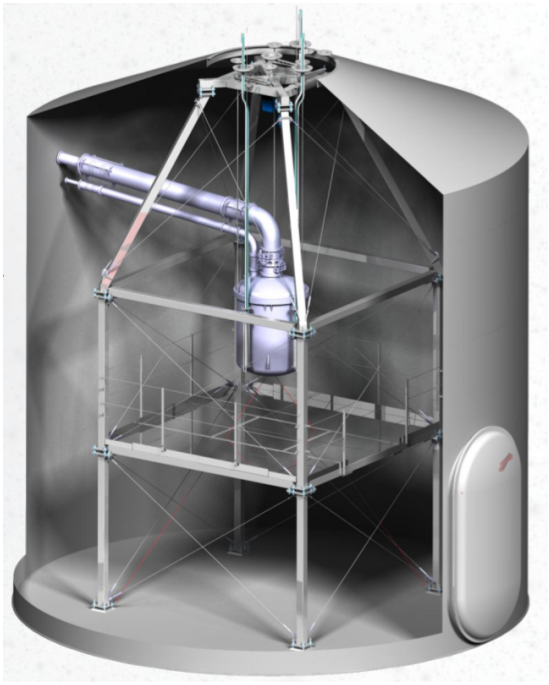

Figure 2.15: CAD drawing of the XENON1T detector within its water shield. Drawing taken from [65].

Figure 2.16: Construction of the water shield for XENON1T in hall B of the LNGS underground laboratory. Photograph from [65].

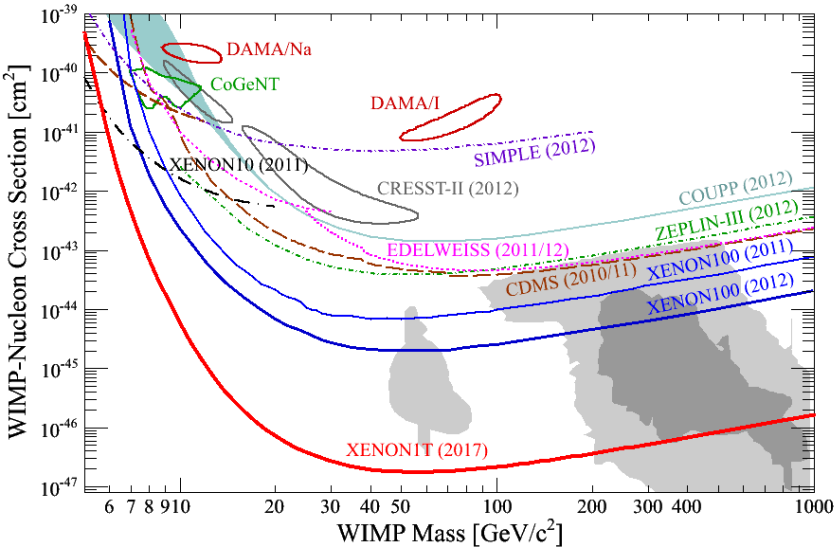

Figure 2.17: Projected sensitivity for XENON 1T. Figure taken from [66].

that have been used in XENON100, with the round R11410 PMTs with 3 ” diameter which have been developed specifically for the use in liquid xenon. These PMTs, which will be discussed in detail in Chapter 6, also show improved quantum efficiency and reduced radioactivity.

The total background in XENON1T is expected to be less than one event in 2 ton year exposure, 100 times lower than that observed in XENON1T. In order to reach this goal all materials will be selected for low radioactivity, and intrinsic background from the xenon will be reduced by removing krypton with the distillation column and radon with an adsorption tower.

XENON1T aims at improving the sensitivity of XENON100 by two orders of magnitude, down to a cross-section of $2 \cdot 10^{-47}$cm^2 at a WIMP mass of 50 GeV/c^2 (see Fig. 2.17).

2.6.2 DARWIN

The DARWIN (DArk matter WImp search with Noble liquids) project is currently a design study for a multi-ton dark matter experiment using of liquid xenon and/or liquid argon. It aims at probing the parameter space down to a WIMP-nucleon cross section of 10^{-48} cm^2 [67] (Fig. 2.18). DARWIN combines the expertise of several collaborations such as XENON, DarkSide [47] or ArDM [68], that have experience working with liquid xenon

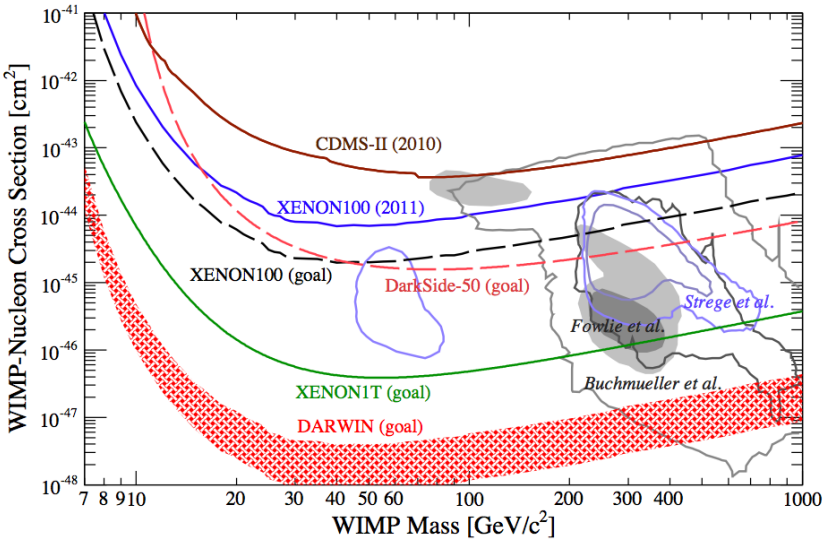

Figure 2.18: Projected sensitivity for DARWIN. Figure taken from [67].

or liquid argon in dark matter experiments. It envisages one or two TPCs similar to what is used in the XENON detectors. For the light and charge readout several possibilities are currently under investigation, including the Hamamatsu R11410 PMT that will also be used in XENON1T, and the Hamamatsu R11065 PMT that was designed for the use in liquid argon and is different from the R11410 only in its photocathode.

Chapter 3

The Electromagnetic Background in XENON100

In order to perform a reliable dark matter analysis it is important that the detector itself is well understood. This includes the electromagnetic background spectrum. Comparing the observed background spectrum to the expectations from Monte Carlo studies using the screening values of the detector material allows to cross-check the assumptions that are used in the dark matter analysis. In this chapter the electromagnetic background spectrum of run10, which lasted from September 2010 to May 2012, is presented. In the course of these studies it was discovered that the position dependent correction of the S2 signals was not correct, and a new correction map has been developed which improves the resolution in the high-energy range of the background spectrum.
Additionally, the discrimination between electronic and nuclear recoils at the beginning of run10 is presented. This discrimination plays an important role in the dark matter analysis (see Section 2.4.3). However, the study presented here is using only the data at the very beginning of run10. Final studies of the whole run have been performed within the collaboration.
While the work presented in this chapter is part of this thesis project, it is only part of the work of the whole XENON100 collaboration, which has been building and operating the detector, performed basic data processing as described in Section 2.3 and developed all of the data selection cuts (Section 2.4.2) that have been used.

3.1 Discrimination

One important part in background rejection in the XENON experiment is the ability to discriminate between electronic and nuclear recoils based on the ratio between S1 and S2 light. In order to quantify the discrimination power the electronic recoil (ER) band is studied using weekly calibrations with ^{60}Co and ^{232}Th sources. The nuclear recoil (NR) band is defined using an AmBe source which is used for a calibration run of several days performed about once per year.
For both the nuclear and the electronic recoil band the data has then been plotted in $log_{10}(\frac{S2}{S1})$ in dependence of $S1$. For $S1$ the position corrected integral of the S1 signal over all PMTs, and for $S2$ the position and lifetime corrected integral of the S2 signal over all PMTs in the bottom array has been used. Both quantities are measured in photoelectrons (PE). For the S2 signal only the bottom PMTs are used in order to avoid saturation effects, which are more likely to be observed in the top PMTs, as those see more of the S2 light. The resulting electronic recoil band is shown in Fig. 3.1, and the nuclear recoil band is shown in Fig. 3.2.
For fitting the electronic recoil band, bins with a width of 2 PE have been selected in S1. The distribution of $log_{10}(\frac{S2}{S1})$ in each of these bins has then been fitted with a gaussian function. The band is defined by the μ and 2σ of these fits (marked in Fig. 3.1).

The same is done for the nuclear recoil band, but because the nuclear recoil band does not have a gaussian profile as the electronic recoil band does, instead of using a gaussian fit to the distribution of $log_{10}(\frac{S2}{S1})$, the median and the 5% and 95% quantiles have been used (marked in Fig. 3.2).

By subtracting the mean of the electronic recoil band from the discrimination parameter $log_{10}(\frac{S1}{S1})$ the bands are transferred into the flattened discrimination space, in which the profile of the electronic recoil band appears as a gaussian distribution with the mean $log_{10}(\frac{S1}{S1}) - ER = 0$ (Fig. 3.3).
In run10 the anode voltage had been reduced from 4.5 V in run8 to 4.4 V. To see whether the bands had changed, the same analysis has been done with data from run8. The bands where found to be generally in very good agreement, with the exception of a slight discrepancy in the electronic recoil band in the lowest energy region (Fig. 3.4).
The electronic recoil band has also been calculated separately for ^{60}Co and ^{232}Th data. The two have been found to be in very good agreement (Fig. 3.5).

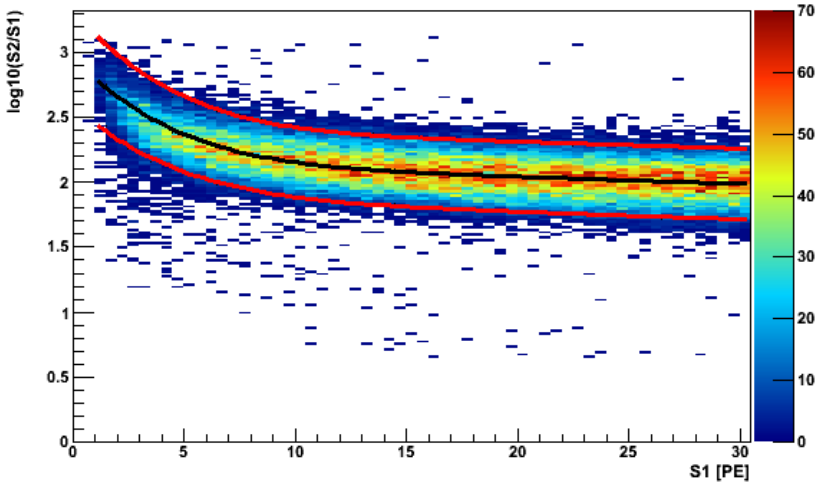

Figure 3.1: The low-energy part of the electronic recoil band derived from the combined ^{60}Co and ^{232}Th calibrations in the first three months of run10. Indicated are the mean (black) and the $\pm 2\sigma$ lines (red).

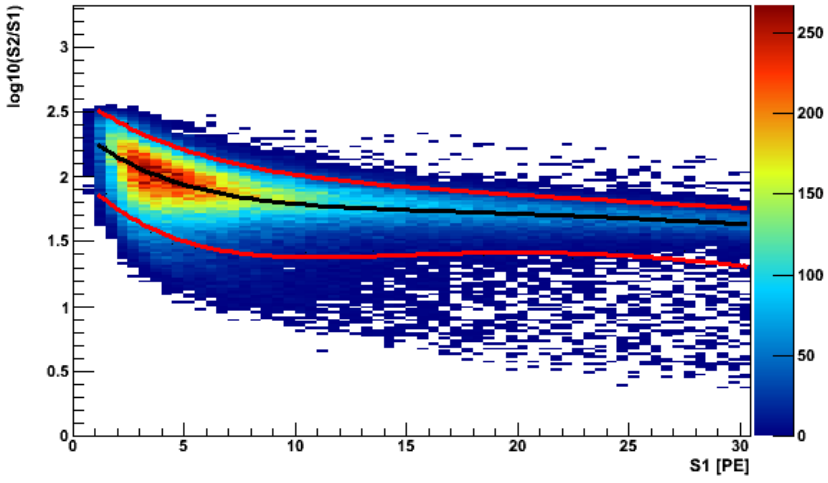

Figure 3.2: The low-energy part of the nuclear recoil band derived from the first AmBe calibration of run10. Indicated are the mean (black) and the 5% - and 95% lines (red).

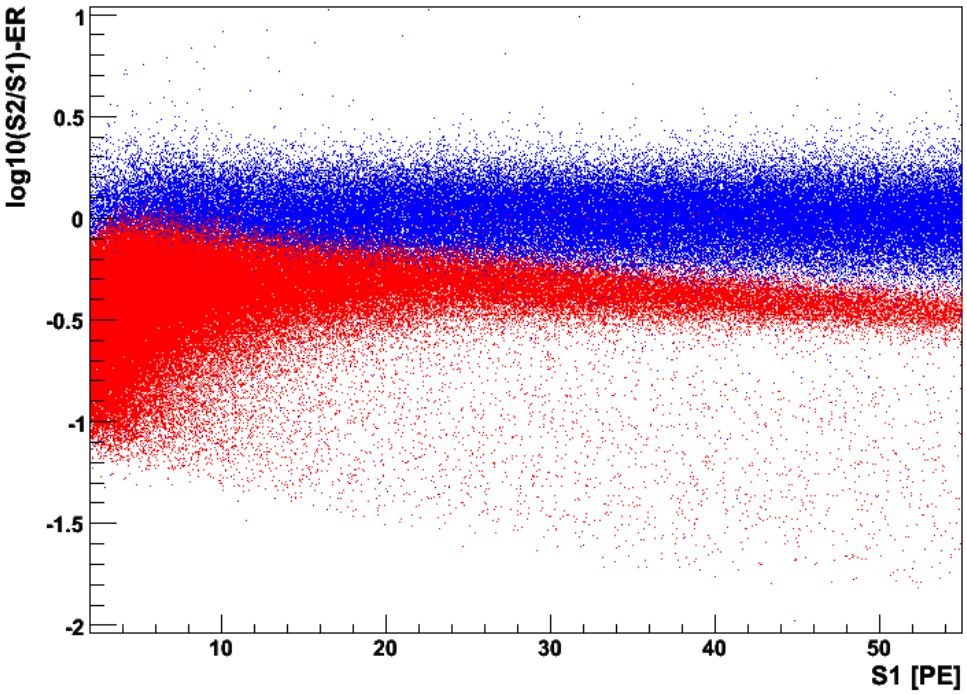

Figure 3.3: The electronic recoil (blue) and the nuclear recoil (red) bands from the beginning of run10 in the flattened discrimination space. Transformation into the flattened discrimination space is achieved by subtracting the mean of the electronic recoil band (ER), as determined in Fig. 3.1, from the discrimination parameter log10(S2/S1).

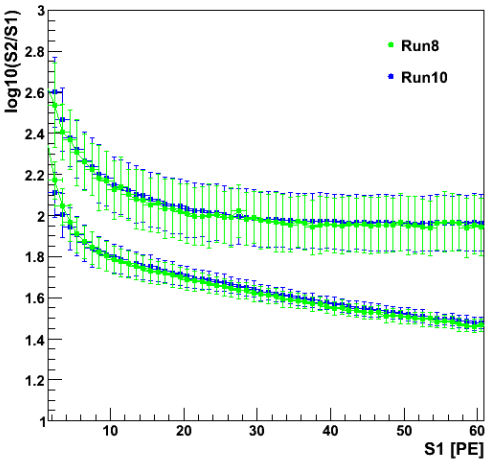

Figure 3.4: Nuclear recoil and electronic recoil band for run8 (green) and the beginning of run10 (blue). They are in good agreement except for a slight difference in the electronic recoil band in the lowest bins.

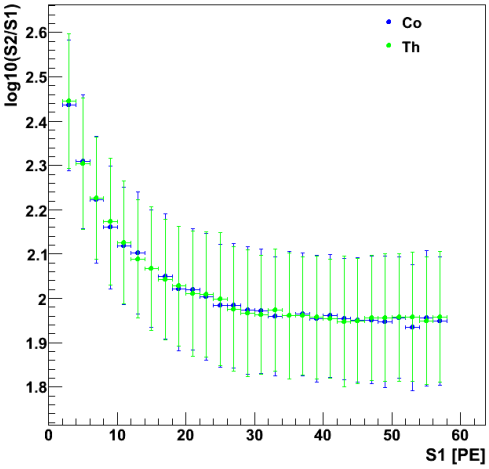

Figure 3.5: Comparison of the electronic recoil band in run10 derived from ^{60}Co (blue) and ^{232}Th (green). They are in good agreement.

Finally the rejection power for electronic recoils at 50 % nuclear recoil acceptance has been calculated for each bin (Fig. 3.6). It has been found to be $> 98.1\%$ for all energies.

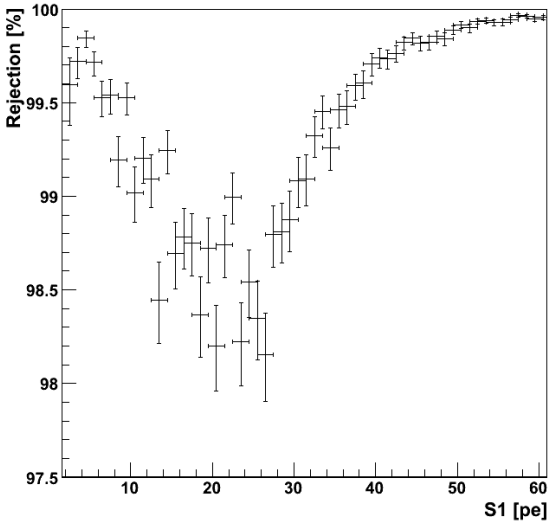

Figure 3.6: Rejection power for electronic recoil events at 50 % nuclear recoil acceptance.

3.2 X-Y Position Dependent S2 Correction

The light signals in XENON100 are measured with the two inner PMT arrays. The output of each PMT is converted to photoelectrons using the gains established from the weekly LED calibrations (see Chapter 5). For the secondary scintillation light signal (S2), two correction factors are used on the raw data: an electron lifetime correction and an x-y position correction. The electron lifetime correction accounts for the charge loss over long drift times, causing reduced S2 signals for events closer to the bottom of the TPC. The x-y position correction accounts for the observed position-dependent differences in amplification in the gas phase. These differences are thought to be due to slight warping in the electrode meshes, leading to different local fields.

A correction map for this effect has been applied already in previous runs, but in run10 it was found that it was not accurate anymore. A new map had therefore to be designed for the correction of run10 data. Different from the previous map which was derived from Cs calibration data, this correction map is obtained from the 40 keV line measured during the two calibrations with an AmBe source conducted in 2011 and 2012. 40 keV events are selected by cutting on the total S1 from all inner PMTs (cS1sTot) and the total S2 signals as seen by the bottom PMTs (cS2sTotBottom). The signals have already been

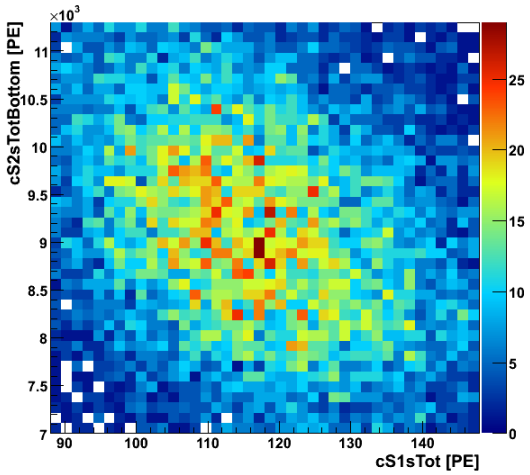

Figure 3.7: Selected 40 keV data from the 2011 AmBe calibration.

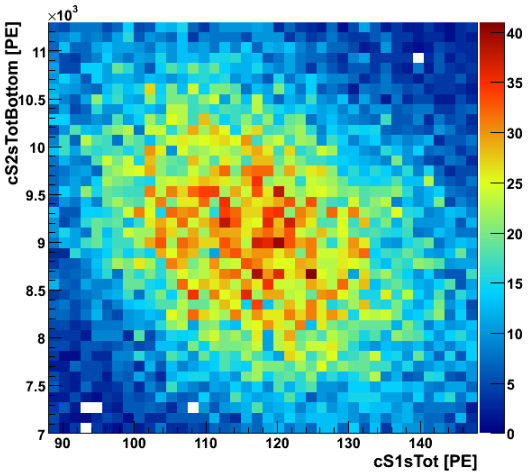

Figure 3.8: Selected 40 keV data from the 2012 AmBe calibration.

corrected using the old run8 correction map as well as electron lifetime correction. The selected events can be seen in Figs. 3.7 and 3.8 for both the 2011 and the 2012 AmBe calibration data. From this selected events the cS2sTotBottom signals are filled into a histogram and a gaussian fit is used to determine the mean value (Figs. 3.9 and 3.10).

The x-y plane of the detector volume is now divided into $16 \cdot 16$ pixels. For each of those pixels the mean of the cS2sTotBottom signals from events within this pixel is determined and then compared to the mean in the whole TPC volume, resulting in the correction maps shown in Figs. 3.11 and 3.12. Established from data already corrected with the S2 correction maps used in run8, these maps picture the difference in S2 size from run8 to run10 depending on the position of the event within the detector. While there is a clear change between these runs there seems to be not much difference between the 2011 and 2012 data. The two have therefore been combined in order to achieve a single S2 correction map that can be used for the entire run10 (Fig. 3.13). The effect of employing this updated position dependent S2 correction becomes obvious in the electromagnetic spectrum: although the map was determined on 40 keV data the resolution greatly improves especially for the Co and K peaks at more than 1 MeV (Fig. 3.14).

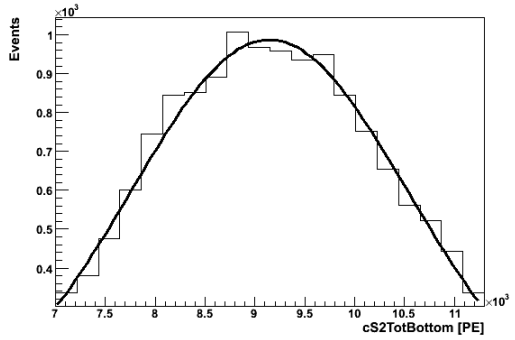

Figure 3.9: Total cS2TotBottom distribution in the 40 keV line from the 2011 AmBe calibration.

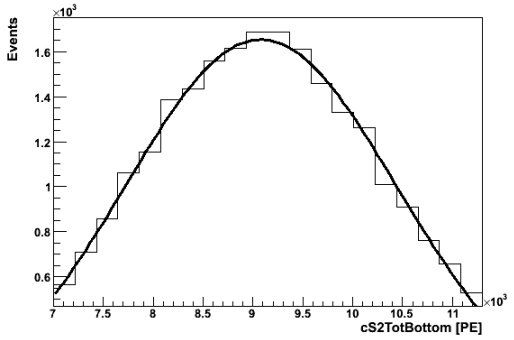

Figure 3.10: Total cS2TotBottom distribution in the 40 keV line from the 2012 AmBe calibration.

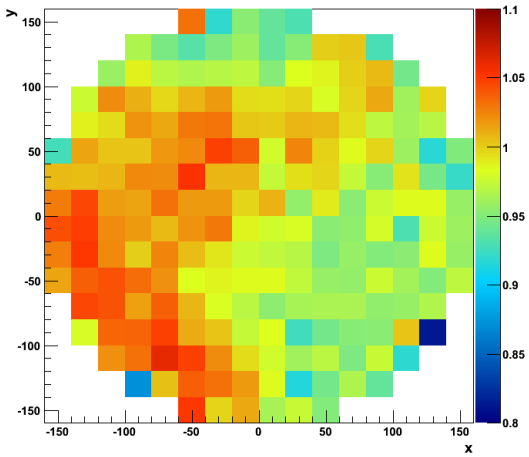

Figure 3.11: S2 correction map derived from the 40 keV line in the 2011 AmBe calibration.

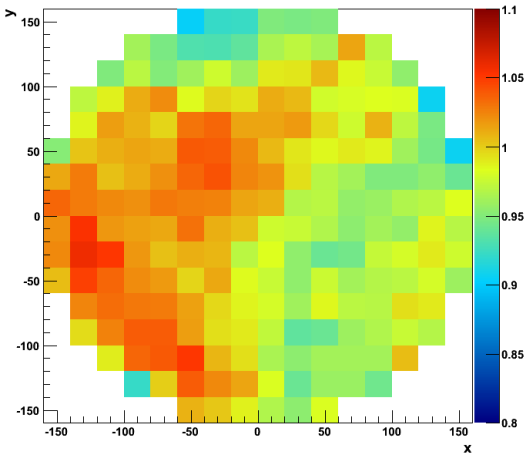

Figure 3.12: S2 correction map derived from the 40 keV line in the 2012 AmBe calibration.

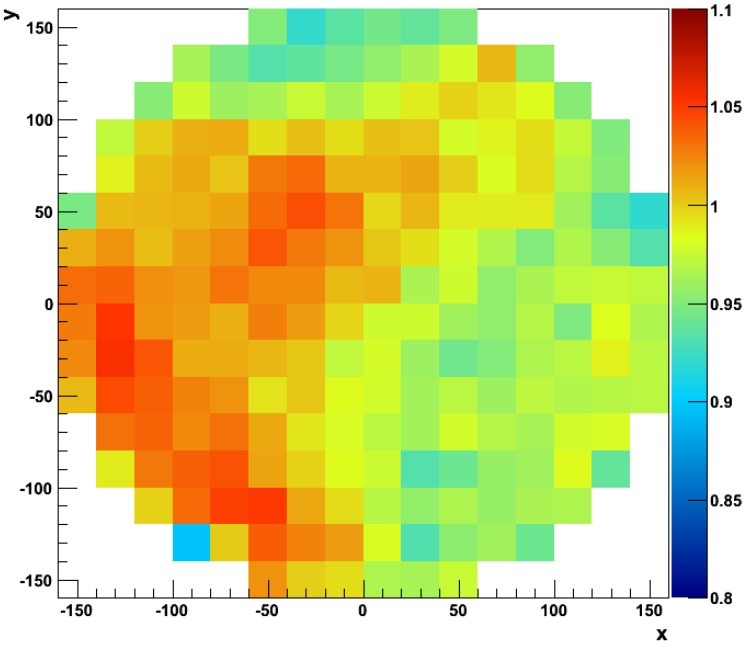

Figure 3.13: S2 correction map derived from the 40 keV line in the combined 2011 and 2012 AmBe calibration data.

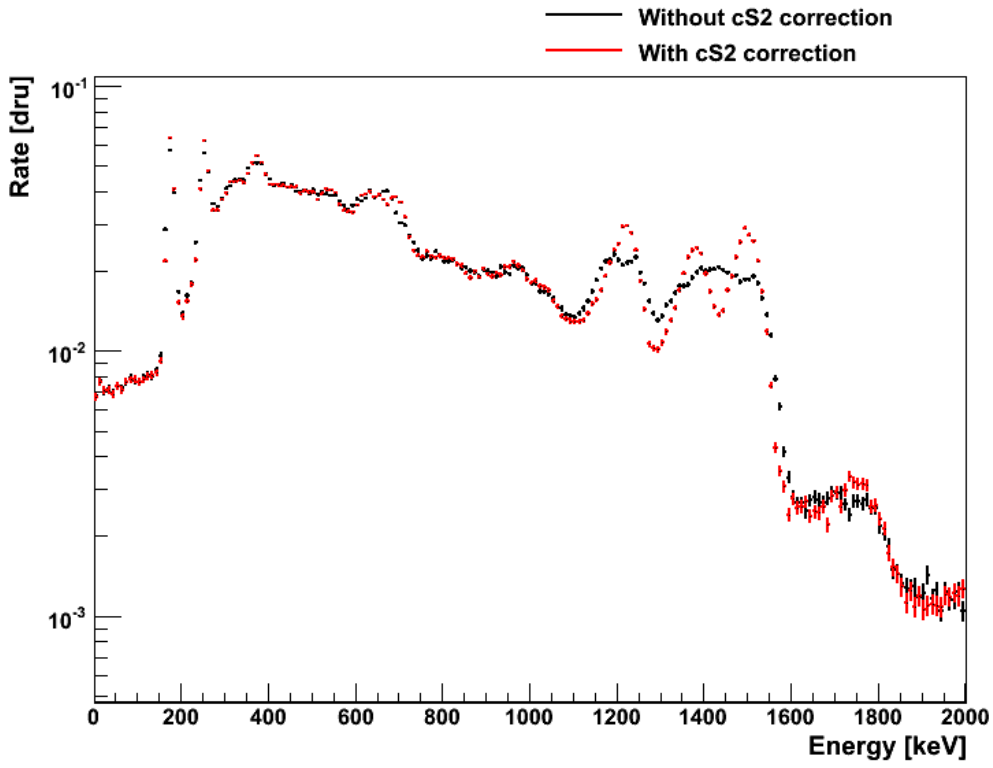

Figure 3.14: Effect of the new S2 correction on the electromagnetic background spectrum in run10 in a fiducial volume of 30 kg.

3.3 Electromagnetic Background Spectrum

3.3.1 Combined Energy Scale

For any event in the XENON100 detector two light signals are observed: S1 from direct scintillation light and S2 which is proportional to the ionisation charge. Due to recombination fluctuations the contributions of the two signals can vary for an event of a given energy, but as the total amount of quanta stays the same, S1 and S2 show a strong anti-correlation [69]. The energy resolution can therefore be improved by combining the two signals in the so called combined energy scale (CES) of the form

$$E = a \cdot S1 + b \cdot S2. \tag{3.1}$$

In order to determine the values for a and b, events with known energy are used, either from calibration sources or from distinguished lines in the detector background. Here the following lines from the background spectrum have been used: 295 keV and 351 keV from ^{214}Pb, 583 keV from ^{208}Tl, 662 keV from ^{137}Cs, 835 keV from ^{54}Mn, 911 keV from ^{228}Ac, 1173 keVand 1333 keV from ^{60}Co and 1461 keV from ^{40}K. The data is comprised of the entire standard dark matter search data of run10 in a 30 kg fiducial volume, using only the most basic cuts to ensure that each signal contains a valid S1 and S2 signal. The events for each energy have been selected by roughly cutting on the cS1sTot and the cS2sTotBottom signals, the latter having been position-corrected by using the correction map described in Section 3.2, and then plotted in a cS2sTotBottom vs. cS1sTot 2D histogram. By fitting a two dimensional gaussian function the mean cS1sTot and cS2sTotBottom have been found. A preliminary combined energy scale has then been created by fitting Equation 3.1 to the results of these gaussian fits. This preliminary CES has then been used in a second iteration in order to better select the events at each energy. The results of this second selection process together with the gaussian fits are shown in Figs. 3.15 - 3.23. The results of the gaussian fits are compiled in Table 3.1.

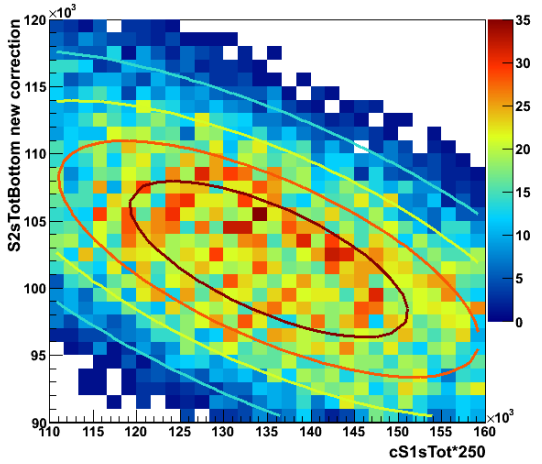

Figure 3.15: 295 keV line from ^{214}Pb.

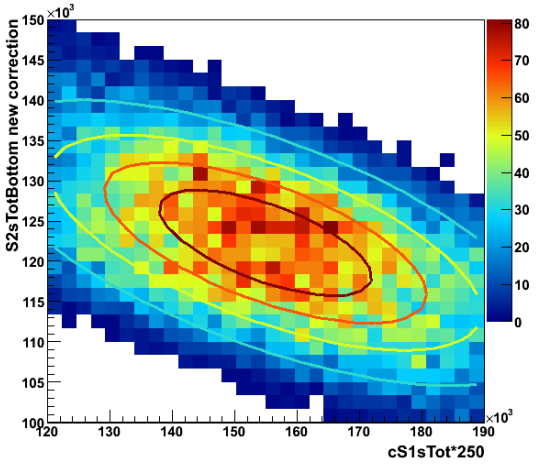

Figure 3.16: 352 keV line from ^{214}Pb.

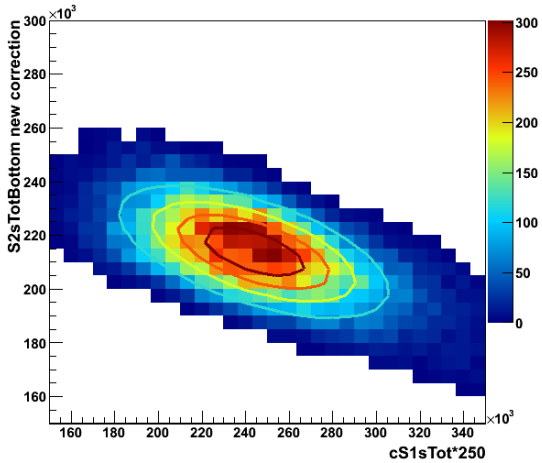

Figure 3.17: 583 keV line from ^{208}Tl.

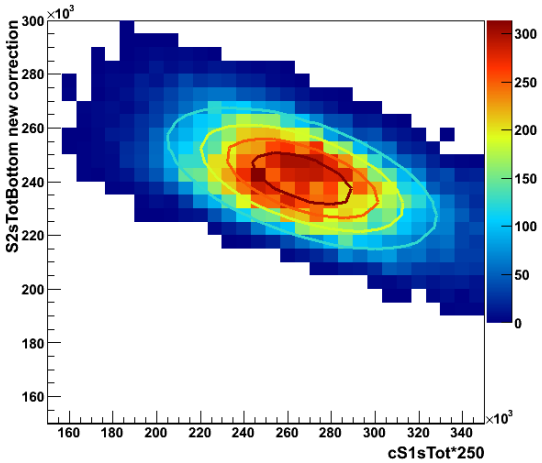

Figure 3.18: 662 keV line from ^{137}Cs.

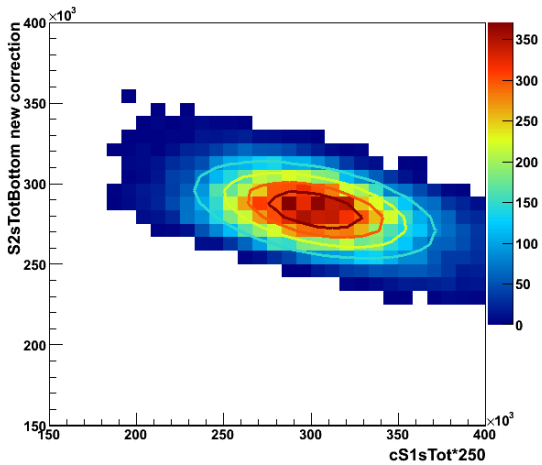

Figure 3.19: 835 keV line from ^{54}Mn.

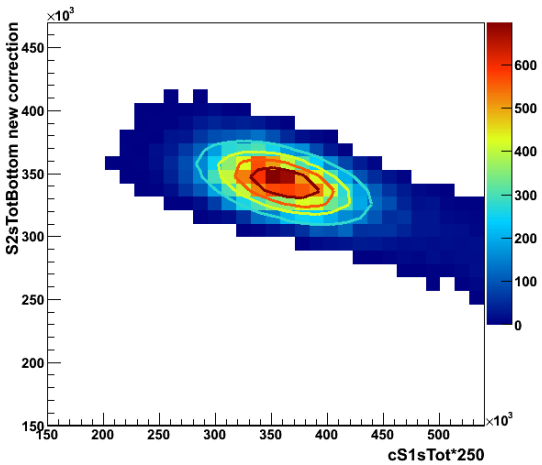

Figure 3.20: 911 keV line from ^{228}Ac.

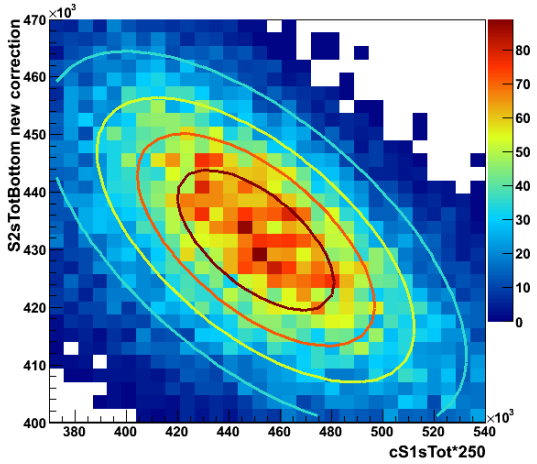

Figure 3.21: 1173 keV line from ^{60}Co.

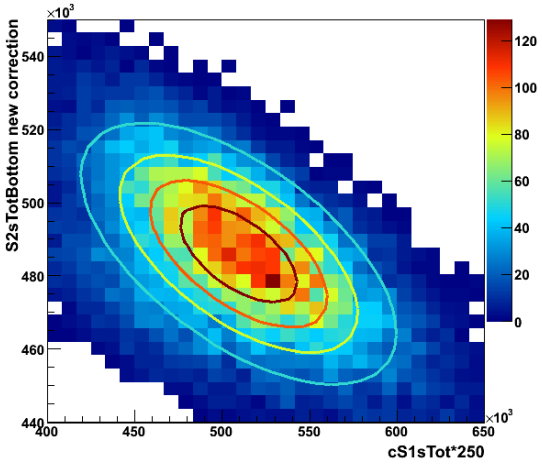

Figure 3.22: 1333 keV line from ^{60}Co.

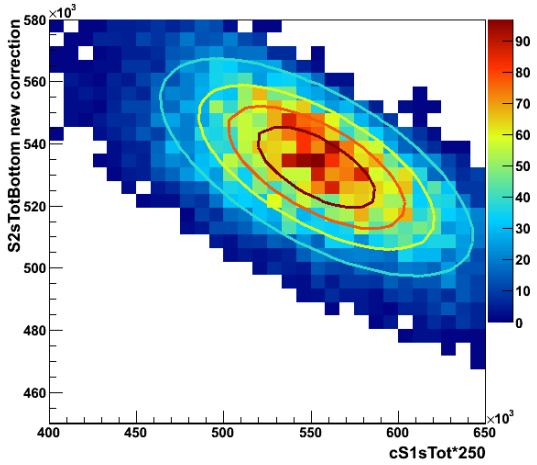

Figure 3.23: 1461 keV line from ^{40}K.

Element	Energy [keV]	Mean cS1sTot	Mean cS2sTotBottom
^{214}Pb	295.223 [70]	$5.606 \cdot 10^2$ ± 1.9	$1.0688 \cdot 10^5 \pm 1.68 \cdot 10^2$
^{214}Pb	351.932 [70]	$6.315 \cdot 10^2$ ± 1.3	$1.2620 \cdot 10^5 \pm 1.21 \cdot 10^2$
^{208}Tl	583.187 [71]	$1.0268 \cdot 10^3$ ± 1.6	$2.3234 \cdot 10^5 \pm 1.50 \cdot 10^2$
^{137}Cs	661.659 [72]	$1.0760 \cdot 10^3$ ± 1.5	$2.4866 \cdot 10^5 \pm 1.55 \cdot 10^2$
^{54}Mn	834.845 [73]	$1.2394 \cdot 10^3$ ± 1.4	$2.9344 \cdot 10^5 \pm 1.69 \cdot 10^2$
^{228}Ac	911.209 [74]	$1.4684 \cdot 10^3$ ± 1.6	$3.5437 \cdot 10^5 \pm 1.87 \cdot 10^2$
^{60}Co	1173.240 [75]	$1.8151 \cdot 10^3$ ± 2.0	$4.4087 \cdot 10^5 \pm 2.58 \cdot 10^2$
^{60}Co	1332.508 [75]	$2.0022 \cdot 10^3$ ± 1.0	$5.0056 \cdot 10^5 \pm 2.59 \cdot 10^2$
^{40}K	1460.822 [76]	$2.2404 \cdot 10^3$ ± 2.3	$5.5194 \cdot 10^5 \pm 2.39 \cdot 10^2$

Table 3.1: Results of gaussian fits to selected background lines.

Using these results to determine the parameters a and b in Equation 3.1, the following combined energy scale has been found:

$$\mathrm{E} = (1.62 \cdot 10^{-1} \cdot \mathrm{cS1sTot} + 2.02 \cdot 10^{-3} \cdot \mathrm{cS2sTotBottom})\ \mathrm{keV} \tag{3.2}$$

The full background spectrum for run10 using this scale is shown in Fig. 3.24.

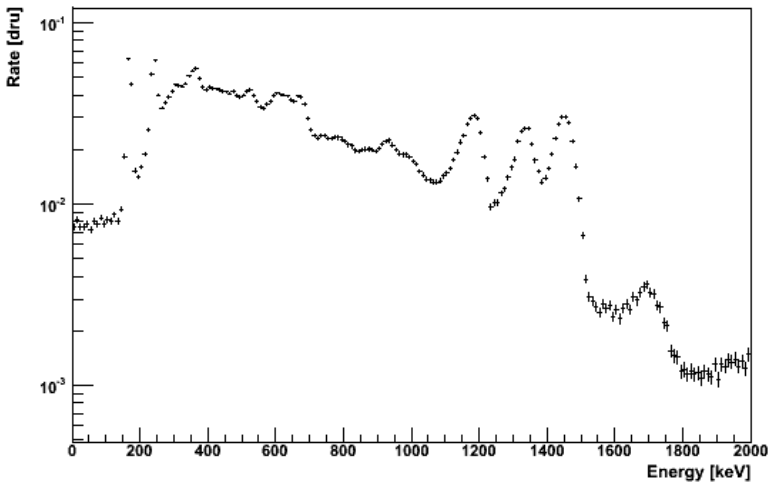

Figure 3.24: The electromagnetic background spectrum in run10 with a 30 kg fiducial volume cut on the combined energy scale Eq. 3.2.

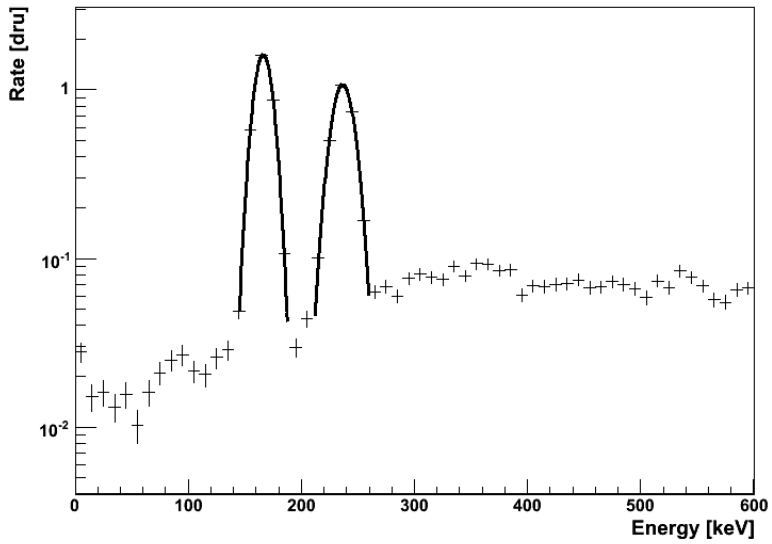

Figure 3.25: The low-energy background spectrum in run10 in the first 10 days after the AmBe calibration. The two peaks from ^{131m}Xe at 164 keV and ^{129m}Xe at 236 keV can be fitted with gaussian functions.

3.3.2 Measurement of the half-lives of ^{129m}Xe and ^{131m}Xe

The AmBe calibration leads to the activation of two xenon isotopes, which can be seen by the appearance of two additional peaks in the background spectrum in the following weeks. ^{131m}Xe decays with a half-life of 11.84 d, emitting gamma radiation with an energy of 163.93 keV [77] and ^{129m}Xe decays with a half-life of 8.88 d, emitting gamma radiation with an energy of 236.14 keV [78].
The decay of the activated xenon lines can be observed by dividing the background data taken after the AmBe calibration into intervals with a total measurement time of $\sim$ 5 days each and creating the background spectrum for each of these intervals. By fitting a gaussian function to each activated xenon line (Fig. 3.25) the height of the peaks can be determined.
Fig. 3.26 shows the evolution of the amplitude of this gaussian fit to the 164 keV line over time. By fitting with an exponential function

$$A(t) = C + A_0 \cdot e^{\frac{t}{\tau}}, \tag{3.3}$$

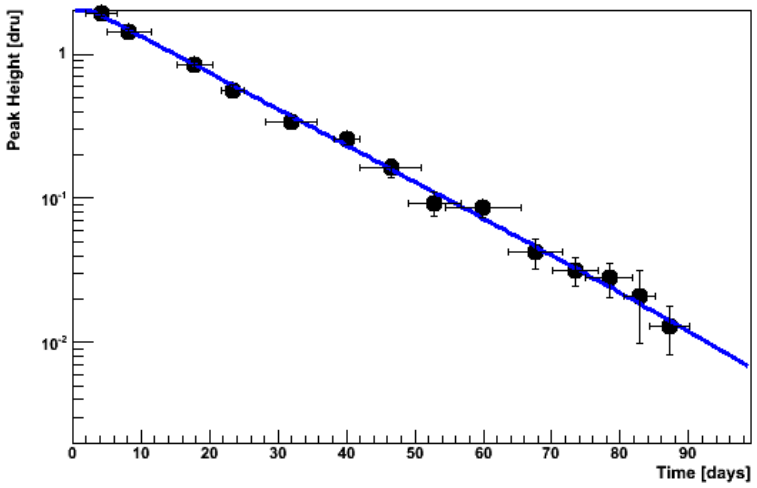

Figure 3.26: Decay of the 164 keV line from ^{131m}Xe. The half-life derived from the exponential fit (blue) is (11.98 ± 0.84) days.

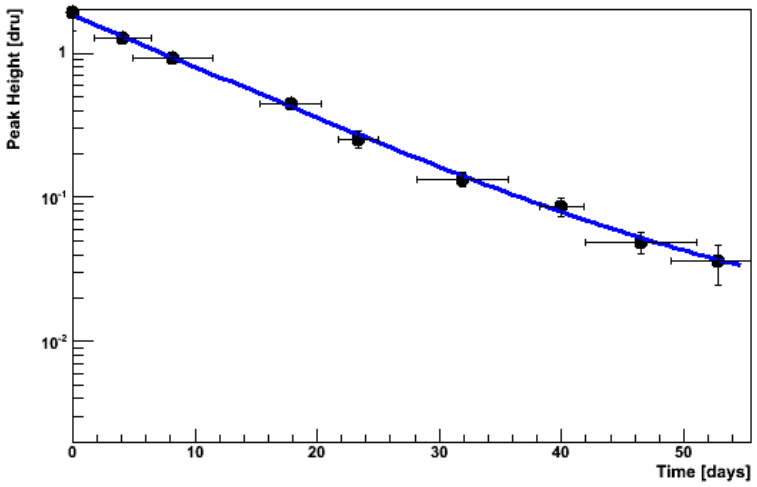

Figure 3.27: Decay of the 236 keV line from ^{129m}Xe. The half-life derived from the exponential fit (blue) is (8.27 ± 1.09) days.

where A_0 is the height of the peak at the beginning of the observed period and C is the constant level in the electromagnetic background spectrum that is independent of the activated xenon, the half-life $T_{1/2}$ of the decay can be estimated as

$$T_{1/2} = \tau ln(2). \tag{3.4}$$

Here $T_{1/2}$ has been found to be (11.98 ± 0.84) d.
The same has been done with the 236 keV line (Fig. 3.27), where the half-life has been found to be 8.27 ± 1.09d. Both half-lives agree with the literature values. After ~ 3 months both activated xenon isotopes have decayed such that the lines are not visible against the background any more. For the analysis in Section 3.3.3 the first three months after the AmBe calibration have therefore been excluded.

3.3.3 Fitting with Monte Carlo Data

As a cross-check the electromagnetic background spectrum of run10 has been compared to Monte Carlo simulations of the background. The same Monte Carlo spectra that had been already used in the analysis of the run7 background spectrum [79] [80] are employed here. They are based on the radioactivity of the detector material that has been screened with Gator before assembly [81] . It also includes spectra for the intrinsic contamination with radon and ^{85}Kr in the liquid xenon and from double beta decay of ^{136}Xe, based on a half-life of $T_{1/2} = 2.11 \cdot 10^{21} y$ [82].
The comparison has been done for a fiducial volume of 10 kg. The combined energy scale for this volume has been determined analogously to Section 3.3.1 to be

$$\mathrm{E} = (1.57 \cdot 10^{-1} \cdot \mathrm{cS1sTot} + 1.97 \cdot 10^{-3} \cdot \mathrm{cS2sTotBottom})\ \mathrm{keV}. \tag{3.5}$$

The data has been corrected with the new S2 correction map from Section 3.2.

Due to PMT saturation the high energy peaks in the background spectrum appear shifted towards lower energies. This saturation can be described by comparing the peak positions that are observed in the background spectrum (E_o) to the actual energies that correspond to these lines (E_a) (Fig. 3.28). The resulting saturation curve has been fitted with a third order polynomial and found to be

$$E_o = 6.47 \cdot 10^{-1} + (9.70 \cdot 10^{-1} \cdot E_a) + (9.67 \cdot 10^{-5} \cdot E_a^2) - (6.14 \cdot 10^{-8} \cdot E_a^3). \tag{3.6}$$

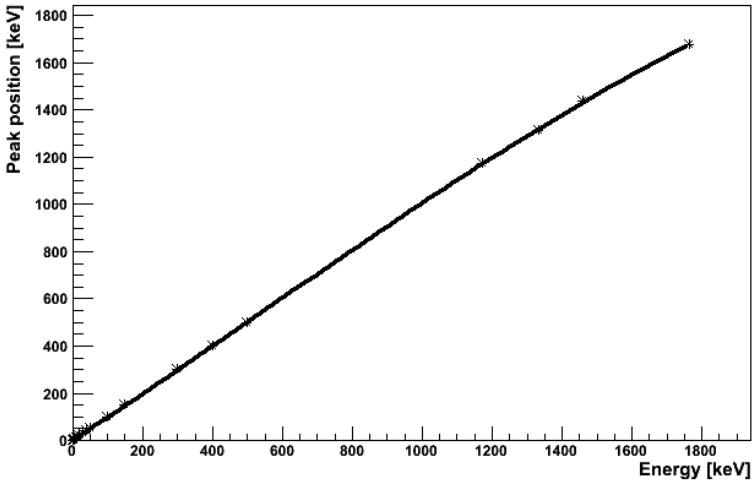

Figure 3.28: Comparison of the peak position for different lines in the run10 background spectrum to their expected positions, fitted with a third order polynomial function.

All Monte Carlo spectra have been modified to account for this saturation effect.
In fitting the Monte Carlo results to the background spectrum seven contributions have been free parameters: the radon contamination, the krypton contamination and the individual contaminations of the PMTs in uranium, cobalt, thorium, potassium and caesium. This is because not all individual PMTs have been screened prior to assembly and the measured value might therefore not be correct for the total contamination. All other values have been fixed to the expectations from screening [80].
The result can be seen in Figs. 3.29 and 3.30:

Source	Amount	Source	Scale factor	Source	Scale factor
Rn	85µBq/kg	PMTs U	2.85	PMTs K	1.56
Kr	0 ppt	PMTs Co	0.93	PMTs Cs	1.69
		PMTs Th	4.42	Detector material	1

The krypton contamination has been reduced so much with the help of the distillation column that it does not contribute significantly to the total background spectrum anymore. Mass spectroscopy measurements with a xenon sample from the detector gave indeed a krypton concentration of only 19 ppt, consistent with measurements from de-

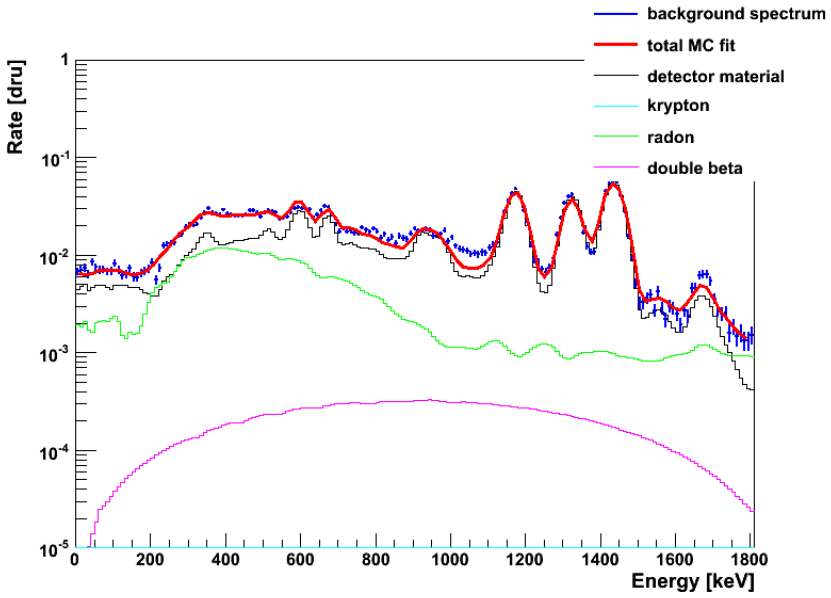

Figure 3.29: The background spectrum in run10 for a fiducial volume of 10 kg fitted with Monte Carlo data.

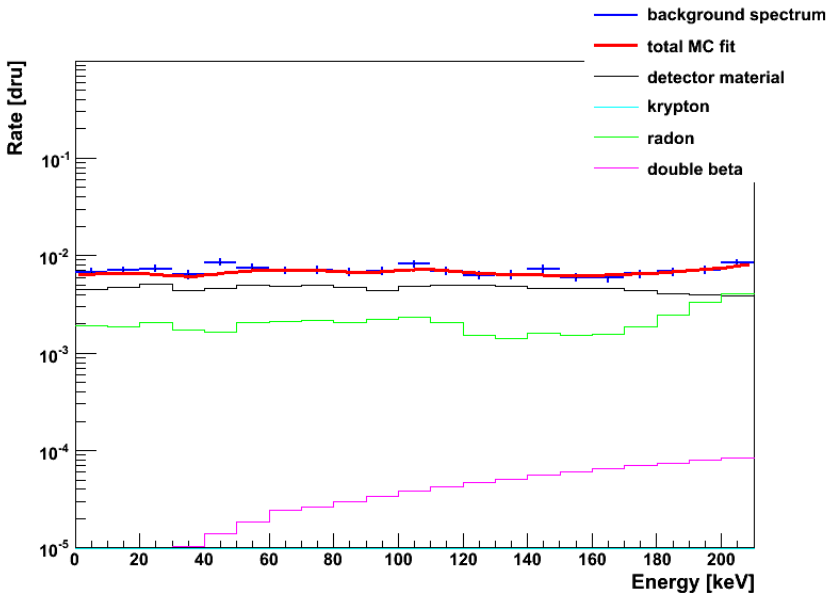

Figure 3.30: The low-energy region of the background spectrum in run10 for a fiducial volume of 10 kg fitted with Monte Carlo data.

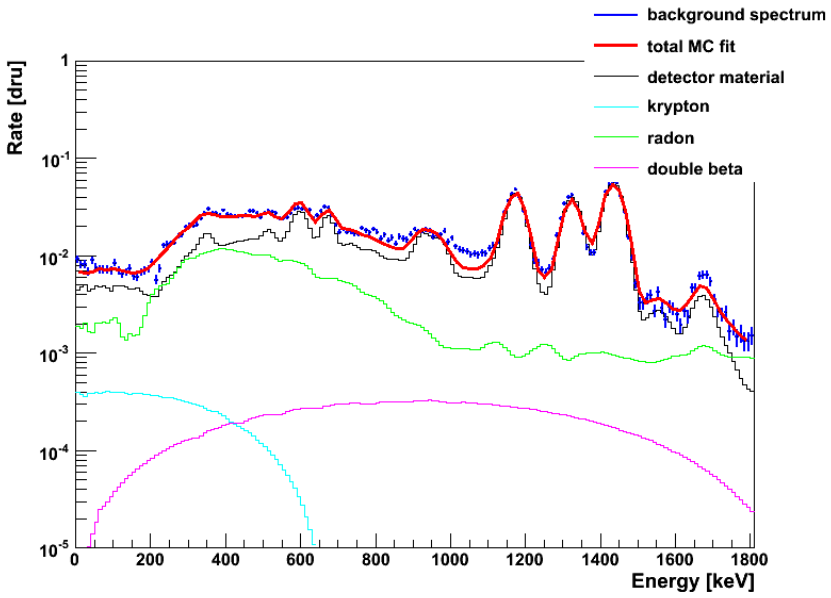

Figure 3.31: The background spectrum in run10 for a fiducial volume of 10 kg fitted with Monte Carlo data, with the Kr contamination fixed to 20 ppt.

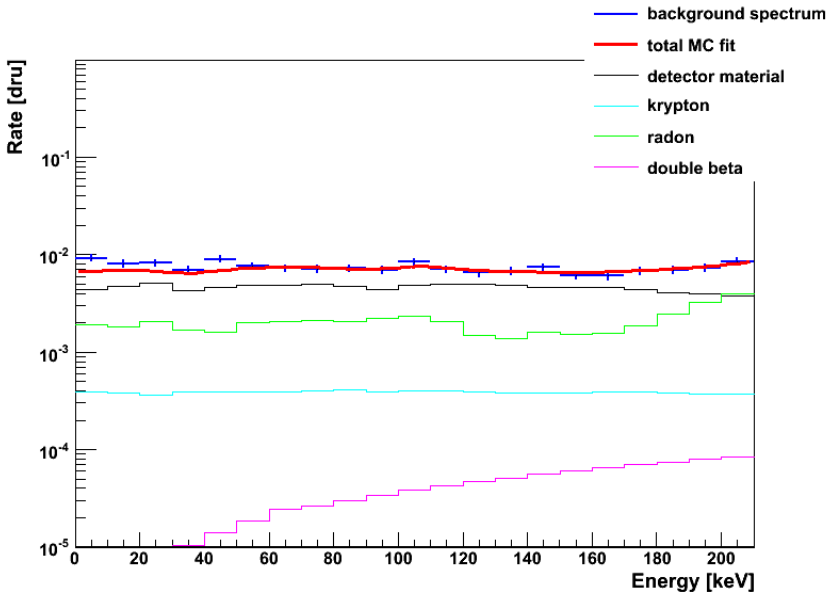

Figure 3.32: The low-energy region of the background spectrum in run10 for a fiducial volume of 10 kg fitted with Monte Carlo data, with the Kr contamination fixed to 20 ppt.

layed coincidence counting of the ^{85}Kr beta decay [43].
The Radon concentration in the xenon has been found to be 85 µBq/kg in this fit. Measurements of the ^{222}Rn emanation pointed to a concentration of 63 µBq/kg.
All in all the measured background corresponds quite well to the expectations from Monte Carlo. There is however a discrepancy in the region around 1 MeV which so far could not be explained. This discrepancy has also been observed in previous runs [79].
When the krypton contamination is fixed to 20 ppt (Figs. 3.31 and 3.32), the scale factor of the uranium contamination of the PMTs decreases accordingly:

Source	Amount	Source	Scale factor	Source	Scale factor
Rn	83µBq/kg	PMTs U	0.82	PMTs K	1.55
Kr	20 ppt	PMTs Co	0.91	PMTs Cs	1.72
		PMTs Th	4.35	Detector material	1

While fitting Monte Carlo spectra to the background data can serve as a cross-check, it can not be used to precisely determine the contaminations of the liquid xenon with radon and krypton, especially if the contamination of the PMTs is not fully known. This will be improved in XENON1T where all PMTs will be screened. For XENON100, the contamination with krypton should be derived with different methods such as spectroscopy measurements or delayed coincidence counting.

Chapter 4

Photomultiplier Tubes

The XENON detection principle is based on the observation of the two light signals S1 and S2 for each event. For this purpose photomultiplier tubes (PMTs) are used. These devices have been developed for more than a century [83] and have since been used in countless experiments. During that time they have been constantly refined and adapted to the various experimental conditions. Still no two PMTs even of the same type are exactly identical due to tiny variations during production. Together with the environmental influences this leads to individual behaviour for each PMT. Apart from this there are wide general differences between different PMT types. As the thorough understanding of the light signals in the XENON detectors is crucial for the interpretation of the data, good knowledge about the PMTs involved is essential.
This chapter is based on the information given in [83], [84] and [85].

4.1 Working Principle of a PMT

The basic set-up of a PMT is shown in Figure 4.1. It consists of a photocathode, several dynodes and an anode enclosed in a sealed and evacuated phototube. The dynodes are usually connected to a voltage divider base which sits on the pins outside of the tube and is supplied with high voltage. Light enters the evacuated tube through a transparent window. When it hits the photocathode, electrons are emitted via the photoelectric effect [86]. These electrons follow then the electric field created by the dynodes and possibly a focusing electrode onto the first dynode and then consecutively onto the following dynodes.

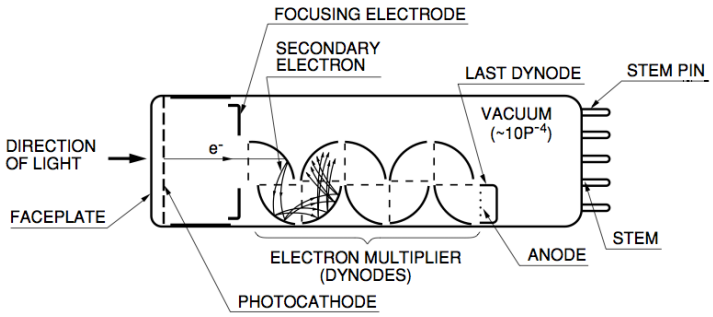

Figure 4.1: Schematic view of a PMT. Drawing from [84].

Each time, the total number of electrons is amplified by secondary emission [87]. After the last dynode the electrons are collected on the anode from where they are read out, resulting in an amplified signal that is proportional to the intensity of the initial light pulse.

4.2 Basic PMT Properties

4.2.1 Gain

The gain of a photomultiplier is the factor by which each initial photoelectron has been multiplied when the signal electrons are collected. It is the product of the secondary emission ratios of all dynodes:

$$G = \prod_{i=1}^{n} \delta_i, \tag{4.1}$$

where n is the number of dynodes and δ_i is the secondary emission ratio of dynode i, defined as the average number of secondary electrons per initial electron. This ratio depends of course also on the kinetic energy of the initial electrons and hence on the potential difference E_i between the dynodes i and $i-1$ or between the first dynode and the photocathode for $i = 1$:

$$\delta = a \cdot E_i^k, \tag{4.2}$$

where a and k are constants depending on the material of the dynode. The gain of the PMT increases with the number of dynodes and with the voltage. This allows to adjust PMTs to a specific gain by changing the supplied voltage.

4.2.2 Quantum Efficiency and Collection Efficiency

Not every photon that hits the window of the PMT leads to the emission of a photoelectron. The probability for an incident photon to eject a photoelectron is called quantum efficiency (QE) and depends on the wavelength of the photon. For modern PMTs the quantum efficiency is typically $\sim 30\%$. Several effects influence the total quantum efficiency of the PMT: First, the photon could be reflected or absorbed by the window before even reaching the photocathode. It is important to select the correct window material that is transparent to the wavelength of the light that one wants to detect. If this is not possible, an additional wavelength shifter can be used.
The photocathode can be either opaque or semitransparent, depending on whether the photoelectrons are emitted on the same or the opposite side of the light influx. Semitransparent photocathodes are deposited directly onto the inner surface of the PMT window. This type is used in the PMTs in both XENON100 and XENON1T.
Reflection of the photon can then also occur on the photocathode itself, especially for metallic photocathodes. This is one reason why today mostly semi-conducting photocathodes are used. In semi-conductors it is also less likely for an excited electron to lose energy in electron-electron scattering, and the work function which describes the energy necessary for an electron to leave the photocathode material can be much smaller than in metals.
The collection efficiency (CE) is the probability for a photoelectron that has been successfully ejected from the photocathode to reach the first dynode where the amplification process is started. It is often included in the quantum efficiency as the effects are difficult to separate in measurements.

4.2.3 Dark Counts

It is possible for the energy of an electron in the photocathode to exceed the work function even without the absorption of a photon. In this case the electron is accelerated onto the first dynode, creating a PMT signal called a dark count that is indistinguishable from a single photoelectron event. It is important to consider the dark count rate of a PMT that will be used for single photon counting. In general the dark count rate increases with temperature or for some time after the photocathode has been exposed to light. In some cases PMTs can be damaged leading to a permanently high dark count rate.

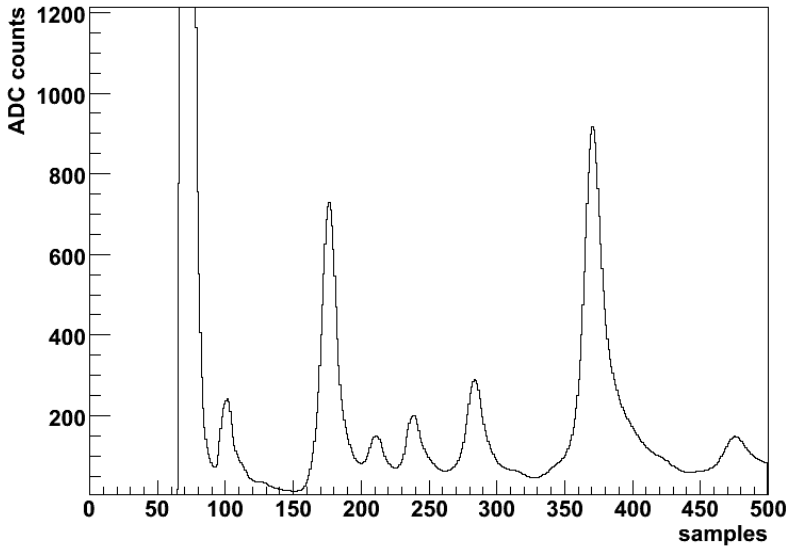

Figure 4.2: Afterpulses after a 10 ns long laser pulse with $\sim$ 50 000 photoelectrons in the R11410 PMT KB0056, a PMT that has been found to have a very high afterpulse rate. One sample is 10 ns long.

4.2.4 Late Pulses and Afterpulses

While the PMT is evacuated, the vacuum is never perfect so that it is still possible that a photoelectron or one of the secondary electrons hits a single gas atom in the phototube thereby ionising it. The positive ion then drifts along the electric field in the opposite direction of the electrons. When it hits the photocathode, more electrons are released which again are amplified in the PMT leading to a second signal, the so called afterpulse. The time between the original signal and the afterpulse depends on the mass of the ion (Fig. 4.2). The probability for an afterpulse to occur depends on the quality of the vacuum. Afterpulse rates can be high for some PMTs from manufacturing, but also increase with time when the vacuum deteriorates. The PMTs that will be used in XENON1T have therefore been tested for their afterpulse rates as described in [88]. In order to sustain a low afterpulse rate it is especially important to avoid leak testing around PMTs as helium can enter the PMT which then can lead to afterpulsing. Late pulses occur when a secondary electron is scattered away from the dynode. It will again follow the electric field lines being amplified at each dynode, leading to a smaller signal

shortly after the main pulse. The actual signal in this case is the sum of the main and the late pulse.

4.2.5 Linearity

In an ideal PMT the signal output would be always directly proportional to the number of photons in the incident light signal. In practice however, PMTs deviate from this perfect linearity for a number of reasons.
The most obvious limitation comes from the photocathode, which can provide only a limited amount of photoelectrons at once, which can lead to saturation effects for large signals. The linearity of the photocathode depends on its material and also the temperature, as the resistivity increases with cold temperatures.
When the signals become very large the electrons start to repel each other at the last dynode stages, which can lead to some electrons not hitting the dynodes anymore, resulting in too small signals. This so-called space charge effect can be avoided by optimising the geometry of the dynodes and increasing the voltage that is applied to the last dynode stages.
For large signals it is also possible that the last dynodes can not provide enough charge for linear secondary emission, leading to saturation effects. One way to overcome this is to add capacitors to the last dynode stages. This is discussed in detail in Section 7.1. While all the effects mentioned so far result in too small signals, overlinearity is also possible if the base current is too small, especially at high signal rates. In this case the electrons travelling between the last dynode and the anode form a current opposite to the one applied on the base, thereby reducing the potential difference between the last dynode and the anode. As the total voltage from photocathode to anode is fixed, it gets redistributed to the previous dynode stages. Because no secondary emission occurs between the last dynode and the anode, the increased voltage in the previous dynode stages results in a higher total gain. This overlinearity increases with larger signals or higher signal rates up to the point at which the potential difference between the last dynode and the anode becomes too small for the charge to be collected on the anode. This problem is also discussed in detail in Section 7.1.

Chapter 5

Calibration of the Photomultiplier Tubes in XENON100

One of the main components of the XENON100 detector are the 242 PMTs that observe the S1 and S2 light signals that compose every event as well as any signals from the veto volume. For the precision of these measurements it is important that the properties of each PMT are well understood. While the PMTs have been tested before the assembly of the TPC, their behaviour can change during operation. For this reason all PMTs are recalibrated once per week with blue LED light.
The calibration set-up was installed before the start of this PhD thesis. The following description of the hardware is therefore based mainly on [80], [89] and [90]. My own contribution consists of performing the weekly LED calibrations from January 2010 to April 2013 while expanding the existing calibration software, and its analysis, which is presented here.

5.1 PMTs in the XENON100 Experiment

The XENON100 detector uses a total of 242 PMTs, grouped in two arrays, consisting of 98 PMTs at the top and 80 PMTs at the bottom of the TPC, with the other 64 PMTs observing the top and the bottom of the active xenon veto of the detector (Figs. 5.1, 5.2 and 5.3). The PMTs at the bottom are arranged in a way to minimise the gaps between the PMTs, to ensure maximum sensitivity to the S1 signals that can be as small as a

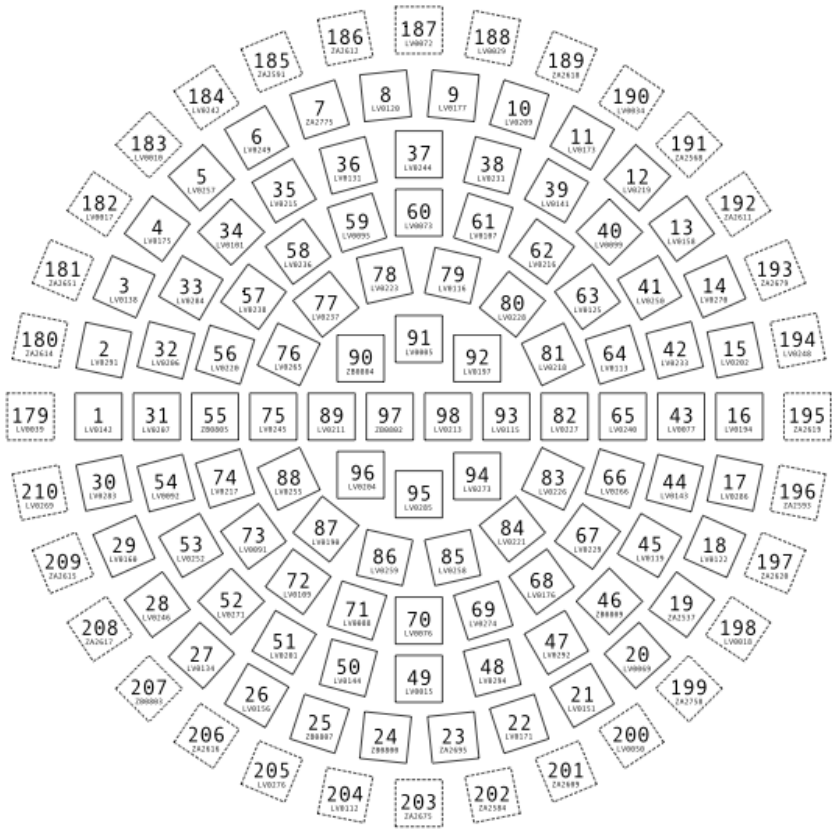

Figure 5.1: Arrangement of the PMTs in the top array of the XENON100 TPC. Drawing taken from [65].

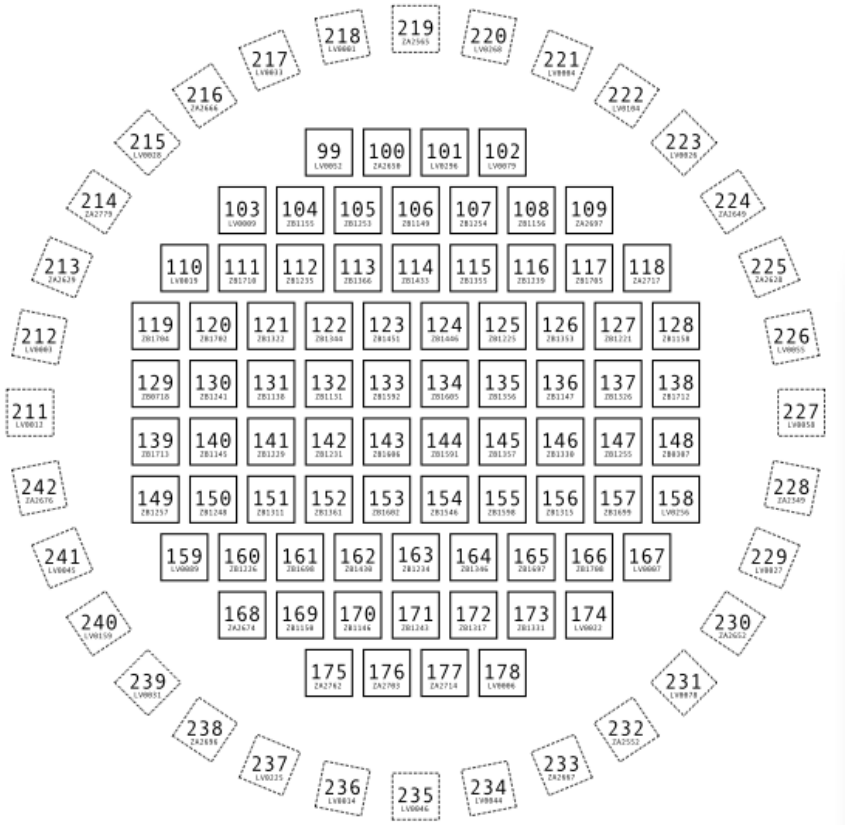

Figure 5.2: Arrangement of the PMTs in the bottom array of the XENON100 TPC. Drawing taken from [65].

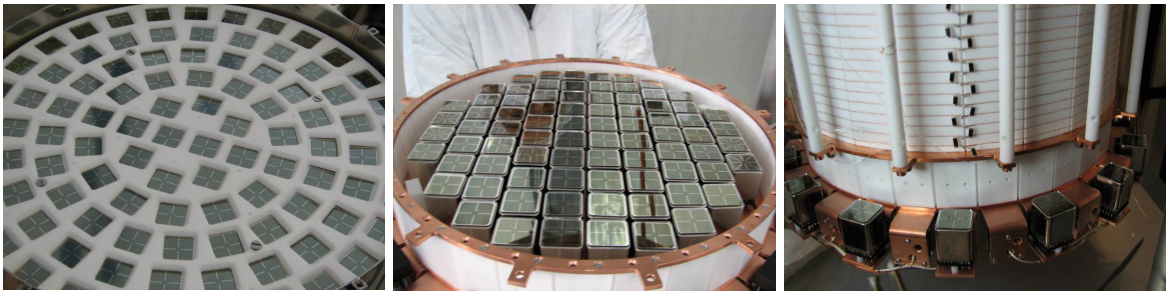

Figure 5.3: Top (left) and bottom (centre) PMT arrays without veto and veto PMTs at the bottom outside the TPC (right). Photographs taken from [65].

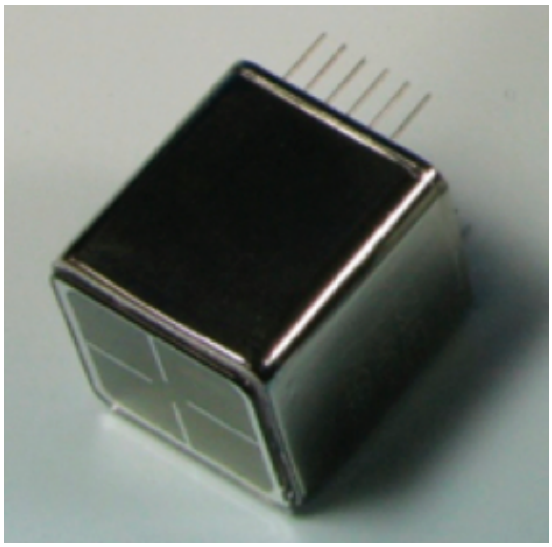

Figure 5.4: The Hamamatsu R8520 PMT. Photograph from [65].

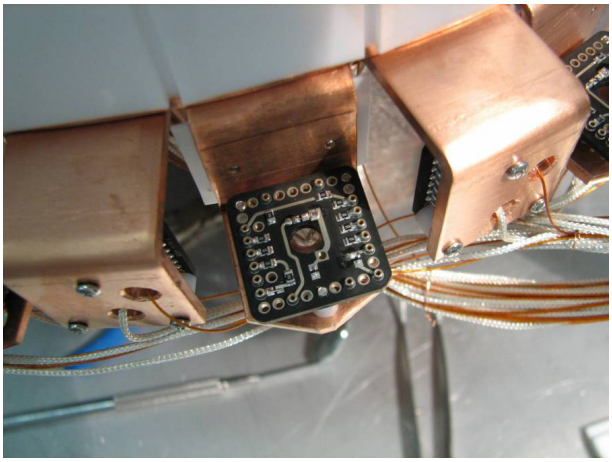

Figure 5.5: The voltage divider bases for the R8520 PMT installed in the veto array. Photograph from [65].

few photons (see Chapter 2). The PMTs with the highest quantum efficiencies have been placed here. The top array is optimised for position reconstruction using the much larger S2 signals.

The PMTs are the Hamamatsu R8520-06-AL model (Fig. 5.4), a 1" square PMT with 10 dynodes designed for the use in liquid xenon: It can sustain temperatures down to –110 °C and pressures up to 5 atm [91]. Its window, made from synthetic silica glass, is transparent for UV light and the bialkali photocathode is sensitive to the xenon scintillation light which has a mean wavelength of 178 nm. This allows for the operation in liquid xenon without the need of an additional wavelength shifter.

The PMTs placed in the top array and in the veto volume have a quantum efficiency of typically $\sim 23\%$, for the PMTs at the bottom array, which are a newer model with improved photocathode, it is $\sim 33\%$. The dynode collection efficiency is $\sim 70\%$ for all PMTs. The gain at a supply voltage of –800 V has been found to be $\sim 2{\cdot}10^6$ [80] [89] [90].

The negative high voltage is supplied to the PMT via a custom-made voltage divider base (Fig. 5.5). As with all materials in the detector, it has been optimised for durability and low radioactivity, using as few components as possible. For this base 13 resistors

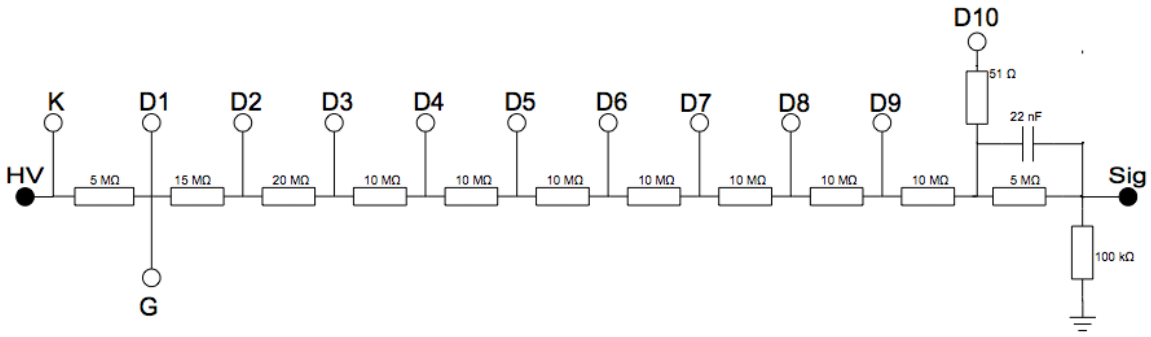

Figure 5.6: Circuit diagram of the R8520 base. High voltage is supplied to the photocathode K, the focusing electrode G and the dynodes D1 - D10.

and 1 capacitor are used. The resistances are chosen according to the ratio recommended by Hamamatsu, based on 1 R = 5 MΩ. The high resistance of 115.1 MΩ for the entire divider chain reduces the current flowing through the base and thus the power dissipation into the detector. Both the small current and the lack of additional capacitors come however with a trade-off of early saturation at high-energy or high-rate signals as they occur during calibration (see Section 7.1 for more information on this topic).
The circuit layout of the base can be found in Fig. 5.6. The electronic elements are soldered onto square printed circuit boards made from 1.55 mm thick copper-clad Cirlex. The base is connected to the PMT pins using spring-loaded brass sockets which allow for quick exchange of the PMTs if necessary.
After amplification by a factor of 10, using Phillips PS776 modules, the signals are recorded with CAEN V1724 flash ADC (FADC) modules, triggered by a clock generator that also triggers the LED signals. Different from the normal data taking (described in Section 2.3), during LED calibrations zero-length encoding is disabled and the complete waveforms (Fig. 5.8) are stored for all PMTs.

5.2 Gain Calibration

As the PMTs are a crucial part of the XENON100 detector, it is essential to monitor their behaviour throughout the data taking. For this reason a calibration system (Fig.

5.7) has been installed inside the detector that allows for regular monitoring of the PMT status without requiring additional hardware interventions [80] [89] [90].
Calibration is performed using LED light. Two blue InGaN LEDs emitting light with a wavelength of 470 nm are mounted in a light-tight box outside the detector. They are connected to standard coated quartz fibers with 1 mm cores leading to two Caburn FFT-UV600-c16 optical feedthroughs. Inside the detector, the feedthroughs are equipped with two quartz fibers with 800 µm cores that can withstand the temperatures required for baking the detector during the vacuum preparation before filling. The quartz fibers guide the LED light to the TPC volume where it is distributed by two bundles of polymethylmethacrylate (PMMA) fibers. A total of 10 fibers has been installed. One bundle of four fibers illuminates the TPC volume and the other bundle with six fibers is used for the calibration of the PMTs in the veto volume. They are placed in a way that a relatively uniform illumination of all PMTs is achieved. The light level can be adjusted separately for the two volumes since each is supplied from its own LED. The PMMA fibers have a core of 180 µm and have been successfully operated up to 90 °C [89], which is higher than the maximum allowed temperature for the PMTs, as well as in liquid xenon. To minimise the necessary material the fibers have been used without jackets. Despite being so close to the inner volume of the TPC, the naked fibers do to not introduce significant amounts of radiation thanks to their small total mass of ~ 1 g. During calibrations a LeCroy Mod. 222 clock generator module is used to trigger both a BNC Mod. 505 pulse generator and the DAQ at a rate of 100 Hz. The pulse generator supplies the LEDs with 4 µs long pulses. The amplitude is chosen for both LEDs individually aiming for a 2 - 3 % signal rate in the stored waveforms. In this way nearly all signals are from single photons allowing for a determination of the PMT's gain.
For every waveform 100 ADC samples (1 µs) before the trigger signal are digitised together with the complete period the LED is lit. This pre-trigger window is used to determine the baseline as well as the dark current and electronic noise rate of this PMT.
A sample waveform can be seen in Fig. 5.8. For each calibration 100 000 events are recorded. The whole data taking procedure takes less than 20 min and is repeated weekly. The raw data is then analysed using a software bundle consisting of several C++ and ROOT scripts. In order to achieve a more uniform signal-to-noise ratio across the PMTs, a software cut is used to shorten the calibration window in the waveforms of the more

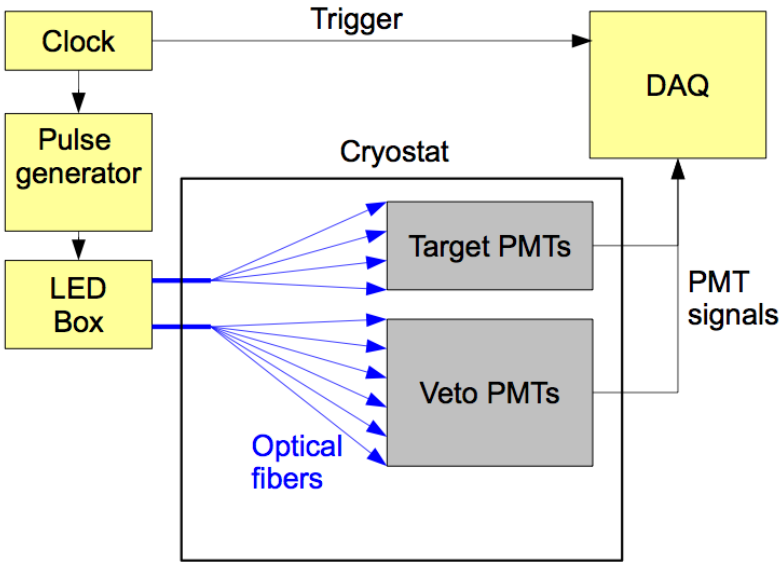

Figure 5.7: Schematic drawing of the XENON100 gain calibration set-up.

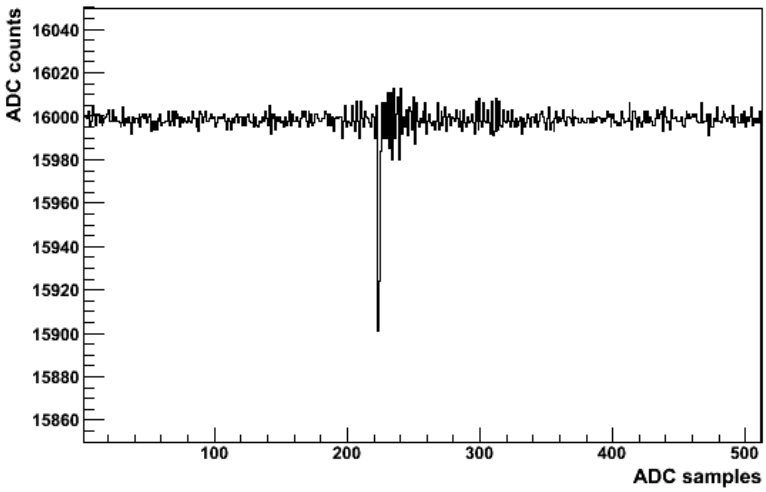

Figure 5.8: Waveform taken during gain calibration featuring an single photoelectron (SPE) signal.

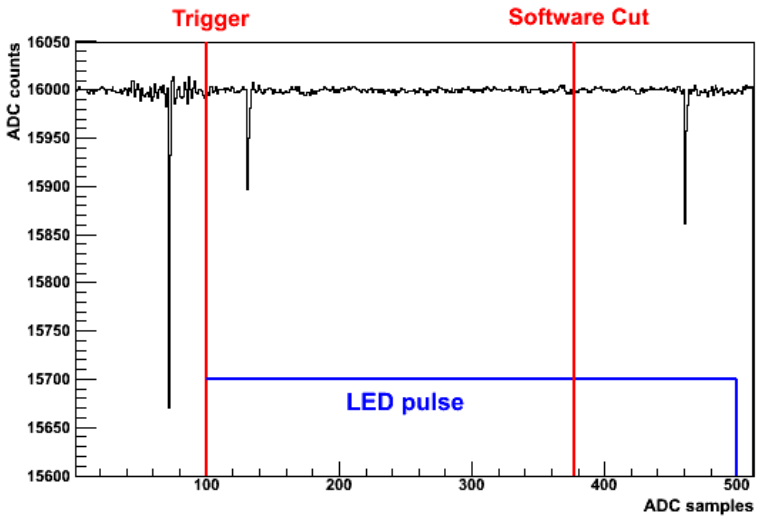

Figure 5.9: Partition of a waveform stored during LED calibration. The first µs (100 samples) is taken before the LED signal and is used to determine noise and dark counts. The other 4µs (400 samples) are taken during the LED signals. This window is shortened by a software cut in order to equalise the light level on all PMTs. Only signals between the trigger and the software cut constitute the SPE spectrum, while peaks before the trigger are counted to the no-LED data, and peaks after the software cut are discarded.

brightly illuminated PMTs, ensuring that the signal-to-noise ratio does not exceed 95% (see Fig. 5.9). The first 100 samples of each waveform, which have been recorded before the LED signal, are used to determine the baseline. The negative signals of the PMTs are then inverted by subtracting the ADC counts in each sample from the baseline. A peak finding algorithm is used to determine the maximum amplitude in the waveform and integrates the ADC counts from 5 samples before to 5 samples after the peak position. The integrated ADC counts are then converted to electrons using the formula

$$1 \text{ integrated ADC count} = \frac{R \cdot A \cdot \nu \cdot e}{res} \text{ signal electrons}, \tag{5.1}$$

where $R = 50\ \Omega$ is the input impedance, $A = 10$ is the amplification factor of the amplifier modules before the ADC, $\nu = 100$ MHz is the ADC sampling frequency, e is the electron charge and $res = (2.25\ \text{V})/2^{14}$ is the resolution of the ADC module.
For each PMT the maximum amplitude from each event, converted to signal electrons, is filled in a histogram, resulting in the single photoelectron (SPE) spectrum of this PMT

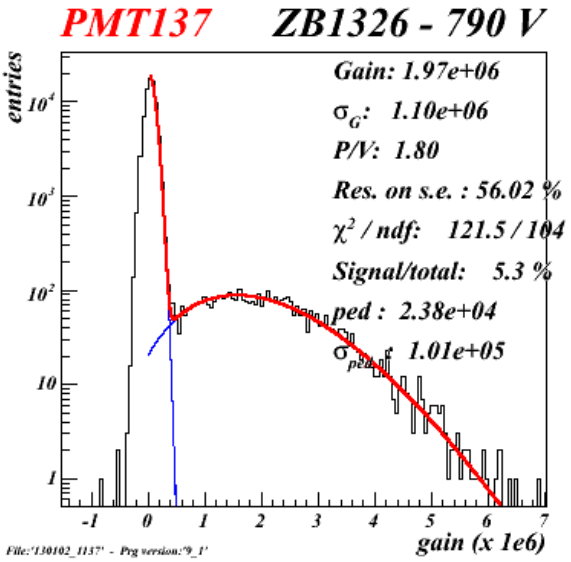

Figure 5.10: Typical SPE spectrum of a PMT as determined during a weekly LED gain calibration of the XENON100 PMTs.

(Fig. 5.10). The histogram is fitted with the following function [89]:

$$f(x) = A_n \cdot e^{-\frac{(x-\mu_n)^2}{2\sigma_n^2}} + A_1 \cdot \frac{\frac{\mu_1}{b}\frac{x}{b}}{\Gamma(\frac{x}{b}+1)e^{\frac{\mu_1}{b}}}, \tag{5.2}$$

where A_n is the amplitude, μ_n the mean and σ_n the resolution of the noise peak; A_1 and μ_1 the amplitude and the mean of the SPE peak; b is a scale parameter constant for each PMT, and

$$\Gamma(x) = \int_0^\infty t^{x-1}e^{-t}dt \tag{5.3}$$

is the gamma function. The gain of the PMT can then directly be determined as the μ_1 from the fit. While Gauss functions are usually used to fit PMT spectra they don't describe well the spectra of PMTs with low amplification at the first dynode stage. The function used here, based on the assumption that the secondary electron emission at the dynodes follows poissonian statistics, has been found to fit the spectra of the R8520 PMTs better. A gaussian function is still used to describe the noise peak. As sometimes several noise components are observed, resulting in the overlay of several Gauss-distributed peaks, the fit starts from the noise peak position of the noise population with the highest amplitude, i.e. the one closest to the signal peak.

Together with the gain of the PMTs the dark count rate is also monitored. For this the number of peaks more than 300 ADC counts from the baseline is counted in the time span before the LED trigger. In August 2011 the monitoring of the rate of peaks more than 30 ADC counts from the baseline, the usual trigger threshold during normal data taking, was added to the list of monitored values. It is important to note that these two rates, usually in the order of 10 Hz for signals exceeding 300 ADC counts and 100 Hz for signals with more than 30 ADC counts do not represent the pure dark count rate. While dark counts make up a sizeable fraction of events in this no-LED data, there are also contributions from scintillation signals in the detector and electronic noise, especially in the rate of signals only 30 ADC counts from the baseline. This electronic noise is a common occurence especially in the PMTs 157 - 178, which are all connected to the same filter box. A sample waveform of electronic noise being counted to this no-LED data rate can be found in Fig. 5.11. When a PMT is found to have strongly increased in one of these numbers the waveforms are inspected by eye in order to establish whether the cause lies in dark counts or electronic noise.

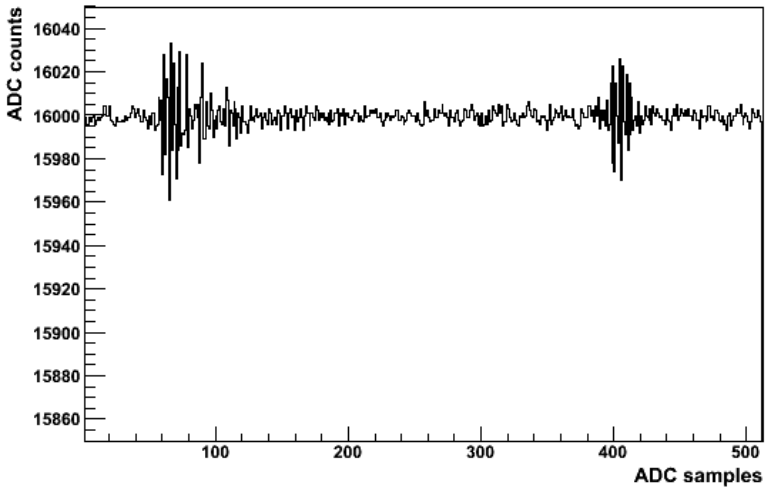

Figure 5.11: Example of a waveform including electronic noise faking a signal in the first microsecond of the waveform.

5.2.1 Gain Stability of PMTs in XENON100

The XENON100 detector has been running for more than four years without being opened. During this time it has gone through eight cooling cycles, the longest stable period being run10, which lasted for twenty months. The 242 PMTs inside have been operating almost continuously over the whole period without the possibility to exchange broken PMTs. The status of the PMTs has been closely monitored in weekly LED calibrations. With the hardware system for the calibrations being permanently in place LED data taking takes less than 20 minutes, and analysis, which is mostly automatised, and manual inspection of the status of all PMTs takes less than a day, allowing quick reactions to changes in the PMT behaviour. In run10 alone 107 such gain calibrations have been performed.
When the detector was closed in 2008 all PMTs had been confirmed to be working. Since then only 15 PMTs had to be switched off at some point. The most common reason for this has been repeated tripping, which occured in 11 PMTs. Additionally, two PMTs stopped to show any signal, and two PMTs have been switched off because of their excessively high dark current.
While it has been found that PMTs can fail at any moment without a clear cause, PMT failing has occurred mainly after a cool-down of the detector, especially at the beginning of run 5, the first run after the last opening of the detector (see Fig. 5.12).

The other PMTs have been found to be very stable. When closing the detector, all PMTs had been equalised to a gain of $2 \cdot 10^6$ by adjusting the PMT voltages. From then on the actual gain of every PMT has been determined from the SPE spectrum with each LED calibration and compared to the previous measurements. One of the evolution plots can be found in Fig. 5.13. Typically the gains have been stable within 2 % of the average value. However some drifting of the gains and especially larger leaps between different runs have been observed. Typically the majority of the PMTs changes in the same direction. For this reason the evolution of the average gain of all PMTs in the TPC is also monitored (Fig. 5.14), as large jumps in this number can hint to general problems in the detector's stability.

For the analysis of dark matter data it is important to know the gain of each PMT in order to convert the PMT output to the number of initial photoelectrons. For this purpose the mean gain of each PMT from all calibrations within one run has been calculated. Fig. 5.15 shows these values that have been used in run8 and run10 for each PMT.

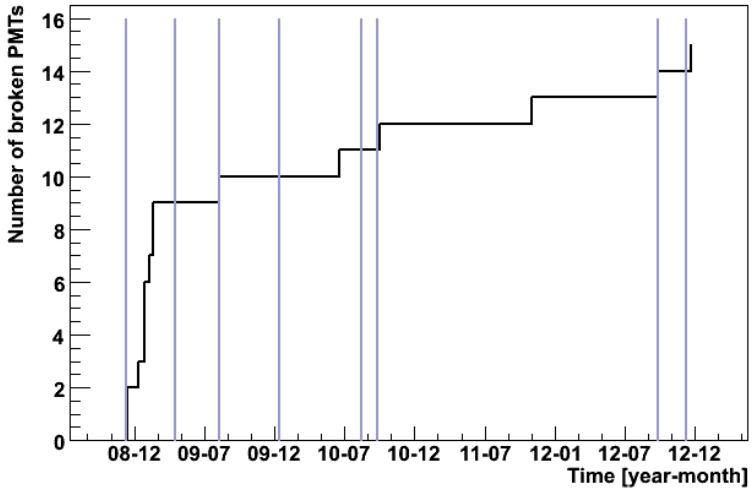

Figure 5.12: Number of failed PMTs in XENON100 over the course of its operation. The blue vertical lines mark the beginnings of new runs. PMT breaking often happens during or shortly after cool-down.

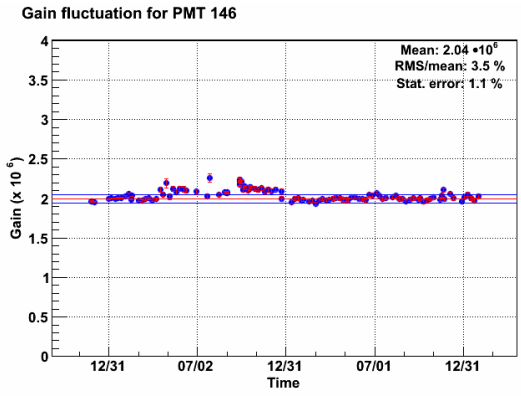

Figure 5.13: Evolution of the gain of one PMT in XENON100.

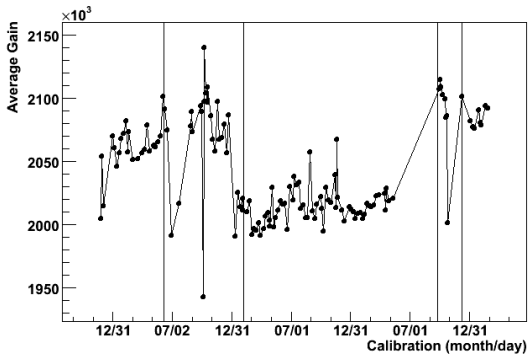

Figure 5.14: Evolution of the average gain of all PMTs in XENON100.

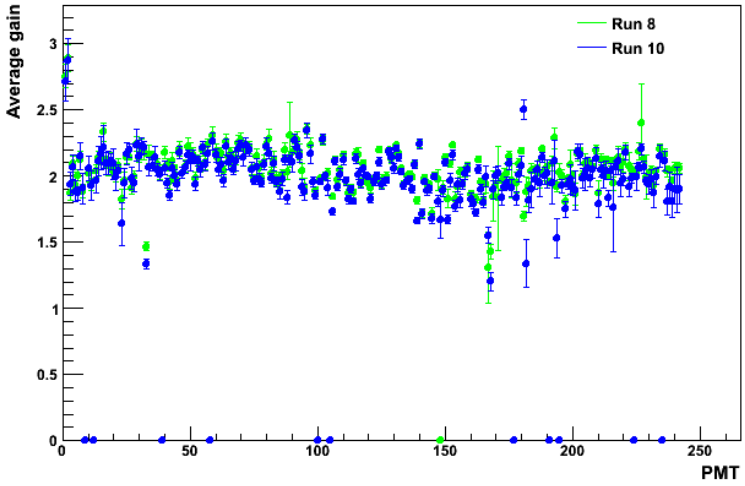

Figure 5.15: Average gain of each PMT used in analysis for run8 and run10.

Three PMTs have been showing sudden changes in gain. PMT 33 had been showing no signal for several weeks before returning to a new, lower, but stable gain (see Figs. 5.16 - 5.19). PMT 184 showed a sudden decrease in gain. For this PMT the voltage has been increased to return it to the nominal gain of $2 \cdot 10^6$ (Fig. 5.20). The third PMT, PMT 220, displayed a sudden lower gain which seemed to be stable for some time, but then started increasing again (Fig. 5.21). The reason for these gain changes has not been found. For these PMTs a fixed mean gain for analysis has been determined for each stable period individually.

5.2.2 Dark Counts and Electronic Noise

As shown in section 5.2 the "no-LED data rate" that is measured with each gain calibration helps to monitor the stability of the PMTs, but does not directly depict the dark count rate. The measurement of the dark count rate is however necessary in order to calculate the number of expected background events from accidental pile-up with dark counts in the XENON100 dark matter search data. For such an event a coincidence of dark counts from at least two PMTs within 178 µs before an S2-like signal is necessary. The dark counts would then be treated as the S1 signal.
To retrieve a more accurate number of dark counts from the no-LED data two cuts are

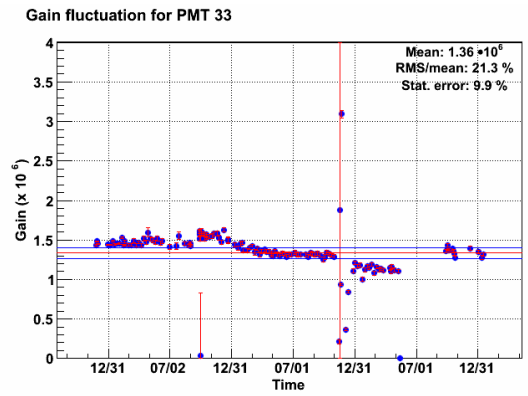

Figure 5.16: Evolution of the gain of PMT 33.

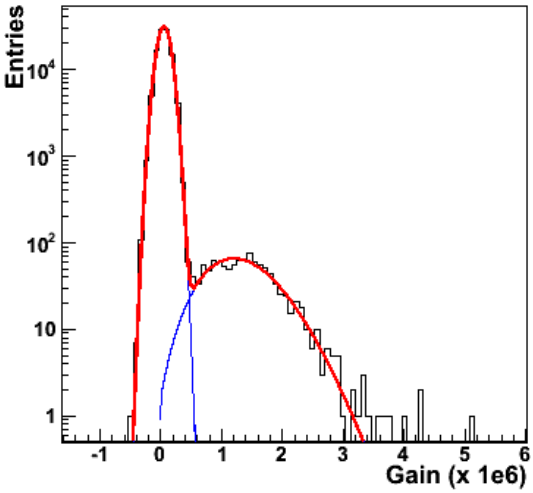

Figure 5.17: SPE spectrum of PMT 33 on October 31st 2011, gain: $1.29 \cdot 10^6$.

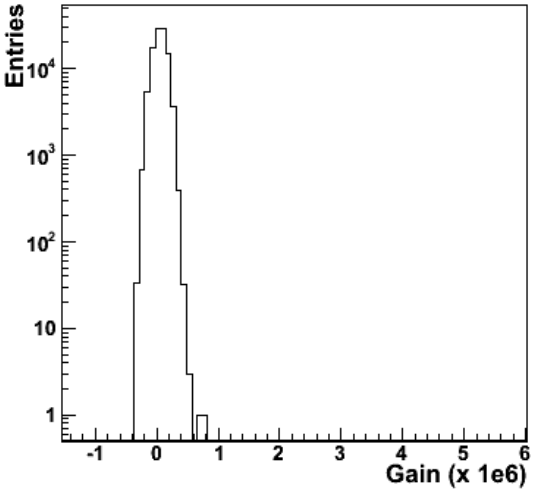

Figure 5.18: SPE spectrum of PMT 33 on November 17th 2011, no signal.

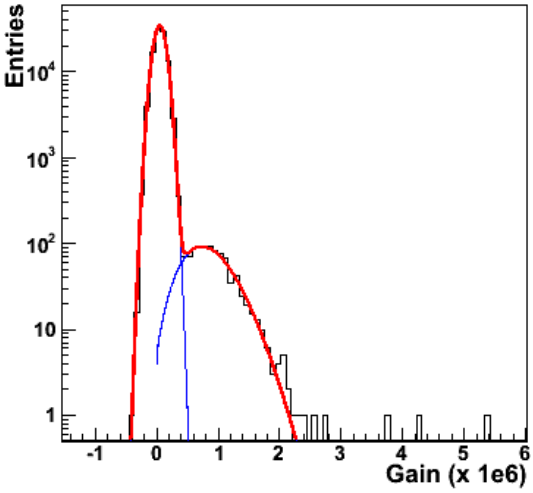

Figure 5.19: SPE spectrum of PMT 33 on December 12th 2011, gain: $8.45 \cdot 10^5$.

used that reject electronic noise. The most common type of electronic noise that can be mistaken for dark counts is in the form of high-frequency bursts, such as in Fig. 5.22.

In order to reject these events the area of 10 samples before and after the alleged peak

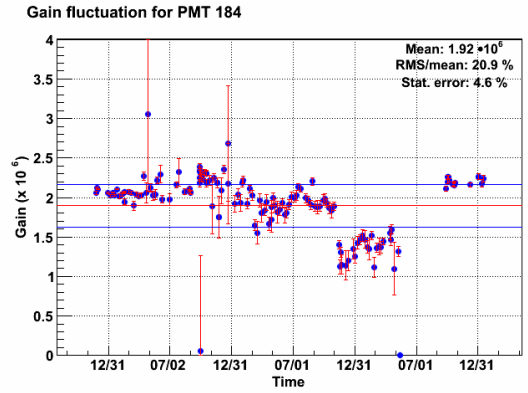

Figure 5.20: Evolution of the gain of PMT 184.

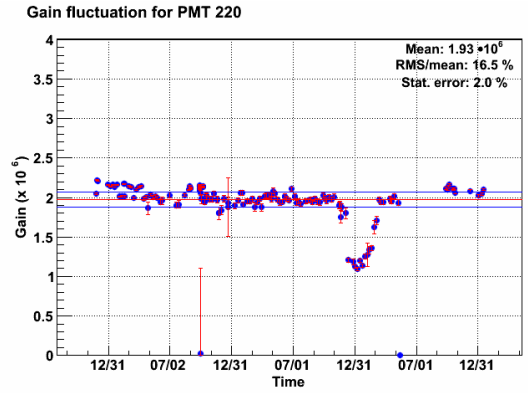

Figure 5.21: Evolution of the gain of PMT 220.

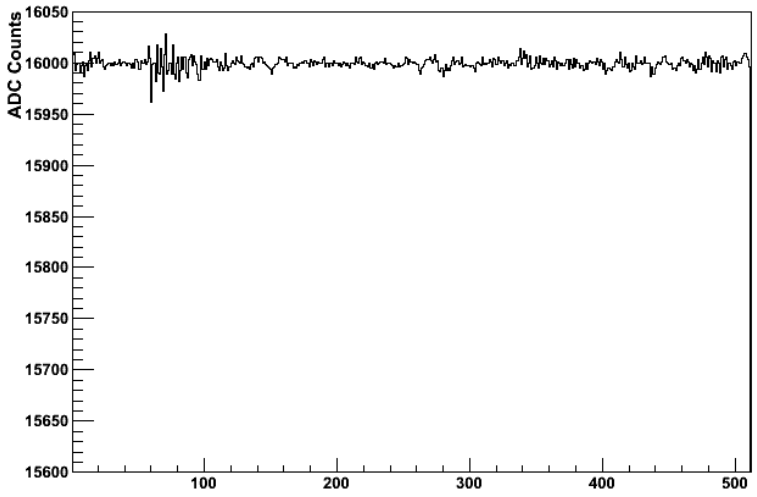

Figure 5.22: High-frequency electronic noise within the first μs of a waveform in an LED calibration. This noise can be misidentified as dark counts, but it is rejected by cut 1.

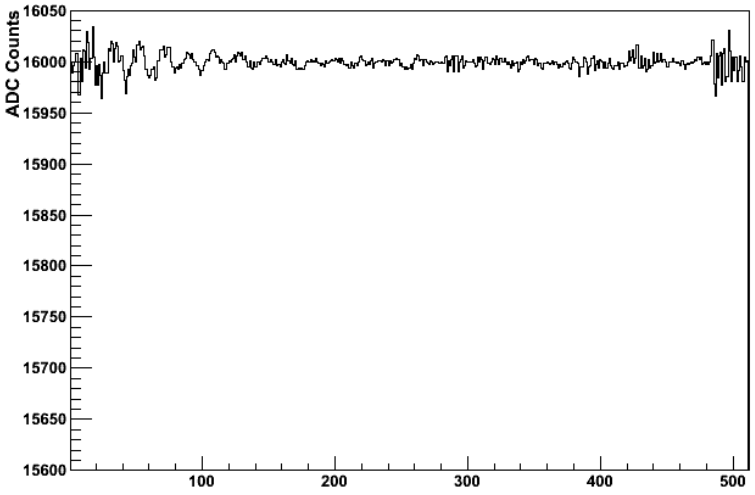

Figure 5.23: Low-frequency electronic noise within the first μs of a waveform in an LED calibration. This noise can also be misidentified as dark counts, but it is rejected by cut 2.

position is investigated and the number of times the waveform crosses the baseline within this region is counted. If the peak position lays within the first 10 samples of the waveform the investigated region is shifted to cover the 20 samples after the peak instead. For an event not to be rejected as high-frequency electronic noise it needs to pass cut 1:

$$N_{bc} < 3, \tag{5.4}$$

with N_{bc} being the number of times the waveform crosses the baseline in the region of interest.

Less often observed is a low-frequency contribution to electronic noise, such as in Fig. 5.23. These events are often not rejected by cut 1. For this reason in the same region around the peak position as the one used for cut 1 the total area between the waveform and the baseline is also integrated. In a noise event this area will be close to zero, since the parts above and below the baseline cancel each other out, while for a real event the area will be much closer to the actual area of the peak. Low-frequency electronic noise events are therefore rejected by cut 2:

$$A_{tot} > 30, \tag{5.5}$$

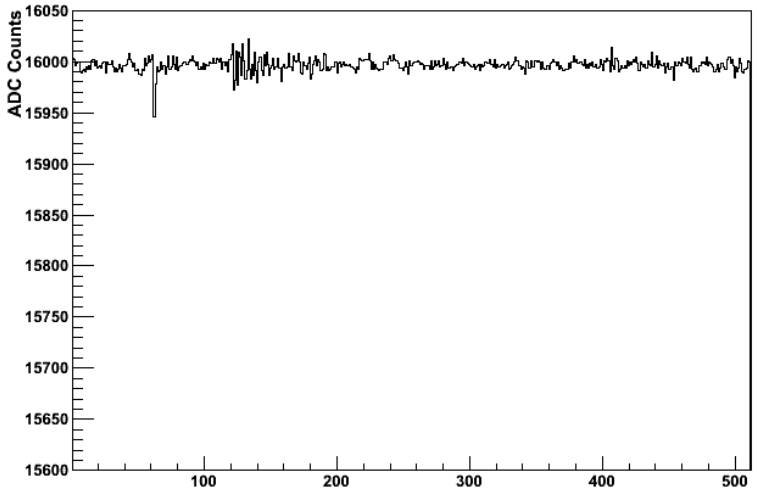

Figure 5.24: A valid dark count event passing both cuts.

where A_{tot} is the integrated area around the peak.
An example of a waveform that passes both cuts can be found in Fig. 5.24. It is from the same measurement and the same PMT as Figs. 5.22 and 5.23. While high-frequency electronic noise is present in this waveform as well, the peak found in the first µs of the waveform is from a valid dark count.

The average dark count rate in run10 for each PMT, as derived from the gain calibrations using those cuts, is shown in Fig. 5.25. A clear difference can be found between the first 178 PMTs, which are installed inside the TPC volume, and the last 64 PMTs observing the veto. Furthermore PMTs sitting in the centre of the top array seem to have a higher dark count rate than the ones on the border of the volume, and the PMTs in the bottom array have a higher dark count rate than those in the top array. One possible explanation lies in the placement of the PMTs: the PMT in the bottom array are of a newer type that has a higher quantum efficiency. The PMTs that showed the best performance in black box tests before installation have been put in the centre of the detector. It is possible that higher quantum efficiency correlates with higher dark current. In fact all XENON100 PMTs that clearly show excessive dark current can be found in the bottom array.
However it is likely that the PMTs inside the TPC volume still see some real light even without the LED, e.g. from background radiation leading to scintillation in the chamber.

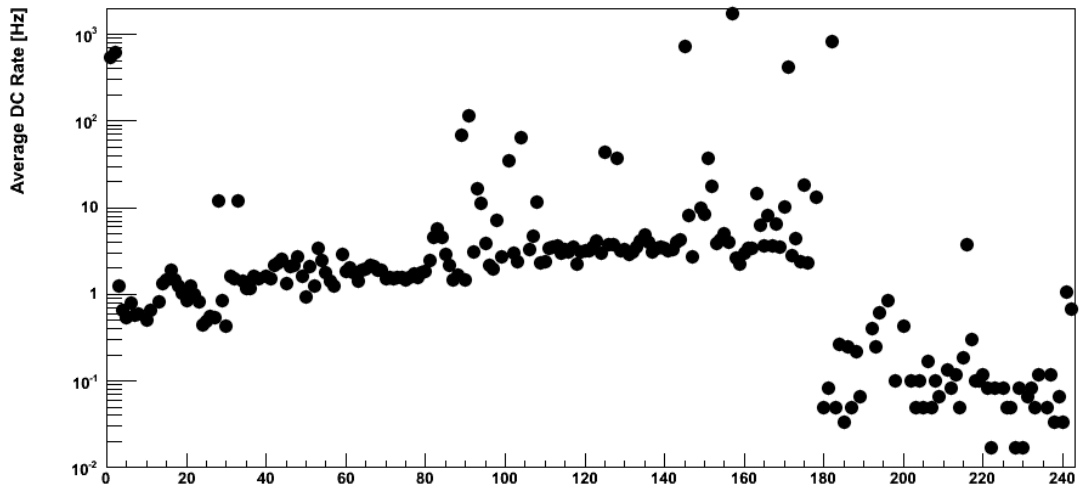

Figure 5.25: The average dark count rate in run10 for the individual PMTs.

Since these events, when in the size of single photoelectrons, are indistinguishable from dark count events they can not be subtracted from the dark count rate. As the combined rate of dark counts and single photoelectron background events should be the same during LED calibration dark time and science data taking it will be used in this form in the following analysis.

For dark counts being mistaken for real S1 signals at least two of them need to be in coincidence, followed by an S2 signal that is not already associated with a valid S1 signal. The average dark count rate in run10 over all working PMTs has been 25.4 Hz. For the inner PMTs the rate was 29.4 Hz. Seven of these PMTs have however been excluded from the peak finding algorithm: PMTs 1 and 2 which are connected to the same filter box as the anode and show a lot of noise on top of a poor single photoelectron spectrum, and PMTs 145, 148, 157, 171 and 177 because of their excessively high dark current. Together with eight PMTs in the inner volume that have been switched off completely there are thus 163 PMTs left that can contribute to an S1 signal. The average dark count rate of these 163 PMTs is 10.8 Hz. The rate at which dark counts from two different PMTs included in the peak finding algorithm will coincide within the S1 time window of 30 ns

is then given by [92]

$$R_{acc} = \frac{163 \cdot (163-1)}{2} \cdot (10.8 \text{ Hz})^2 \cdot 30 \text{ ns} = 0.046 \text{ Hz}. \tag{5.6}$$

This rate seems high, but in order for these coinciding dark counts to be confused with a xenon scintillation signal a corresponding S2 signal that is not already connected to a S1 pulse is also necessary. These "lonely" S2 signals can occur for various reasons: The S1 pulse could be too small, or be missed by the PMTs due to the imperfect light collection and quantum efficiency. It is also possible that the S1 and S2 signals are too close to each other in time to be properly distinguished.
The number of lonely S2 signals in run10 has been determined from the actual data, counting S2 signals within the 34 kg fiducial volume that contain less than 1000 photoelectrons and are not connected to an S1 signal. A total of $N_{S2} = 19068$ such events has been found [92]. Using these numbers a total of

$$N_{DC} = N_{S2} \cdot R_{acc} \cdot dt = 19068 \cdot 0.046 \text{ Hz} \cdot 145\mu\text{s} = 0.13 \tag{5.7}$$

events can be expected in run10 which come actually from two coinciding dark counts within the maximum allowed drift time window of dt = 145 μs before a lonely S2 signal.

Chapter 6

The Hamamatsu R11410 PMT

The detection principle of the XENON experiment relies on the measurement of light signals. When a WIMP scatters off a xenon nucleus first the very small direct scintillation light S1 signal is created. The ionisation charge is then drifted in the electric field of the TPC to the gas phase where a secondary, larger light signal S2 consisting of up to hundred thousands of photons (see Section 7.1) is created proportional to the charge. In order to detect these light signals a photosensor is required. This chapter describes the testing and preparation of the Hamamatsu R11410 photomultiplier tube which will be used for this task in XENON1T.

6.1 Requirements for Photosensors in the XENON1T Detector

The high sensitivity that is necessary for dark matter detection as well as the special conditions in a liquid xenon environment set a number of requirements for a photosensor to be used in the XENON1T detector. The most obvious one is that it needs to be able to detect the xenon scintillation light which has a mean wavelength of 178 nm. For the detection of S1 signals as small as a single photon, a photosensor with high quantum efficiency, good single photon resolution and good space coverage is necessary. At the same time any dark current or electronic noise must be kept as low as possible. For the much larger S2 signals on the other hand good linearity over a wide dynamic range is essential. In order to reconstruct the interaction vertices, either several smaller photosensors have

to be used or larger photosensors that themselves provide some segmentation of their sensitive area. In both cases any cross-talk has to be avoided.
While the expected rate of WIMP signals is very low, the photosensors should be able to also handle much higher rates (in the order of several 100 Hz) during calibration of the detector.
One of the main concerns in rare event searches such as the XENON experiments is the background from the detector itself. It is therefore of high importance that the photosensors are extremely low in radioactivity and of course they should also not produce any light themselves inside the TPC.
In a liquid xenon TPC the photosensors need to be working stably and reliably over long periods of time without the possibility to easily exchange failing photosensors. They need to survive the cool-down cycle where the temperature changes from 300 K down to 180 K and the pressure changes from very high vacuum to 2 bar and stay operational under the liquid xenon conditions. They also must not introduce impurities into the ultra clean xenon or heat, that in the worst case could lead to bubbles in the detector.
Some of these properties depend not only on the PMT itself, but also on its voltage divider base. The design of a suitable base is described in Chapter 7. In this chapter the characteristics of the PMT itself are discussed.

6.2 The Hamamatsu R11410 PMT

For XENON1T the Hamamatsu R11410 photomultiplier tube (Figs. 6.1 and 6.2) has been chosen as photosensor. This new PMT has been developed specifically for the use in liquid xenon. It has a round window with a diameter of 76 mm. Due to its special photocathode and a synthetic silica window transparent to UV light it is capable of efficiently detecting the xenon scintillation light, which has an average wavelength of 178 nm, without any additional wavelength shifter. Like its sibling, the R11065 PMT that has been designed for the operation in liquid argon and is different only in the photocathode, it can withstand temperatures down to 87 K [93] and pressures up to 6 atm [94]. The bialkali photocathode has a high quantum efficiency of more than 30%. The PMT uses twelve dynode stages (visible in Fig. 6.3) and reaches a gain of around $5 \cdot 10^6$ at its recommended supply voltage of –1500 V.

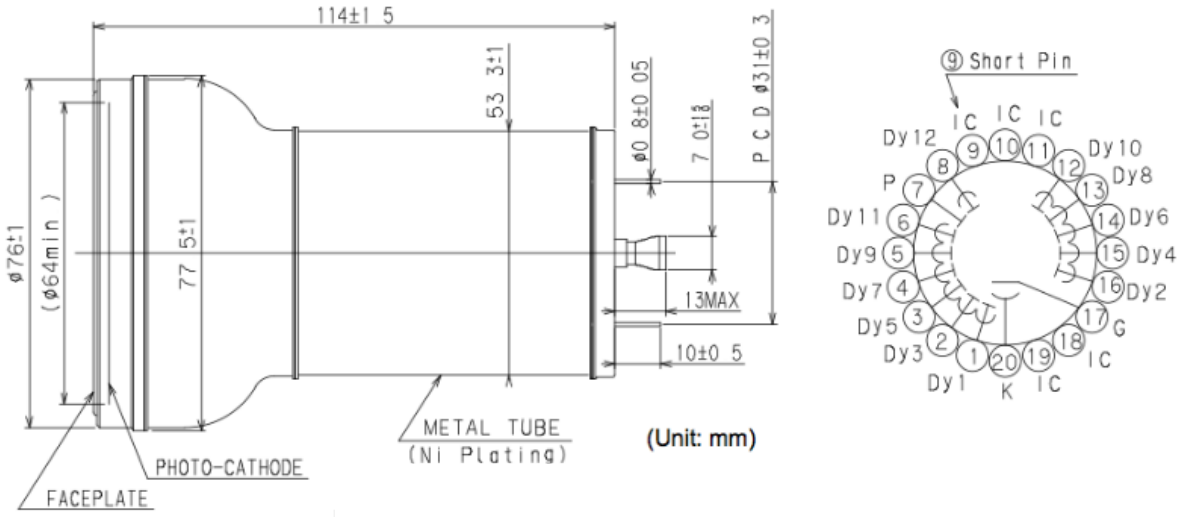

Figure 6.1: Geometry and pin layout of the Hamamatsu R11410 PMT, taken from the PMT's data sheet.

Figure 6.2: The Hamamatsu R11410 PMT.

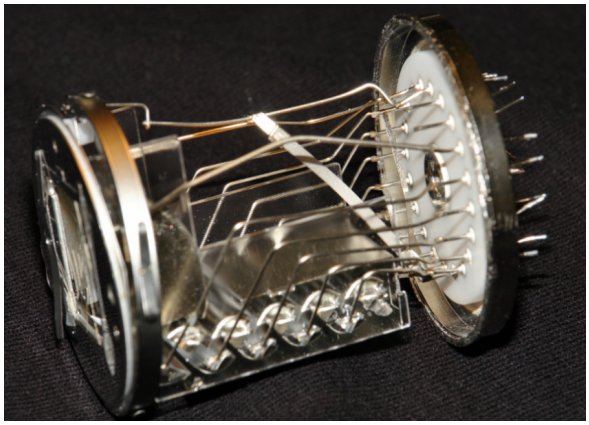

Figure 6.3: Inside dynode structure of a broken R11410-10 PMT. Photograph from [65].

One design goal of the R11410 was to reach ultra low radioactivity. The original version of this PMT, while already cleaner (normalised to sensitive area) than the R8520 used in XENON100, did not meet the requirements yet. A second version, the R11410-MOD, which was later renamed R11410-10, brought vast improvements (see Table 6.1).

	R8520 [mBq/cm^2]	R11410 [mBq/cm^2]	R11410-MOD [mBq/cm^2]
^{238}U	0.023±0.005	0.13±0.02	0.07±0.04
^{232}Th	0.026±0.005	0.07±0.01	0.033±0.004
^{40}K	1.7±0.2	1.1±0.2	0.30±0.05
^{60}Co	0.090±0.008	0.18±0.02	0.09±0.02
Sum	1.8 ±0.2	1.5±0.2	0.49±0.06

Table 6.1: Comparison of screening results for R11410 and R11410-MOD and the R8520 [81] that is currently used in XENON100. All results have been obtained by the XENON screening group with the Gator germanium detector [95].

Figure 6.4: R11410 (left) and R11410-MOD (right). The glass stem has been replaced by a ceramic one, reducing the radioactivity of the PMT.

This reduction has been achieved by replacing materials with specially selected low-radioactivity alternatives. Notably the glass stem of the PMT has been replaced by a ceramics stem (Fig. 6.4).

6.3 Test Set-Ups

6.3.1 Black Boxes

While the PMT is intended to be used in liquid xenon, most tests can be done faster and easier at room temperature. For this purpose two light-tight black boxes have been built, one small (25 cm x 25 cm) suitable for the testing of one R11410 PMT at a time, and one larger (90 cm x 90 cm) which can accommodate several PMTs at once and more elaborate test set-ups. Both black boxes have been built from polyvinyl chloride (PVC) and have a lid that is additionally sealed with black rubber foam to make it lightproof (Fig.6.6). All cabling is lead through a bent PVC tube that is then optically sealed with more foam material (Fig.6.7). The boxes are covered on the outside with aluminium foil

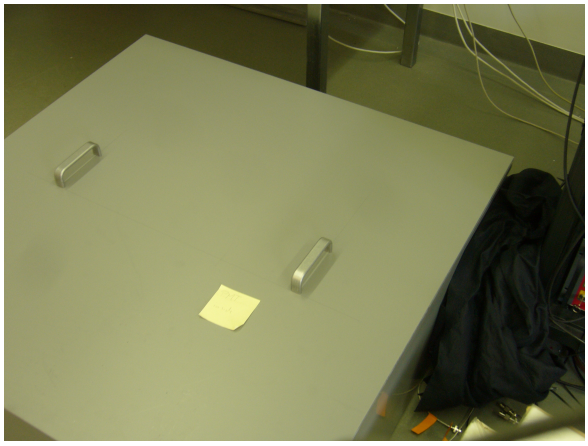

Figure 6.5: Black box for room-temperature PMT tests.

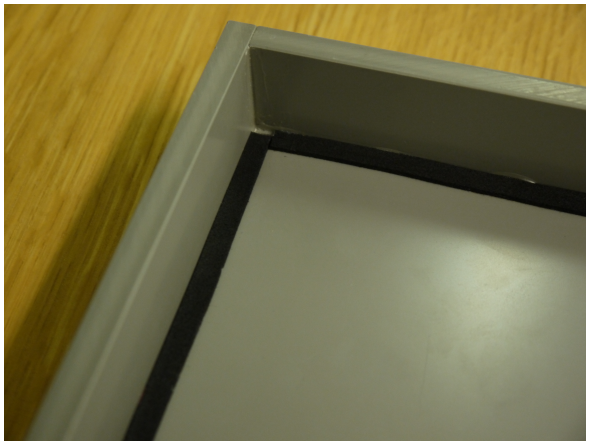

Figure 6.6: Sealing of the black box lid.

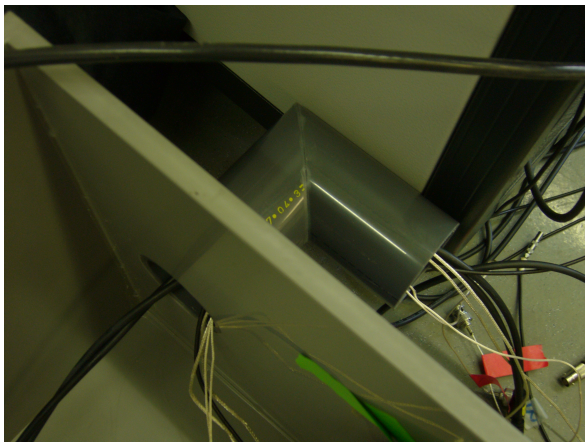

Figure 6.7: Cable guide into the black box.

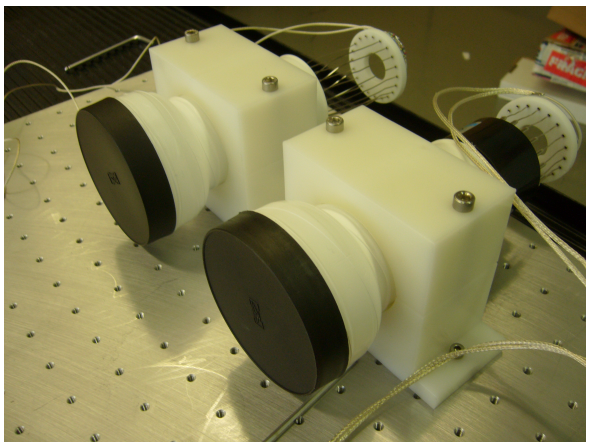

Figure 6.8: Custom designed PTFE fixtures for mounting R11410 inside the large black box.

and black felt for both electrical and additional optical shielding.
A PTFE fixture is used to keep the PMTs in place inside the box. The oval form of the cut-out allows to tighten without damaging the PMT. In the big black box this fixture can additionally be screwed onto a metal plate on the floor of the box (Fig. 6.8). The PTFE also provides the necessary insulation from the metal case of the PMT which is connected to the photocathode and thus set to high voltage during operation.

6.3.2 MarmotX

For tests in liquid or gaseous xenon a small test chamber, called MarmotX, was built (Fig. 6.9). It can hold one PMT at a time in a PTFE structure which doubles as filler so that the amount of xenon that is necessary to fill the chamber is minimised (Fig. 6.10). The PMT faces downwards onto a small xenon volume, sitting on a PTFE ring around this volume that also acts as a light reflector together with a PTFE plate on the bottom of the chamber. Because PTFE contracts at liquid xenon temperatures the PMT could be crushed if it was held too tightly. To avoid this there is some space between the holding structure on top of the PMT and the PMT itself that allows the PMT to float up a few millimeters on top of the xenon when the chamber is filled.
In the long-time stability tests MarmotX was filled with ~ 300 g of xenon so that the front part of the PMT with the photocathode was submerged in the liquid while the pins with the base were in xenon gas.
MarmotX is cooled with cold nitrogen vapour. For this purpose the whole chamber sits on top of a Dewar vessel filled with liquid nitrogen just a few centimeters above the liquid level. The liquid nitrogen should not touch the chamber as it would freeze the xenon.
Temperature and pressure inside the detector are monitored by up to four PT100 temperature sensors (one mounted on the outside of the chamber, the others inside on the bottom, at the height of the PMT photocathode and on top) and one pressure sensor. The values are read every five minutes by a slow control system that creates plots for the measurements over time and sends alarm messages by SMS in case that one of these values crosses a predefined threshold, or the slow control system loses network connection. In the beginning the nitrogen Dewar vessel had to be refilled manually every two hours which required night shifts for long-time measurements. Later on an automatic refilling system consisting of a solenoid valve on a larger nitrogen Dewar vessel which is controlled

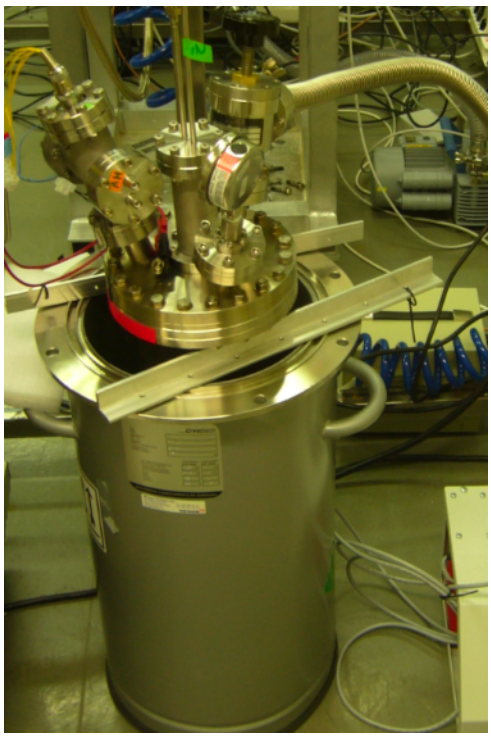

Figure 6.9: The MarmotX chamber. It is placed above the liquid nitrogen in the larger Dewar vessel without touching the liquid. The nitrogen vapour then provides cooling.

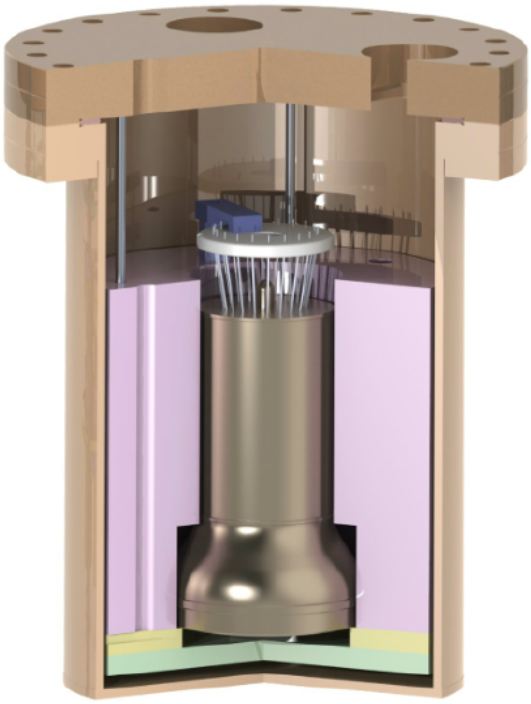

Figure 6.10: CAD drawing showing the inner structure of the MarmotX chamber, taken from [88].

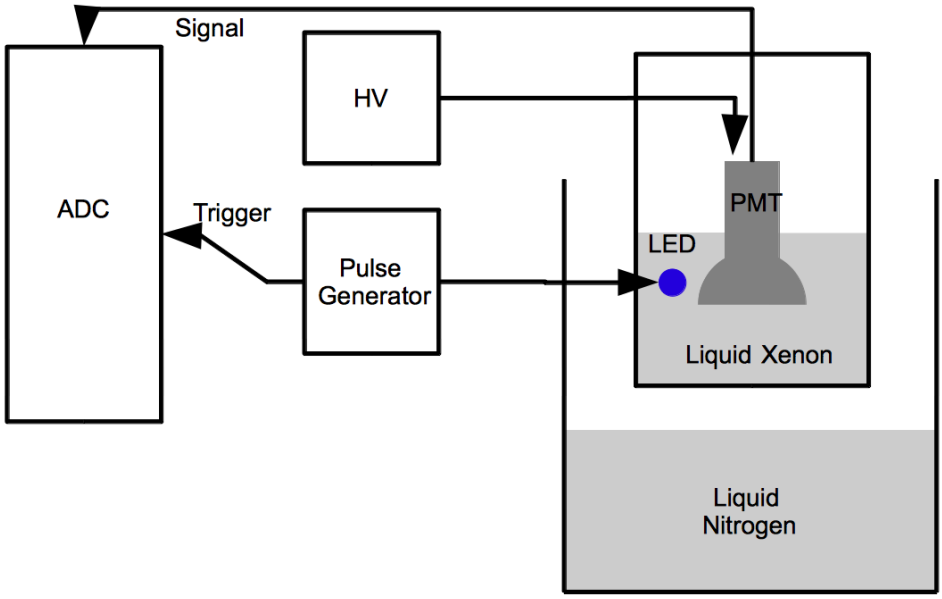

Figure 6.11: Schematic view of the test set-up in liquid xenon.

directly by the slow control system was used. Additionally a maximum of 25 W heating power can be supplied to the walls of the chamber via a 3 mm thick copper conductor. This not only allowed longer runs without the need of staying in the laboratory during nights and weekends, but also a much finer control of the operational conditions within the chamber and thus improved the overall stability.

6.3.3 MarmotXL

MarmotXL (Fig. 6.12) is a larger liquid xenon test chamber that can house three PMTs at the same time. The PMTs are mounted facing upwards in a PTFE holder on an aluminium structure (Fig. 6.13) that allows to vary the distance between the PMTs. This set-up can be used to study the influence of the electric fields between the PMTs when they are supplied with different high voltages, as it might be the case in XENON1T when the voltages of the individual PMTs will be adjusted to equalise the gains or when a broken of malfunctioning PMT has to be switched off.
In MarmotXL the PMTs are facing a metal plate that can as well be set to high voltage, mimicking the electric fields that are present in a TPC like XENON1T. The distance

between this plate and the PMTs is also variable.
The chamber is equipped with two PT100 temperature sensors. MarmotXL is designed for tests in liquid xenon, however, for the tests described here only gaseous xenon at room-temperature has been used.

Figure 6.12: The MarmotXL chamber.

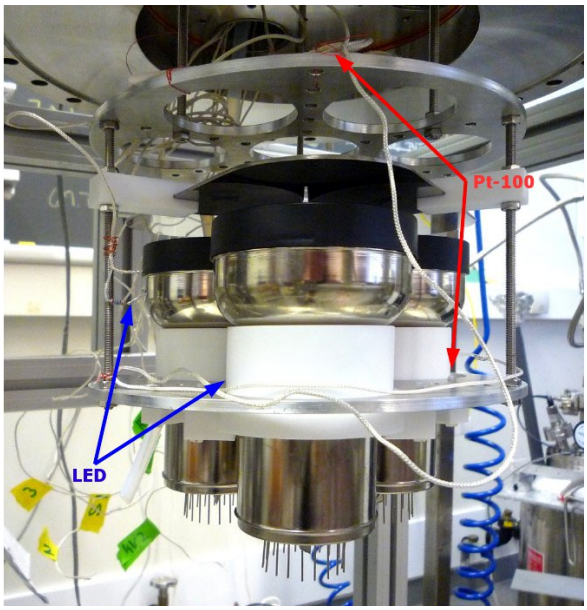

Figure 6.13: Inside set-up with three PMTs fixed. Photograph by A. James.

6.3.4 Data Acquistion

First tests were done using a multichannel analyser (MCA) together with an amplifier for the data acquisition. Most tests however were performed with the CAEN V1724 ADC board that is used in the XENON100 data acquisition system [48] and that will also be used in XENON1T.
The software for this ADC board has been developed specifically for these PMT tests and consists of three parts: a program for saving the raw or preprocessed data (miniDAX), a program for (re-)processing the saved raw data (miniProcess) and a program for plotting

the raw waveforms (miniWF). This software package is complemented by a bundle of bash and ROOT scripts that allow automatic data taking and analysis.
The central part of the data taking is done by miniDAX. It is configured via xml files and for each event it can either save all data for a predefined time period - including a selectable time span before the trigger - in various formats or quickly preanalyse the raw data while it is taken and save the results. The latter is used for example for linearity tests where the PMT signal has to be integrated for the same time span after each trigger from the pulse generator (see Section 7.1.3). It is also possible to not save anything but use the program in oscilloscope mode displaying the triggered events live on screen. The standard procedure in the PMT tests described here is saving 5 µs long waveforms of which 0.5 µs are taken pre-trigger as arrays in a ROOT tree.
For analysis this raw data has to be processed using miniProcess after the data taking. For each waveform it first calculates the level of the baseline by averaging over the first samples that are taken before the trigger and should therefore not contain any signals. The baseline level is stored together with the standard deviation. The latter allows to cut for example on waveforms that include dark counts or electronic noise before the trigger that would distort the baseline and thus lead to false values in the following calculations. Usually the baseline stays close to its set value of 16000 ADC counts.

The processor cycles now over the entire waveform and determines the amplitude for each sample as the difference between the baseline and the number of ADC counts in this sample. The start of a possible signal is defined as the sample at which the amplitude is greater than the "low threshold" given in the configuration file of the processing program for the first time. Unless there are significant problems with electronic noise the low threshold is usually set to 1 ADC count (Fig. 6.14). This deviation from the baseline is however only recognized as a true signal if the amplitude of one of the following samples also crosses a second "high threshold" which is also defined in the configuration file before it falls below the low threshold again which defines the end of the signal. If this is the case several parameters are computed for this signal (see Table 6.2 for full list): the peak position as the sample with the highest amplitude within this signal, the signal width as the number of samples from first to second crossing of the low threshold, the peak height as the maximum amplitude within the signal and the signal area that integrates the amplitude over the whole waveform. The signals within an event are sorted by signal

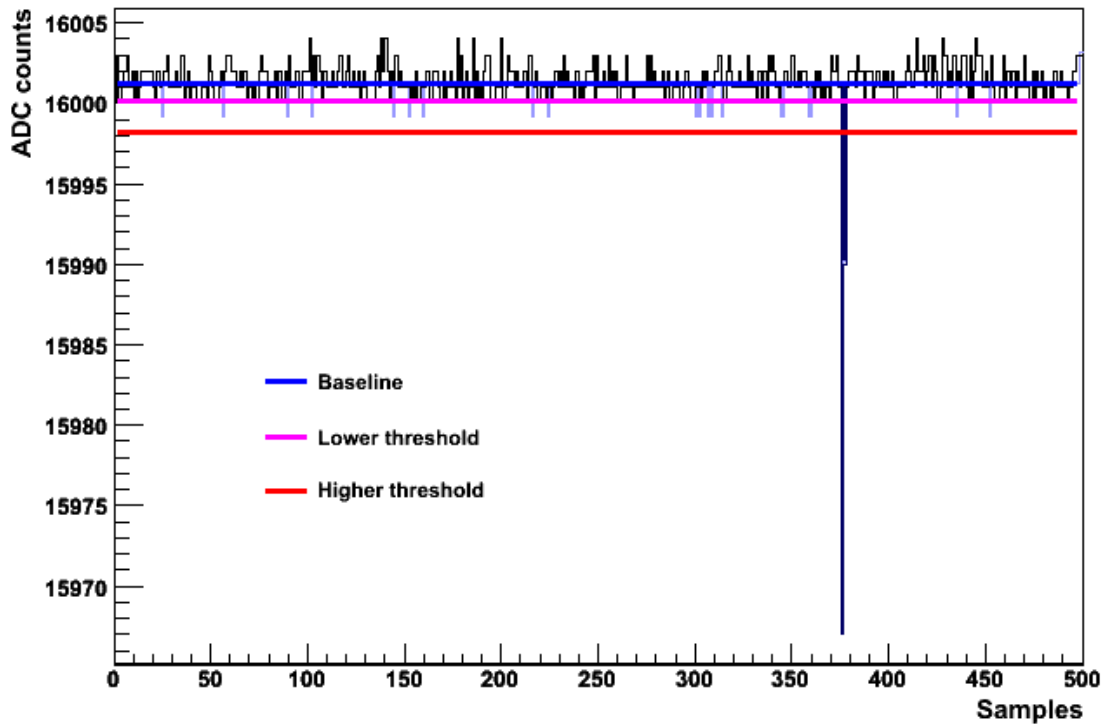

Figure 6.14: Waveform analysed with lower threshold = 1 and higher threshold = 3. The baseline has been calculated from the first 50 samples (pre-trigger region). The integrated area of each peak candidate is marked in light blue, but only one signal (dark blue) crosses the higher threshold. The other signal candidates are discarded.

Name	Type	Unit	Description
ver	char[4]	-	Version number of miniProcess
filename	char[23]	-	Name of the data set
evtnb	int	-	Number of the event within the file
lt	int	ADC counts below baseline	The low threshold that has been used for processing
ht	int	ADC counts below baseline	The high threshold that has been used for processing
wflength	int	ADC samples	Length of the stored waveform
trg	int	ADC samples	Position of trigger within the stored waveform
baselength	int	ADC samples	Number of samples in the beginning of the waveform that have been used for the calculation of the baseline
baseline	float	ADC counts	Average baseline determined from the pre-trigger samples
basesd	float	ADC counts	Standard deviation of the baseline
fi	int	integrated ADC counts	Full integral of the entire waveform with the baseline subtracted
sc	int	-	Number of signals that crossed the high threshold in the entire waveform
dc	int	-	Number of signals before the trigger that crossed the high threshold. Can be used to calculate the dark count rate
dc2	int	-	Number of signals before the trigger that crossed the high threshold but not (2*ht-lt). Can be used to calculate the dark count rate while excluding larger signals that are probably not dark counts
pi	int [10]	integrated ADC counts	Integrated signal area of the biggest 10 signals in the waveform, ordered by signal size (area)
ph	int [10]	ADC counts	Pulse height of the biggest 10 signals in the waveform, ordered by signal size (area)
pw	int [10]	ADC samples	Width from first to second crossing of the low threshold of the biggest 10 signals in the waveform, ordered by signal size (area)
pp	int [10]	ADC samples	Position of the sample with the highest amplitude within each of the biggest 10 signals in the waveform, ordered by signal size (area)
fpi	int	integrated ADC counts	Integrated signal area of the first signal crossing the high threshold after the trigger
fph	int	ADC counts	Pulse height of the first signal crossing the high threshold after the trigger
fpw	int	ADC samples	Width from first to second crossing of the first signal crossing the high threshold after the trigger
fpp	int	ADC samples	Position of the sample with the highest amplitude within the first signal crossing the high threshold after the trigger

Table 6.2: Data saved after processing with miniProcess

area and the ten biggest signals after the trigger are saved in the root tree. If less than ten peaks are found the remaining variables are set to zero. Additionally the first signal after the trigger is always saved. In SPE analyses usually only this first signal is used in order to avoid bias towards large signals.
The total number of signals in the waveform is saved as well as the number of signals before the trigger, which can be later used to estimate the dark count rate.
Additionally the total integral of the amplitudes in the entire waveform is calculated. When each event contains a maximum of one true signal the electronic noise cancels out and this number can be used instead of the pulse area of the first signal after the threshold. It has however not been employed in the analyses presented here.
miniDAX has been adapted in the frame of this thesis from the original miniDAX written by M. Schumann, which itself is based on the Wave Dump program by C. Tintori

(CAEN). The basic communication to the ADC board and the oscilloscope mode have been inherited from the previous program. It has been expanded to use all eight channels of the ADC module instead of only one at a time, and the data saving/preanalysis has been completely redone to fit the needs of the work presented here.
Both miniProcess and miniWF have been developed as part of this thesis project.

6.3.5 Noise Rejection

While the electronic noise in the measurements presented here was usually very low it was still occurring sporadically during the long-term stability measurements, probably induced from other experiments that were ongoing in the laboratory at the same time. This noise in the form of bipolar high frequency outbursts (Figs. 6.15 and 6.16) lead to a broader noise peak in the SPE spectrum resulting in an inaccurate fit and underestimation of the gain value.

The problem occurs when the first peak after the threshold actually belongs to such a noise cluster. In this case this peak will be of similar amplitude as the other peaks in the waveform. Furthermore the peaks will appear very close to each other. The weighted peak distance of the first and the ten largest peaks in the waveform, defined as

$$dist = \frac{fph}{fpw} \sum_{i=0}^{9} |ph[i] \cdot pp[i] - fph \cdot fpp| \tag{6.1}$$

with fph being the height, fpw the width and fpp the position of the first signal after the trigger and $ph[i]$ and $pp[i]$ the height and position of the ith largest signal in the trace, will be the smaller the more similar the first peak is to the other signals in terms of pulse height and peak position. Additionally, the fraction $\frac{fph}{fpw}$ tends to be larger for real signals. As the peak distance increases also for waveforms with multiple valid signals it is compared to the total area of the ten biggest peaks,

$$peaksum = \sum_{i=0}^{9} pi[i], \tag{6.2}$$

where $pi[i]$ is the integrated area of the ith biggest signal. The exact numbers of the cut have been adjusted with the actual data from noisy data sets. The resulting cut that has

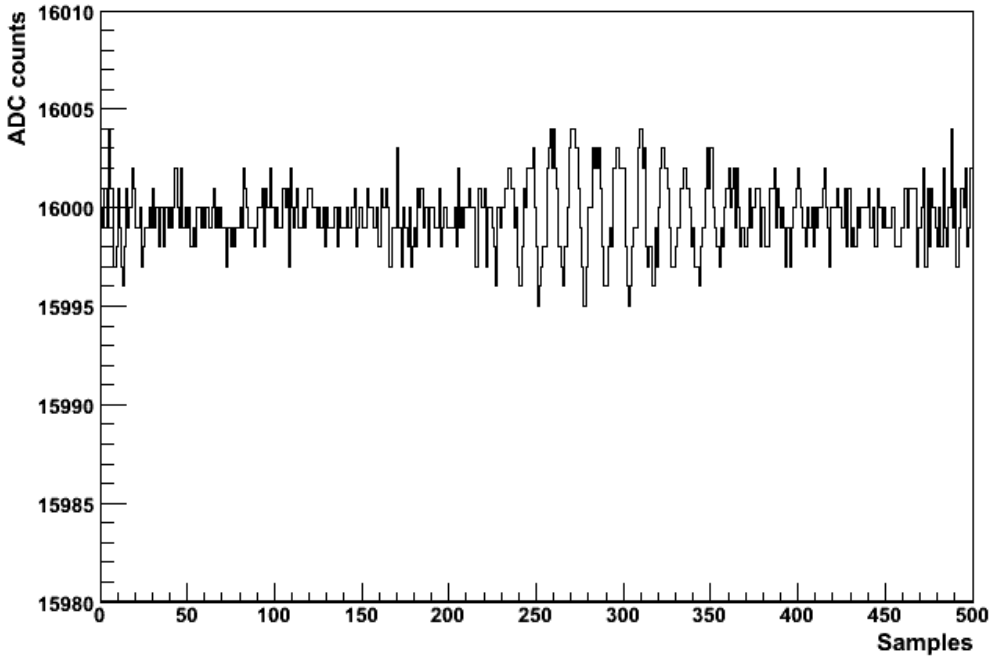

Figure 6.15: Waveform in which the first peak after the trigger (at sample 227) belongs to a noise outburst.

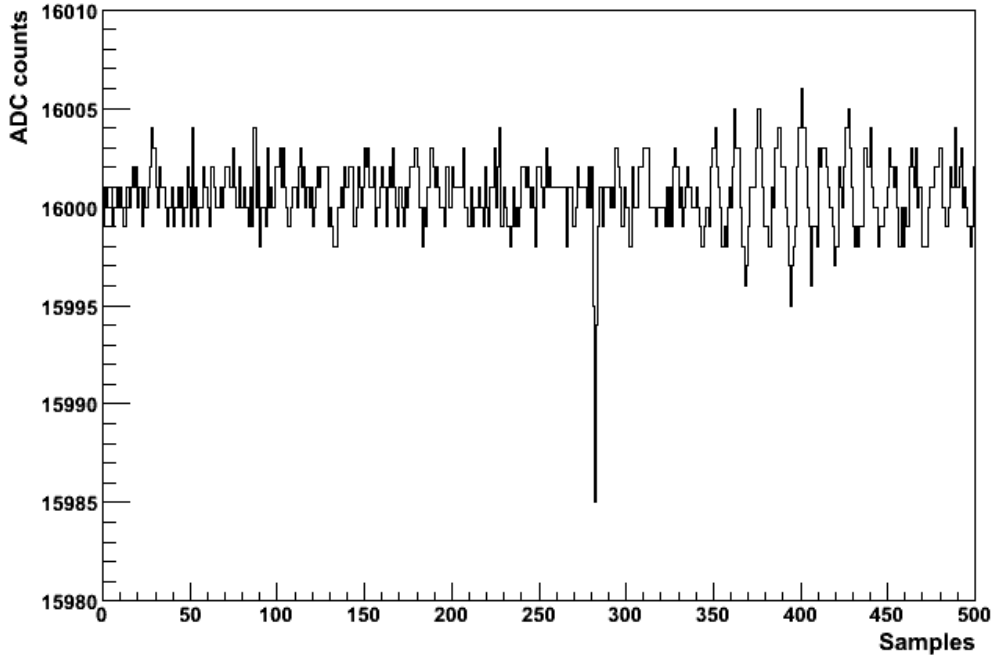

Figure 6.16: Waveform in which the first peak after the trigger (at sample 282) is a valid signal, while noise is also present in the waveform.

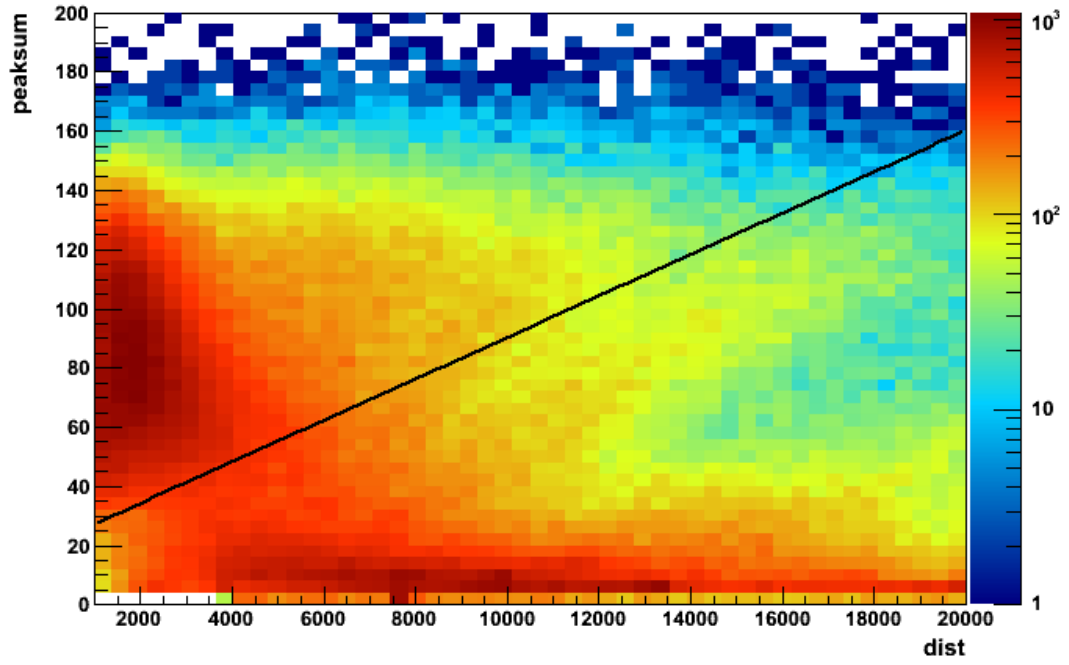

Figure 6.17: Distribution of the dist and peaksum parameters in a particularly noisy measurement. The black line indicates the anti-noise cut. Everything above this line is rejected.

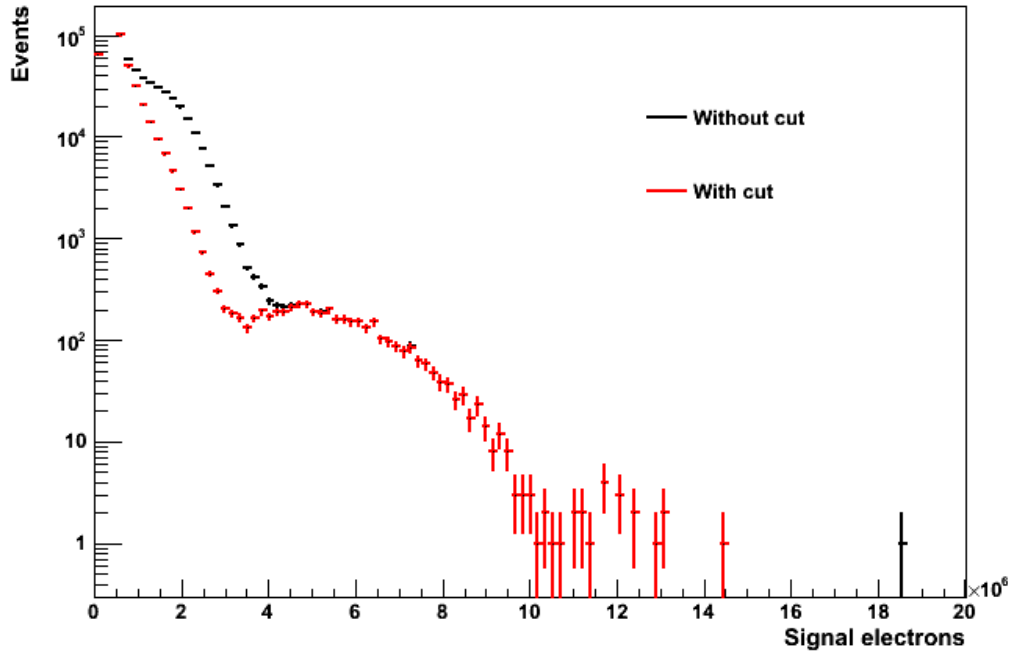

Figure 6.18: Effect of the anti-noise cut on the SPE spectrum. The second contribution to the noise peak is cut away, while the signal peak stays unaffected.

been used in the following analyses is

$$peaksum < 0.007 \cdot dist + 20. \tag{6.3}$$

The cut can be seen in Fig. 6.17, showing the distribution of the parameters *dist* and *peaksum* for a particularly noisy measurement. The black line shows the cut. The cluster of events above the cut corresponds to events where the first peak after the trigger is part of a noise outburst, while the cluster below the line represents valid events. All events above the line are rejected by the anti-noise cut.
For example the first peak after the trigger in the waveform shown in Fig. 6.15 belongs to a noise outburst. For this event $dist = 4335$ and $peaksum = 89$. The event is therefore rejected by the anti-noise cut. In the event shown in Fig. 6.16 the first peak after the trigger is a valid signal, separated from the noise outburst later in the same waveform. In this case $dist = 119051.25$ and $peaksum = 71$. This event is not rejected.
The effect of the anti-noise cut on the SPE spectrum from the same data set is shown in Fig. 6.18. The second contribution of the noise peak, corresponding to the additional bipolar noise is cut, while the rest of the noise peak, coming from normal baseline fluctuations, and the signal peak remain unchanged.

6.4 Performance of the R11410 PMT

A total of seven R11410 PMTs have been tested: two of the original R11410 type with serial numbers ZK4988 and ZK4990 (quantum efficiencies as measured by Hamamatsu: 38.8 % and 34.8 % respectively), two of the R11410-MOD (later named R11410-10) type with reduced radioactivity (serial numbers ZK5626 and ZK5629 with quantum efficiencies of 32.30% and 33.20% respectively) and three out-of-spec R11410-10 PMTs (KA0067, KA0068 and KA0070).
All PMTs have been checked in the black box. Additionally, three PMTs (ZK4988, ZK5629 and KA0067) have been tested in liquid xenon in the MarmotX detector. Furthermore, three PMTs (KA0067, KA0068 and KA0070) have been used in MarmotXL to determine the behaviour in the presence of electric fields and under increased pressure.

6.4.1 Single Photoelectron Response at Room Temperature

The single photoelectron (SPE) response has been tested in the black box using a blue (470 nm) LED to generate single photons. To this end, the LED has been driven by pulse generator signals, usually with a length of 4 µs and a repetition rate of 1 kHz. Data taking has been triggered on the LED signals by the pulse generator (Fig. 6.19). The voltage of the signals driving the LED has been chosen in a way that only about 2% of all triggered waveforms contain any signal. In this way the amount of multiple-photon events is highly suppressed.

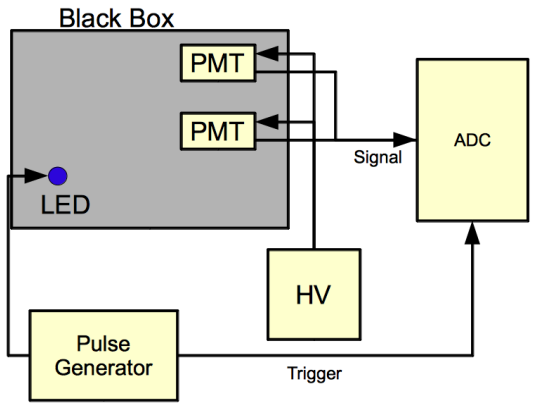

Figure 6.19: Set-up for room-temperature SPE measurements with blue LED light.

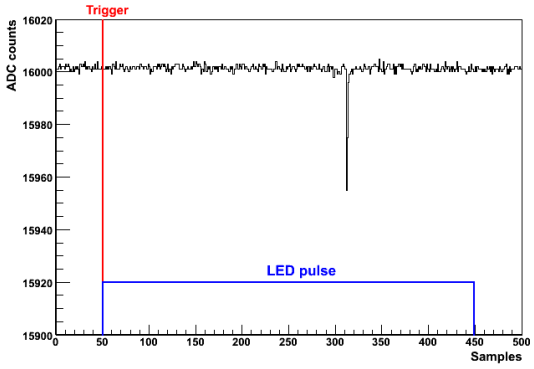

Figure 6.20: Waveform with SPE signal. The trigger at 50 samples (0.5 µs) starts both the DAQ and the LED pulse with a width of 400 samples (4 µs).

Using the ADC with the miniDAX/miniProcess software bundle, the SPE spectrum has been created by histogramming the area of the first pulse after the trigger for every event. The pulse area is measured as the integral of the waveform in ADC counts over time. Because the full range of the ADC board is 2.25 V with a resolution of 14 bit, the area (in integrated ADC counts) corresponds to the number of signal electrons as follows:

$$1 \text{ integrated ADC count} = 10 \text{ ns} \cdot \frac{2.25 \text{ V}}{2^{14}} \frac{1}{R} \approx 171428 \text{ signal electrons}, \tag{6.4}$$

assuming 50 Ω signal line impedance. Usually 50 000 waveforms have been used for each

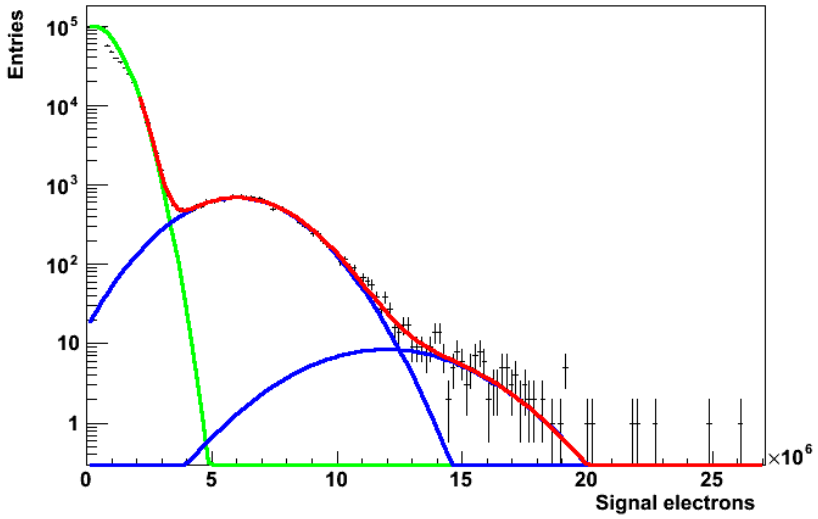

Figure 6.21: Fitted SPE spectrum. The first peak (green) is the noise peak, the other two peaks (blue) are the signal peak from single and double photoelectrons, respectively.

measurement.

A typical SPE spectrum can be found in Fig. 6.21. The first peak corresponds to electronic noise and comes from the waveforms in which no SPE signal was found. The second peak represents the SPE signal. The gain of the PMT corresponds to the mean of this peak (in signal electrons), as it is the mean number of electrons measured in the signal for each incoming photoelectron. A third, smaller peak can also be seen. It comes from the fraction of events in which two photoelectrons have been detected at almost the same time.

The spectrum is fitted with three Gaussian functions in the following way:

$$f(x) = A_n \cdot e^{-0.5(\frac{x-\mu_n}{\sigma_n})^2} + A_1 \cdot e^{-0.5(\frac{x-\mu_1}{\sigma_1})^2} + A_2 \cdot e^{-0.5(\frac{x-2\cdot\mu_1}{\sqrt{2}\cdot\sigma_1})^2} \tag{6.5}$$

where A_n, A_1 and A_2 are the amplitudes of the noise peak, the single photoelectron and the double photoelectron peak, respectively, μ_n is the mean and σ_n the resolution of the noise peak and μ_1 the mean and σ_1 the resolution of the SPE peak. The mean of the double photoelectron peak is fixed to be twice the SPE peak's mean, and the resolution of the double photoelectron peak is fixed to be the one of the SPE peak multiplied by $\sqrt{2}$. From the Hamamatsu data sheet the gain of the R11410 is supposed to be $G = 5 \cdot 10^6$

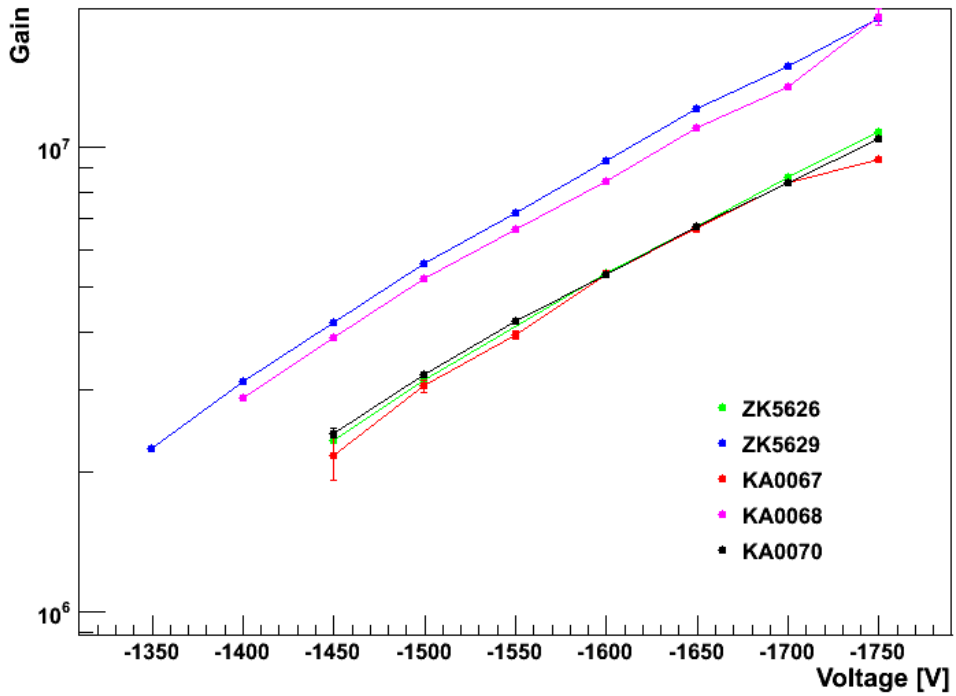

Figure 6.22: Gain vs HV for the five R11410-10 PMTs at different supply voltages, measured at room temperature in the black box.

with $U = -1500$ V supply voltage. Some variation around this gain was found in the black box measurements for the different PMTs. As expected (see Section 4.2.1) the gain rises exponentially with increasing voltage (see Fig. 6.22). The maximum allowed voltage is $U_{max} = -1750$ V. When the voltage is too low, the SPE peak can not be distinguished properly from the noise peak anymore, and the fit fails. This lower boundary to the voltage range varies a bit from PMT to PMT but is usually somewhere around $U = -1400$ V. The SPE resolution of the PMT is defined as

$$res_{SPE} = \frac{\sigma_1}{\mu_1} \tag{6.6}$$

It does not depend on the PMT supply voltage and has been found to be similar for all PMTs at $\sim 40\%$ (see Fig. 6.23).

The peak-to-valley ratio is the ratio of the amplitude of the signal peak in the SPE spectrum to the lowest point between noise and signal peak. Since the fit can sometimes

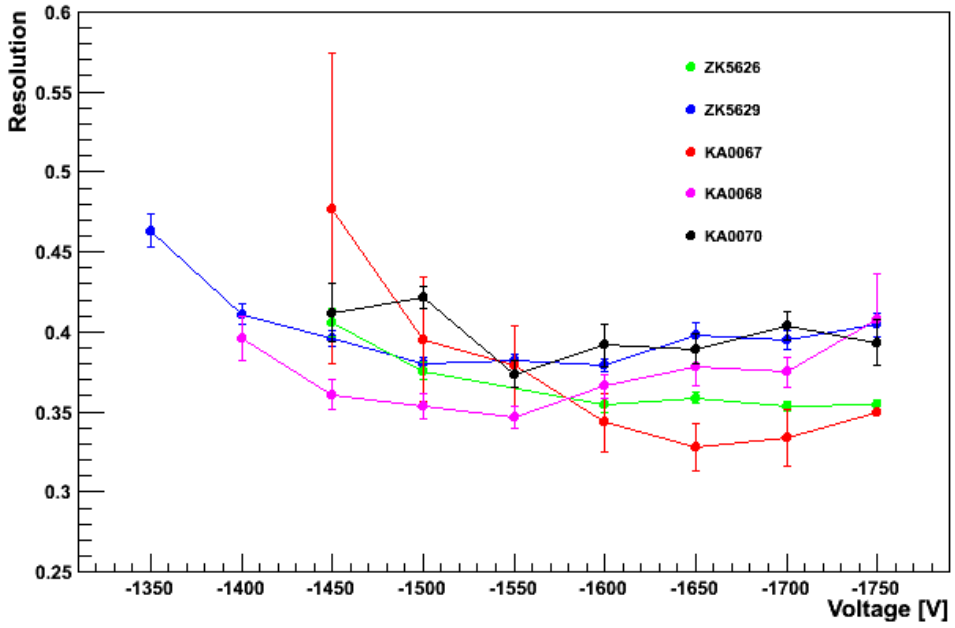

Figure 6.23: Resolution vs HV for the five R11410-10 PMTs at different supply voltages, measured at room temperature in the black box.

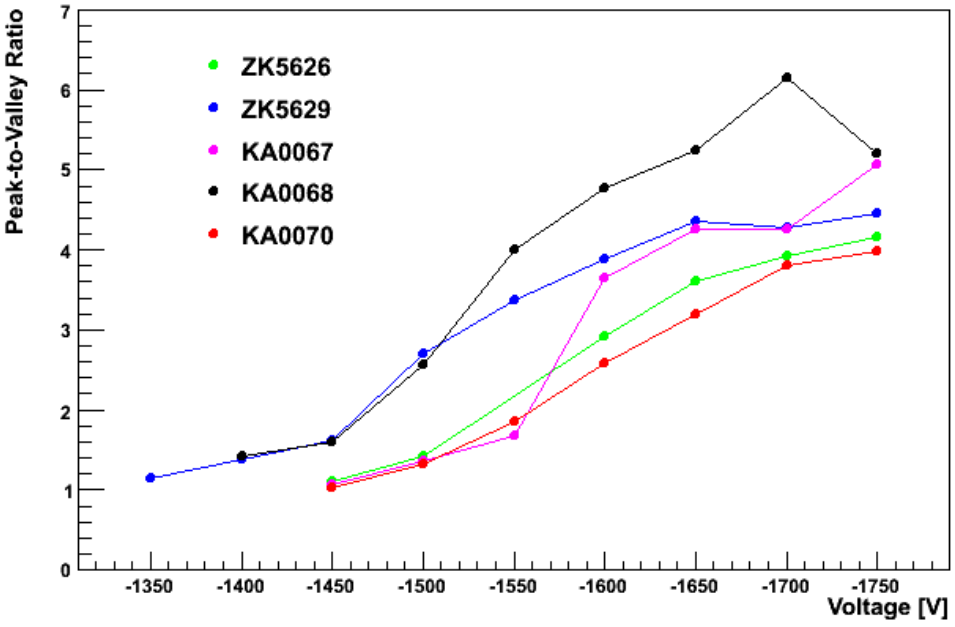

Figure 6.24: Peak-to-valley ratio vs HV for the five R11410-10 PMTs at different supply voltages, measured at room temperature in the black box.

underestimate the valley, the ratio is determined from the actual data. For this purpose the histogram is rebinned to eliminate statistical fluctuations between neighbouring bins, thereby smearing the valley a bit, leading to a slight underestimate of the peak-to-valley ratio. The measured values of the peak-to-valley ratios are shown in Fig. 6.24 as a function of the applied voltage.

6.4.2 Performance in Liquid Xenon

Tests in liquid xenon are much more laborious than black box tests due to the pumping and cooling involved. It is however critical to ensure that the PMTs will work without problems in this environment before implementing them in the XENON1T detector. The interest lies not only in the PMT's initial behaviour in liquid xenon, but also in its long-time stability and response to repeated cooling cycles.
In a first trial run of MarmotX the R11410 PMT ZK4998 was kept cold for one week. At this time the automatic nitrogen refilling system was not in place yet so that a manual refill was required every two hours. It was found that the gain of this PMT dropped significantly after the cool-down. However, the gain measured before at room temperature had been much higher than expected from the PMT's data sheet. Over the whole week the gain continued to decrease. After being warmed up to room temperature again the gain did not increase again.
Several reasons might exist for this unexpected behaviour: First, as the gain measured afterwards was much closer to the nominal gain, and the PMT had not been used much before, it might be that it just went through an initial aging process [85] [93]. On the other hand due to the manual refilling of the liquid nitrogen the temperature and pressure were not kept very stable, but showed fluctuations of $\sim 8\%$. On the second day in liquid xenon the xenon inside MarmotX got even frozen by the accidental refill of too much nitrogen which came to touch the Dewar vessel containing the xenon with the PMT, resulting in the PMT's tripping. It took two days until the PMT could be restarted. Although the device seemed to work fine afterwards it is quite possible that this event had a lasting effect on it.
The experiment has therefore been repeated with a new PMT, the R11410-10 ZK5626. The PMT was constantly running at – 1600 V. An automatic calibration system has been used to take an SPE spectrum every four hours. For this reason the LED had to be

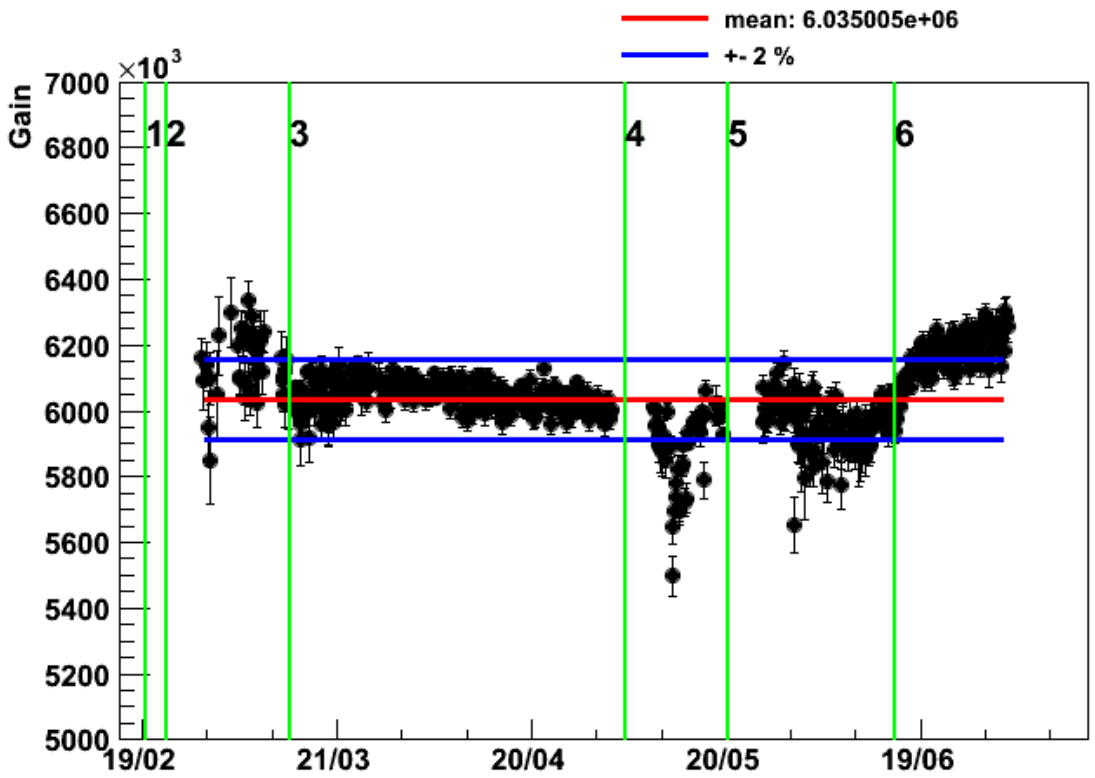

Figure 6.25: Gain evolution of the R11410-10 PMT ZK5626 in liquid xenon. Several incidents are marked: 1: Start of cooling. 2: Accidentally too high LED illumination. 3: Again accidentally too high LED illumination. 4: LED switched off. 5: Failure of the PMT power supply. 6: Accidentally too much nitrogen refilled.

running at the single-photon level used for SPE measurements constantly, including the time between the measurements.

The gain evolution of this test can be found in Fig. 6.25. Cool-down started at February 20$^{\text{th}}$ (marked 1 in Fig. 6.25). Regular gain measurements using the ADC with miniDAX did however take place only from February 29$^{\text{th}}$. Initially a decrease in gain was observed for this PMT as well, but on a much lower level. This PMT had shown a much lower gain from the beginning also at room temperature. After a few weeks the PMT gain appeared however to be very stable. The blue lines in Fig. 6.25 mark the region of $\pm$ 2% around the mean gain of the whole measurement. There are however some spikes apparent in the evolution plot. All of them can be linked to external events influencing the stability of

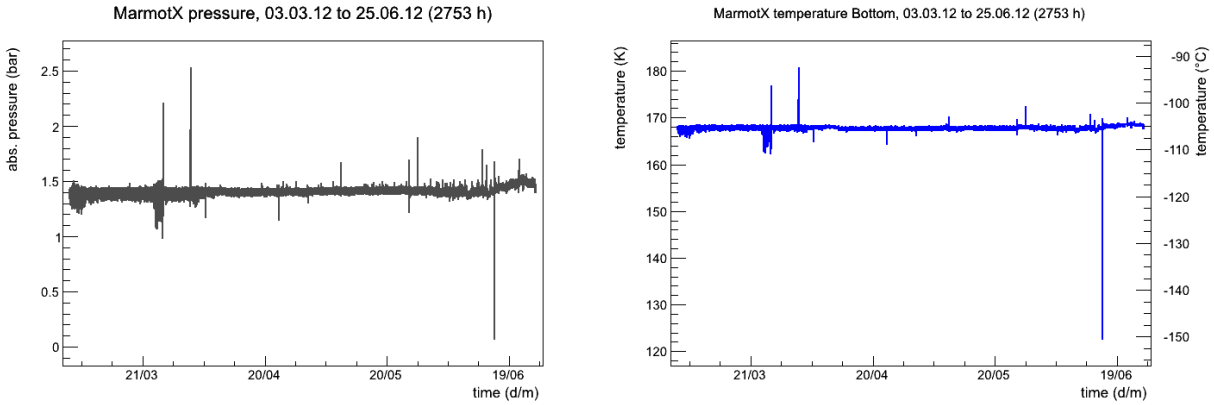

Figure 6.26: Stability of pressure (left) and temperature (right) in MarmotX.

the set-up:

The colder temperatures in liquid xenon affect not only the PMT but also the LED that is used to create single photons. To account for the decreasing amount of light emission the voltage of the LED has to be adjusted. Doing this the voltage was accidentally increased too much on February 23$^{\text{th}}$ (marked 2 in the plot) - from 1.0 V that had been used at room temperature to 2 V, while 1.23 V would have been the correct setting. The PMT reacted to this high illumination with a steep increase in the dark count rate which in turn influenced the SPE spectra in a way that the gain appears to be lower than before. The PMT recovered over the course of one week.

A similar accident occured on March 13$^{\text{th}}$ (marked 3). After borrowing the pulse generator to another experiment the signal and trigger cables were swapped upon reinstallation, leading to a TTL signal being fed to the LED. The mistake was only realised in the next morning. The PMT reacted again with very high dark current, leading to lower gain values being calculated. Again it took one week for full recovery.

While the automatic nitrogen refill system kept the conditions in MarmotX very stable occasional manual refills were still necessary when the nitrogen storage Dewar vessel ran empty. In one of these cases on June 15$^{\text{th}}$ (marked 6) too much nitrogen was filled. While not causing the xenon to freeze the pressure dropped and the PMT tripped. Pressure and temperature returned to a new stable, but slightly different value as can be seen in Fig. 6.26. When the PMT was switched on again it now also showed a higher gain value than before.

Cooling the PMT to liquid xenon temperature puts some stress on this device, and in

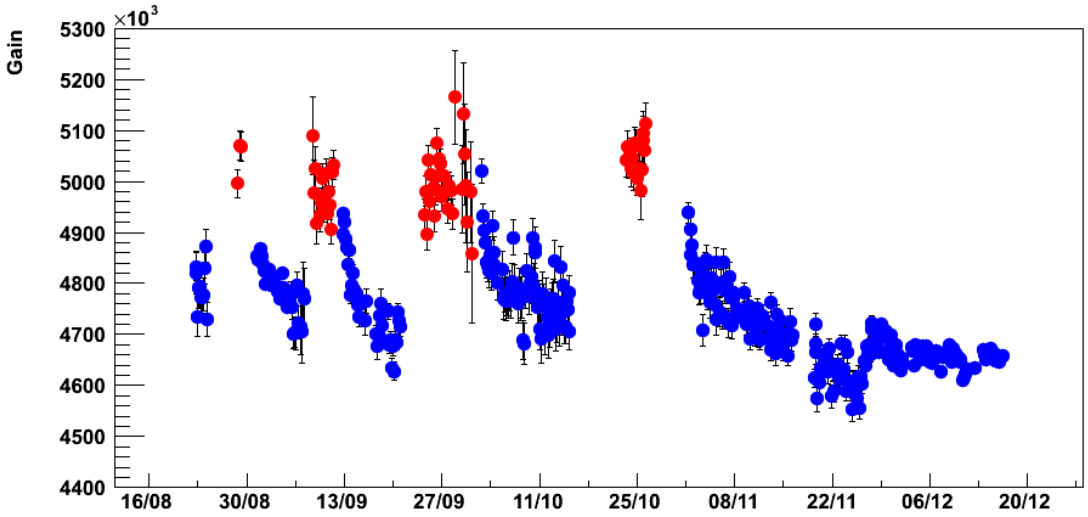

Figure 6.27: Gain evolution of the R11410-10 PMT KA0067 over five cooling cycles. Blue points have been measured with the PMT immersed in liquid xenon, red points without cooling.

XENON100 it was found to be the main reason for PMTs failing. A third PMT (the R11410-10 KA0067) has therefore been tested in MarmotX, this time going through several cooling cycles. The PMT was tested with a supply voltage of – 1600 V over four months in which it was cooled down five times. Again the gain was measured automatically with blue LED light every four hours. Each time that MarmotX was filled with liquid xenon the gain value decreased for several weeks before reaching a stable cold value (Fig. 6.27). When warmed up the gain always recovered to the gain it had before. The warm gain and the cold gain were very stable.

6.4.3 Dark Counts

With each gain calibration during the cooling cycle test the dark count rate has also been determined by counting all signals in the first microsecond of each waveform, which is recorded before the start of the LED pulse. These signals should therefore not stem from LED light, but from dark counts. However, given that the PMT is immersed in liquid xenon there is still a fraction of the pulses originating in scintillation signals. Furthermore

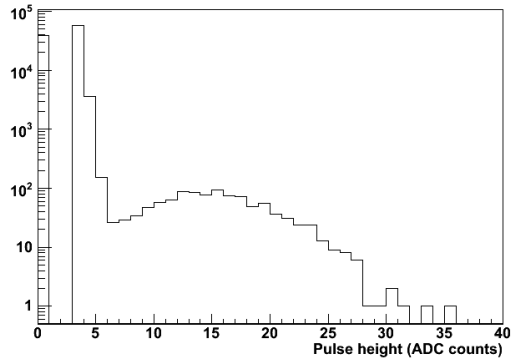

Figure 6.28: SPE pulse height spectrum from LED measurement in liquid xenon.

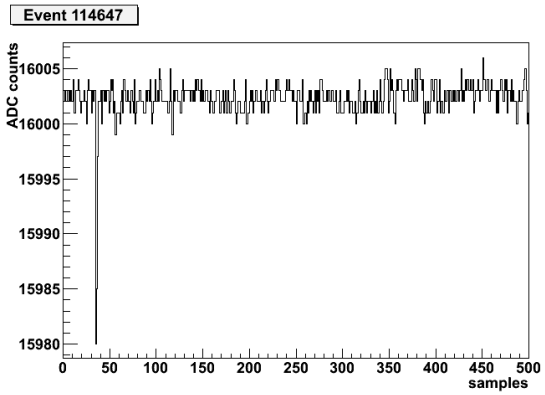

Figure 6.29: Typical SPE signal from dark counts.

electric noise can also contribute to the total signal rate. The dark count spectrum looks similar to an LED SPE spectrum with noise and signal peak. To avoid including electric noise into the dark count measurement the signal threshold has been raised to the mean pulse height of single photoelectron pulses as determined from the gain measurement (Fig. 6.28). Assuming that the pulse height spectrum is symmetric around this point the resulting number of signals found above this threshold should be half of the total number of dark counts. It was found that two additional cuts are needed in order to exclude scintillation signals from the dark count measurement. In order to avoid signals that are clearly too big to come from dark counts, as in Fig. 6.30, the pulse height must be less than twice the average SPE pulse height. And the total number of signals within a waveform has been limited to five, avoiding clusters of SPE-like signals as can be seen in Fig. 6.31, that are very unlikely to stem from dark counts. The resulting dark count rate determined in this way can be found in Fig. 6.32. The rate is clearly dependent on the temperature, with an average rate of 150 Hz in cold and 600 Hz in warm. While the dark count measurements have been taken in between of the LED pulses, the rates found here are considerably higher than measurements taken after the LED has been completely off for an hour. It appears that the illumination of the photocathode increases the chances of an electron to be released even some time afterwards. This is in agreement with what has been observed in the accidentally too high illumination during the long term stability test described in Section 6.4.2.

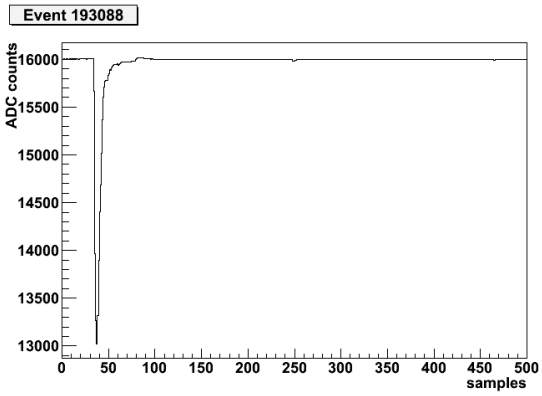

Figure 6.30: Probably a xenon scintillation signal, too big to stem from dark counts.

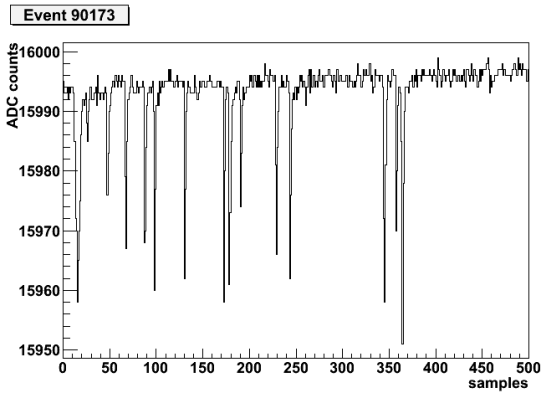

Figure 6.31: Cluster of SPE-like signals, unlikely to stem from dark counts.

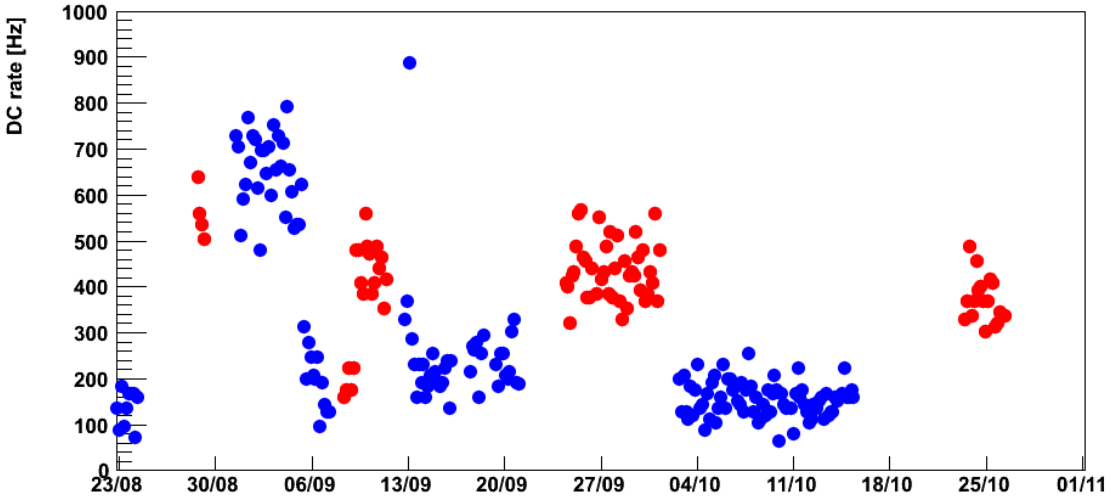

Figure 6.32: Dark current evolution of the R11410-10 PMT KA0067 over five cooling cycles. Blue points have been measured with the PMT immersed in liquid xenon, red points without cooling.

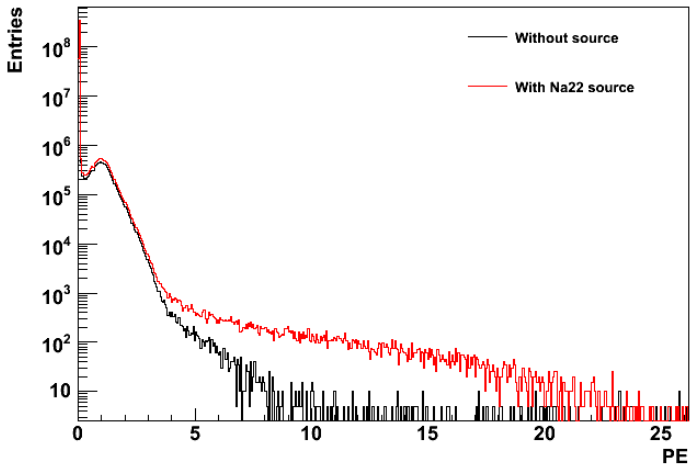

Figure 6.33: Effect of a ^{22}Na source on the SPE spectrum from dark counts in a R9869 PMT (not the R11410) that is used in the Xurich detector. The source induces larger signals found mostly in the tail of the SPE spectrum.

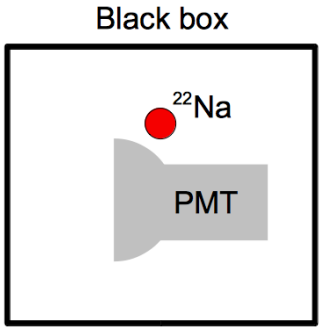

Figure 6.34: The ^{22}Na source has been placed on the side of the PMT for this test.

6.4.4 Effect of the Presence of Radioactive Sources

For some PMTs radioactive sources like those used in calibration have been shown to create signals directly in the PMT (for example in the Hamamatsu R9869 PMTs used in the Xurich detector, see Fig. 6.33). To test if this is the case for the R11410 three LED single photoelectron spectra have been taken in the black box, one normal spectrum, one with a ^{22}Na source attached to the side of the PMT body (Fig. 6.34) and one with the ^{22}Na source directly in front of the PMT window. After positioning the source, which exposed the PMT (without having voltage applied) to room light for a few seconds it was waited for half an hour before taking the next measurement. The measurements showed no qualitative difference between the SPE spectra with and without source (figs. 6.35 and 6.36). Using calibration sources close to the PMTs should therefore not be a problem in XENON1T.

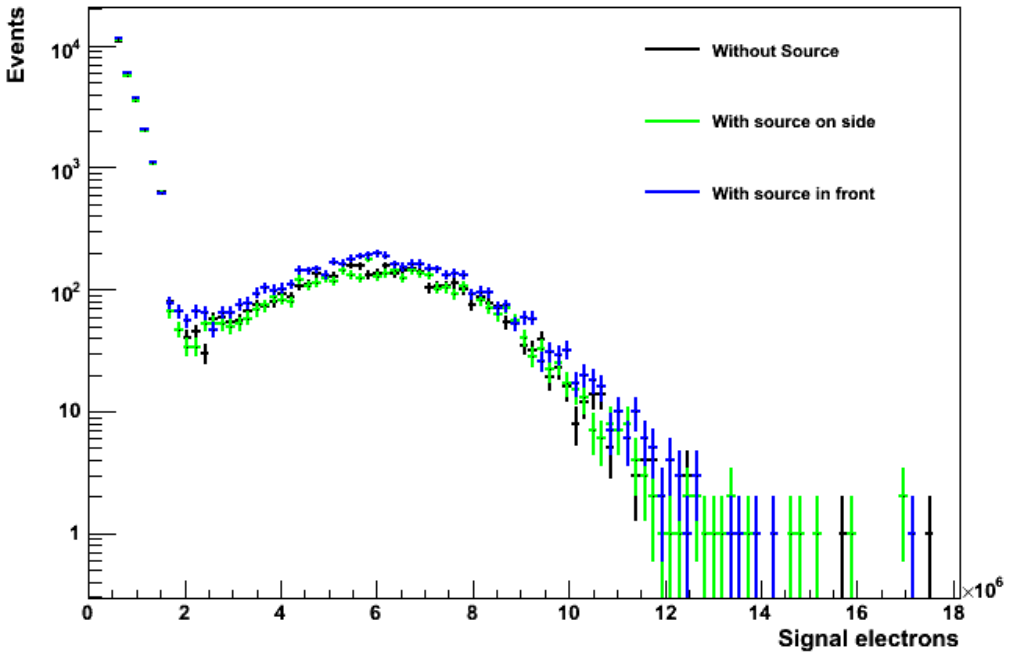

Figure 6.35: LED SPE spectra of the R11410 PMT with and without a ^{22}Na source present at the side of the PMT body or in front of the window.

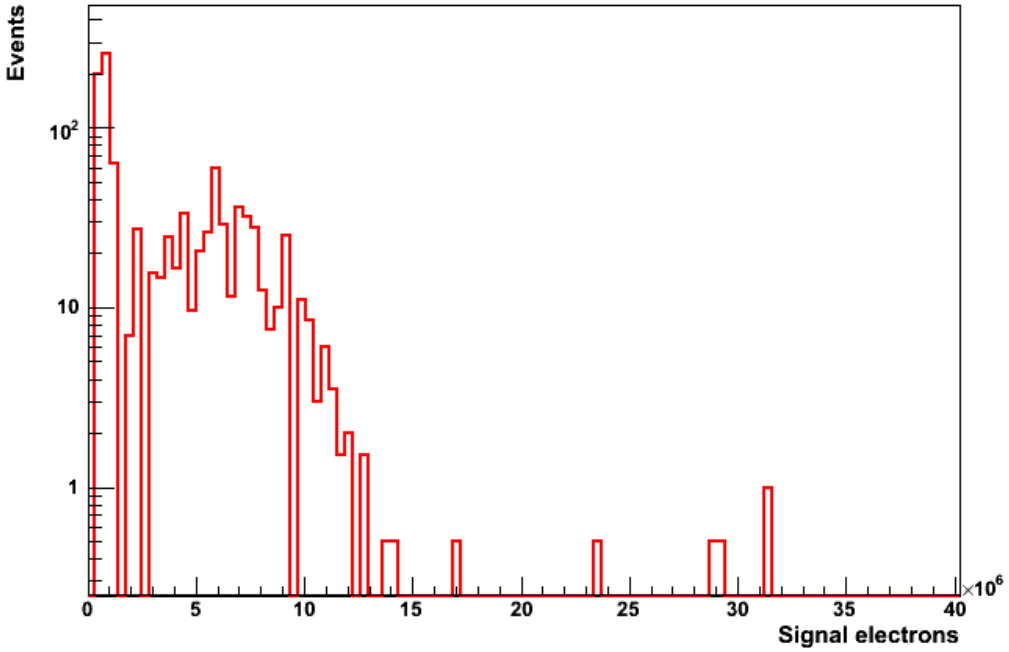

Figure 6.36: Difference between the SPE spectrum with and without a ^{22}Na source in front of the PMT window. A small overall increase in events is observed, but no qualitative change is seen.

6.4.5 Performance in Electric Fields and High Pressure

In XENON1T the PMTs will be placed very close to each other in order to maximise the light collection efficiency. It is planned to keep a centre-to-centre distance of 80 mm, thus leaving only 2.5 mm between the edges of the PMTs. When the PMTs are supplied with negative high voltage not only the photocathodes but also the metal bodies of the PMTs will be set to a negative potential of around – 1500 V. The exact voltage will however vary between the different PMTs, as it allows to equalise the gain. In some cases it may also be necessary to switch off individual PMTs that fail. It is therefore necessary to test the planned set-up to ensure that the electric fields between the PMTs do not influence the behaviour. Furthermore the PMTs could also be affected by the strong fields inside the TPC, although it is possible to counter these with a protecting mesh between the TPC electrodes and the PMTs.
Three PMTs have been tested inside MarmotXL at the prefered centre-to-centre distance of 80 mm in various combinations of voltages supplied to the three PMTs, mimicking the possible situations in a running detector setting:

PMT 1	PMT 2	PMT 3	Plate
– 1600 V	– 1600 V	– 1600 V	0 V
– 1750 V	– 1600 V	– 1500 V	0 V
0 V	– 1750 V	– 1750 V	0 V
– 1750 V	– 1750 V	0 V	0 V
0 V	– 1750 V	– 1750 V	– 1500 V
– 1750 V	– 1750 V	0 V	– 1500 V

All tests have been performed in room-temperature gaseous xenon. The metal plate has been kept in a distance of ∼15 mm from the PMTs' photocathodes. For every combination an LED SPE spectrum has been taken from each PMT and has then been compared to the LED SPE spectrum at the same voltage of this PMT with no HV on the other PMTs or the metal plate (Fig. 6.37). In all these cases no deviation has been found.
For an additional test the field between photocathode and plate has been varied by applying different voltages to the metal plate. One PMT was kept at – 1500 V while the other two PMTs were switched off. The distance between the PMTs and the metal plate was reduced to 3 mm. Again the test was conducted in room-temperature gaseous xenon

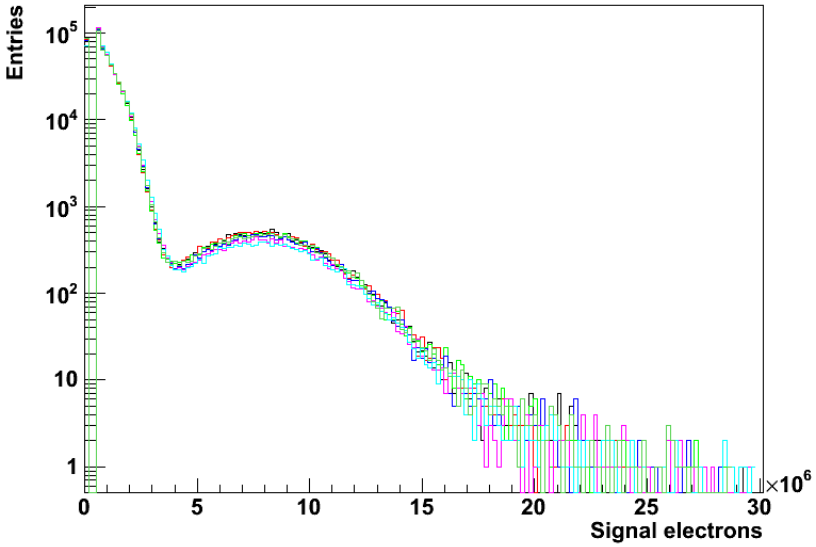

Figure 6.37: Comparison of LED SPE spectra of PMT 2 at -1600 V in different electric fields.

with the following configurations:

PMT	Plate	Resulting Field
– 1500 V	– 1500 V	0 kV/cm
– 1500 V	0 V	5 kV/cm
– 1500 V	+ 750 V	7.5 kV/cm
– 1500 V	+ 1500 V	10 kV/cm
– 1500 V	+ 1800 V	11 kV/cm

Up to 11 kV/cm no irregularities have been observed. At higher fields sparking occurred, most likely between the metal plate and ground. The PMT did not trip but saw some light signals.
Finally a quick test has been done with the pressure of the xenon gas increased to 2.5 bar. For this test the recirculation has been stopped. Again no problems have been found.

Chapter 7

The Voltage Divider Base for the Hamamatsu R11410 PMT

While the PMT itself has to be carefully selected to match the requirements of the experiment, much of its performance also depends on how the voltage is distributed to it and how the signal is read out. Attention has therefore been given to the design of the voltage divider base that will be used together with the R11410 PMT in the XENON1T detector.

In particular the base design and the applied voltage affect the gain of the PMT and its linearity. Especially PMT saturation at high energy signals, which was a problem in XENON100 (see Section 3.3.3), should be avoided in XENON1T. As the gain of the R11410 is generally higher than that of the R8520 used in XENON100, and the area of its photocathode is larger, this aspect of the base design becomes even more important. The optimisation of the base in terms of linearity is described in the following section.

Another major design goal of the base, as for every other part of the XENON1T detector, is to keep the radioactive background to a minimum. Of course all used parts need also to be suitable for the use in liquid xenon. The material selection is described in Section 7.3.

7.1 Linearity

7.1.1 External Factors Contributing to the Linearity

As it has been explained in Section 4.2.5, there can be some divergence between the linearity of individual PMTs, depending on the photocathode and the positioning of the dynodes. But the observed linearity can also depend on external factors, especially in the way the voltage is supplied. In XENON1T these external factors play the dominating role for the overall linearity due to the specific limitations set on the voltage divider bases and the read-out electronics by the experimental requirements.
One important point is that the last dynodes can be depleted if pulses become too large, leading to saturation of the output signal [84]. For individual larger pulses this effect can be countervailed by the use of decoupling capacitors connected to the last dynode stages [83] [84] [85].
Using capacitors does however not increase the linearity if the signal repetition rate is too high, as the recharging time of the capacitors also increases with the capacitance. For good linearity at higher repetition rates it is therefore also necessary to reduce the resistance of the base [83] [84] .
When the signal current exceeds a certain fraction of the base current it affects the electric fields within the PMT, thus leading to changes in gain and ultimately saturation [83] [84]. It is possible that saturation is preceeded by overlinearity where space charge effects lead to better focusing onto the dynodes [85]. This can be countervailed by reducing the base's total resistance in order to increase the base current, using voltage stabilising elements such as transistors or Zener diodes, or even connecting each dynode stage to its individual high voltage power supply [83] [84] [85] [93].
Apart from the PMT itself and its base the read-out of the signals can also influence the linearity. An amplifier may be used which can allow to lower the bias voltage of the PMT: this reduces the gain of the PMT and thus the total signal current, which in turn expands the range over which the PMT is linear. The output signal is then amplified to compensate for the lowered resolution when reading out smaller signals.
Finally, if using an ADC for digitising the output of the PMT, saturation can also occur if the size of the output signals exceed the total input voltage range of the ADC.

7.1.2 Linearity Requirements for the PMTs in XENON1T

In XENON100 PMTs start saturating at light pulses of 6000 – 8000 photoelectrons [96], corresponding to signals of about ∼150 keV. The goal in XENON1T is to vastly improve on this number, aiming on good linearity up to signals corresponding to an energy of at least 1 MeV. As the light pulses are spread over several PMTs, it is necessary to estimate the maximum number of photoelectrons that an individual PMT will see in such a signal. This calculation has originally been performed by T. Marrodan: Assuming the same charge yield of ∼350 PE/keV as observed in XENON100 [97], a 1 MeV event will produce $3.5 \cdot 10^5$ PE. While the photocathode area of the R11410 PMT is 6.8 times as large as that of the R8520, the distance from the PMT to the liquid level will also increase from 1.75 cm in XENON100 to 6 cm in XENON1T [97], effectively increasing the solid angle from 15% in XENON100 to 16.8% in XENON1T [97]. In order to reach the goal of good linearity up to 1 MeV signals in XENON1T each PMT must therefore be linear up to signals of $\sim 6 \cdot 10^4$ PE.

The linearity does however depend not only on the size of the individual light signals, but also on the signal repetition rate. While this rate will be very low during dark matter measurements, it will increase substantially during calibrations. Even if each light pulse individually would not cause the PMT to saturate, the average signal current of the PMT needs to be small compared to the base current in order to sustain good linearity. The average signal current should not exceed 5% of the base current [84], for good linearity it is recommended that it should be below 1% [84].

It is expected that the signal rate for each individual PMT during energy calibration measurements will be ∼300 Hz. If a PMT were to observe the maximum of a 1 MeV signal at a signal rate of 300 Hz, this would, assuming a gain of $5 \cdot 10^6$, correspond to a signal current of ~ 14 μA. In order to provide good linearity at this rate, the base current would need to be at least 280 μA.

Increasing the base current is however problematic in the XENON1T experiment because it also increases the heat produced by the base. This puts some strain on the cooling of the detector and could in the worst case lead to bubbles in the liquid xenon. For the total of 248 PMTs the maximum allowed power dissipation is 10 W. The resistance of the base has therefore to be carefully balanced between low heat and good linearity.

Another way to support the linearity at such high signal rates would be the use of voltage

stabilising elements such as Zener diodes or transistors in the base circuit [83] [84] [85] [93]. However, as the radioactivity of the base needs to be kept to a minimum in order not to introduce background into the dark matter search, the amount of material and the range of electronic elements that can be used is limited. This strongly discourages the use of diodes or transistors.

A third possibility would be to decrease the PMT's bias voltage. As the gain increases exponentially (see Section 4.2.1) and the base current increases linearly with the voltage, reducing the bias voltage leads to an improved signal to base current ratio and therefore better linearity. To avoid losing resolution of signals of a few photoelectrons an amplifier can be used for the PMT output. However, because the amplifiers that were used in the XENON100 experiment introduced additional electronic noise into the signal, it was planned to avoid using amplifiers in XENON1T. Yet, at the time of writing of this thesis, it is now probable that amplifiers with a fixed gain of 10 will be used, though not in order to enable reducing of the PMTs' bias voltage to improve the linearity, but in order to increase the gain further, to improve the single photoelectron resolution with the ADC even more.

If this is the way it will be done, the observed linearity will no longer be limited by the PMT or by its base, but by the ADC itself. The CAEN V1724 ADC boards that will be used in XENON1T have an input voltage range of 2.25 V with a resolution of 14 bit and an input impedance of 50 Ω. The baseline will be set to $U_{max} = 2.2$ V. So, depending on the gain G of the PMT, the maximum number of photoelectrons S_{max} that can be contained in a $t = 1$ µs long light pulse without saturating the ADC will be

$$S_{max} = \frac{I_{max} \cdot t}{G \cdot a \cdot e} \tag{7.1}$$

$$= \frac{U_{max} \cdot t}{G \cdot a \cdot e \cdot R} \tag{7.2}$$

$$\approx \frac{2.2\ \text{V} \cdot 1\ \mu\text{s}}{G \cdot 10 \cdot 1.602 \cdot 10^{-19}\text{C} \cdot 50\Omega} \tag{7.3}$$

$$\approx \frac{2.7 \cdot 10^{10}}{G}, \tag{7.4}$$

where a=10 is the amplification factor of the amplifier and $e \approx 1.602 \cdot 10^{-19}$ C is the electron charge. For the nominal PMT gain of $G = 5 \cdot 10^6$, ADC saturation for 1 µs long signals would start already at $S_{max} \approx 5500$ PE, corresponding to an S2 signal of only 100 keV.

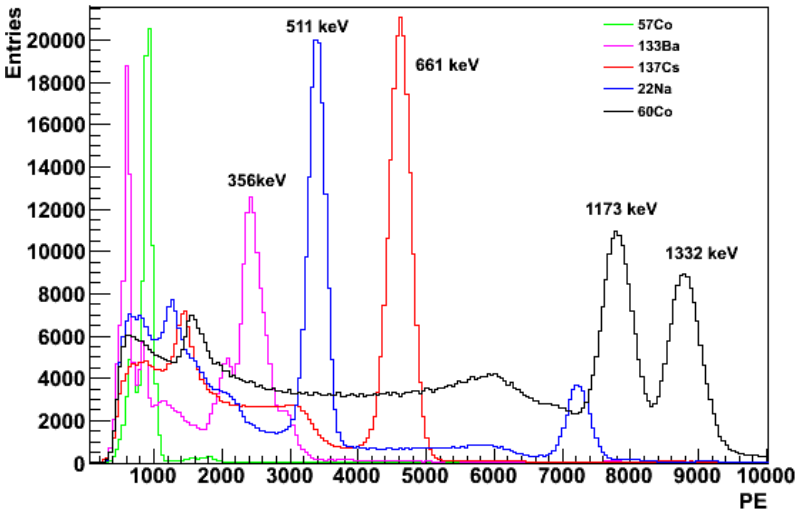

Figure 7.1: Peak positions of different sources with NaI crystal, measured with the R11410-MOD PMT ZK5629 at a bias voltage of –1300 V.

It has not been decided yet whether this configuration will be used. In order to allow comparison of the linearity of different base designs independently from the chosen PMT gain, the signal size is not measured in photoelectrons, but as the maximum signal current I_{max}. The number of photoelectrons in a square pulse of length t can then be calculated from the maximum signal current depending on the PMT gain and the amplifier gain using Equation 7.1.

7.1.3 Testing Linearity

An ideal test of the PMT's linearity would result in a clear correlation between the number of photons hitting the photocathode and the size of the resulting signal. While the determination of the latter number poses no problems, a direct measurement of the first is not possible without involving the very same device that should be calibrated. One has therefore to resort to other methods for estimating the number of incoming photons.

For first tests the PMT has been optically coupled to a NaI scintillator. Using various radioactive sources this method mimics the way PMT saturation can be seen in the

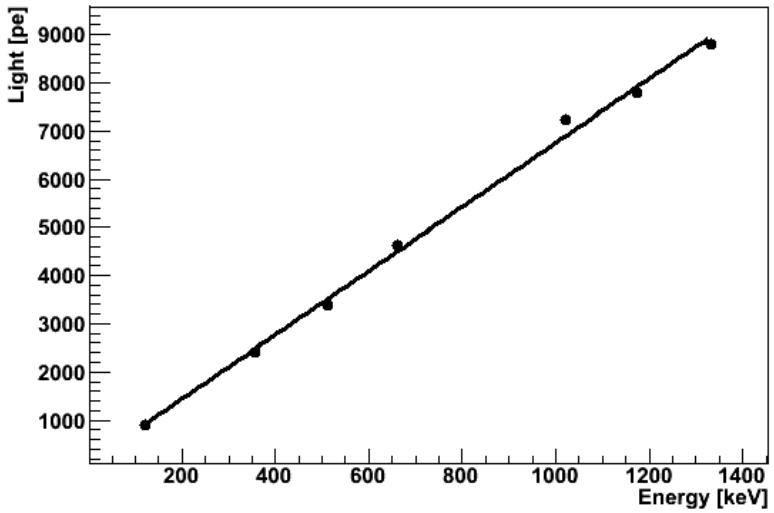

Figure 7.2: Photoelectrons from scintillation signals against peak energy. The base shows good linearity up to at least 9000 photoelectrons.

XENON100 detector: Assuming a constant light yield in the scintillator, the observed signals in the PMT should be proportional to the source energy up to the saturation point of the PMT. The number of initial photoelectrons can then be calculated using the gain as determined from an SPE spectrum (see Section 6.4.1).
This test was performed using ^{57}Co, ^{133}Ba, ^{137}Cs, ^{22}Na and ^{60}Co sources and lead to an improvement of the base by adding a fourth capacitor resulting in linear behaviour up to at least 9000 photoelectrons at the nominal supply voltage of – 1500 V (see Figs. 7.1 and 7.2). This exceeds already the linearity that was reached in XENON100, where the PMTs are linear up to 6000 - 8000 photoelectrons [96].
But in order to not only reach, but also to improve on the linearity of XENON100, it is necessary to measure even larger light signals, the goal being linearity up to at least $\sim 6 \cdot 10^4$ PE (see Section 7.1.2). Clearly light signals of this large size can not be created using the small NaI scintillator with radioactive sources.
For tests at larger signals a laser has been used together with an LED similar to the method described in [98]. The laser can provide several ten thousands of photons at once. The size of light pulses is varied by changing the laser's supply voltage. But the exact amount of photons in each pulse is not known other than from the measurement by the

PMT itself. For this reason the additional LED is necessary in order to conduct a linearity test. The idea is to measure up to which point the PMT is able to respond linearly to a small deviation (an additional LED pulse) on a large signal (the laser pulse). For this the LED settings stay the same throughout the whole measurement, while the size of the laser pulses is varied. For each point of the linearity curve three separate measurements have do be done: The laser pulse by itself, the LED pulse by itself, and then both at the same time. As long as the PMT is linear the differential linearity, defined as

$$Lin_{diff}(P_{laser}) = \frac{S(P_{both}) - S(P_{laser})}{S(P_{LED})}, \tag{7.5}$$

where $S(P_{laser})$ is the mean area of the PMT signals for the laser pulses, $S(P_{LED})$ the mean area of the PMT signals for the LED pulses and $S(P_{both})$ the mean area of the PMT signals for laser and LED flashing at the same time, should equal 1. If the PMT starts to saturate, the additional LED pulse on top of the laser signal would not result any more in an increase of the signal as big as the actual change in the total incoming light, and thus Lin_{diff} would become a value < 1. If on the other hand the PMT exhibits overlinearity, the output signal would increase overproportionally with the addition of the LED pulse and Lin_{diff} would be > 1.

For each setting of the laser voltage one can therefore say with certainty whether the PMT output is still linear. If it is, the number of photoelectrons produced by this pulse can then be determined using the previously measured gain of the PMT. This measurement allows therefore to determine up to which point the PMT is perfectly linear. For larger light signals only the general behaviour of the PMT can be derived from the measurements, without knowing the exact extend of over- or underlinearity in this region, as the number of photoelectrons can not be measured precisely with a non-linear PMT.
However, if the steps between the different measurement points are small enough, it is possible to get a more accurate estimate of the absolute linearity, or S(P)/P, via integration. The absolute linearity connects each light pulse P to the resulting PMT signal S(P). In the measurement described before it is:

$$S(P_{both}) = S(P_{laser}) + Lin_{diff}(P_{laser}) \cdot S(P_{LED}), \tag{7.6}$$

or, for sufficiently small LED pulses $P_{LED} = \epsilon \to 0$ and $P_{both} = P_{laser} + \epsilon = P + \epsilon$:

$$S(P + \epsilon) = S(P) + Lin_{diff}(P) \cdot S(\epsilon) \tag{7.7}$$

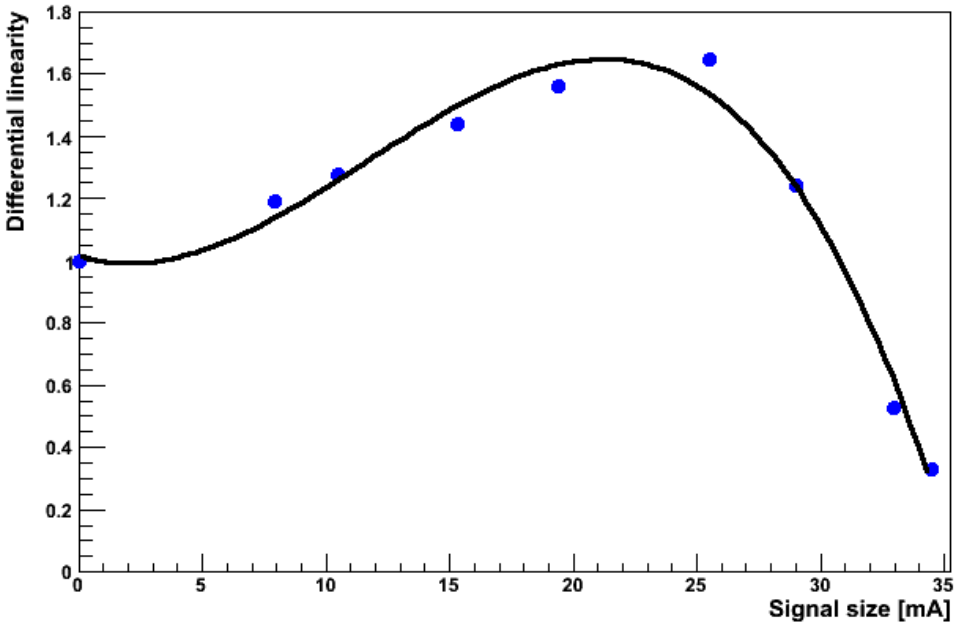

Figure 7.3: Example of a third order polynomial fit to a curve of differential linearity measurements.

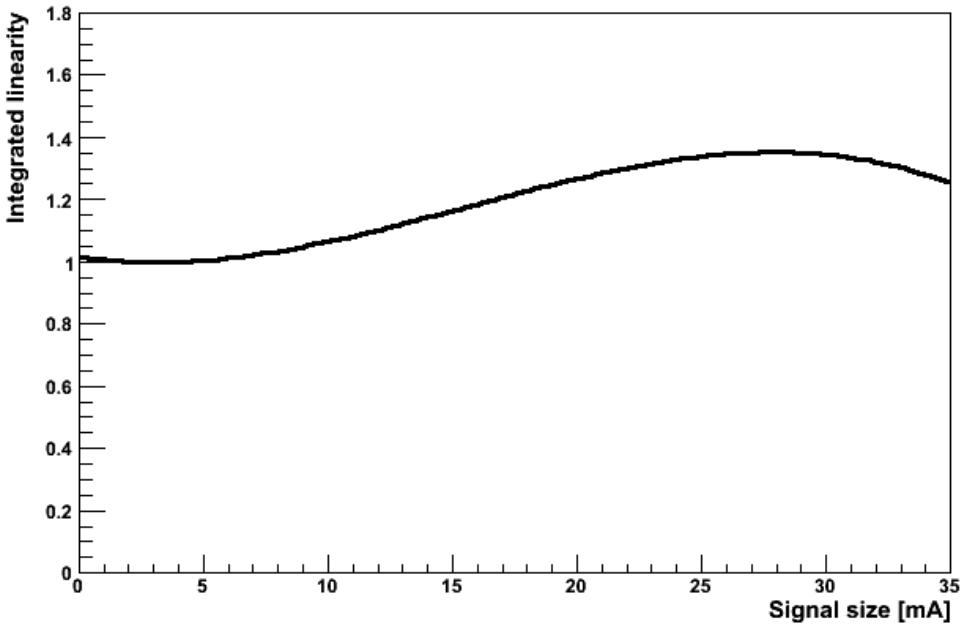

Figure 7.4: Integrated linearity derived from the differential linearity in Fig. 7.3.

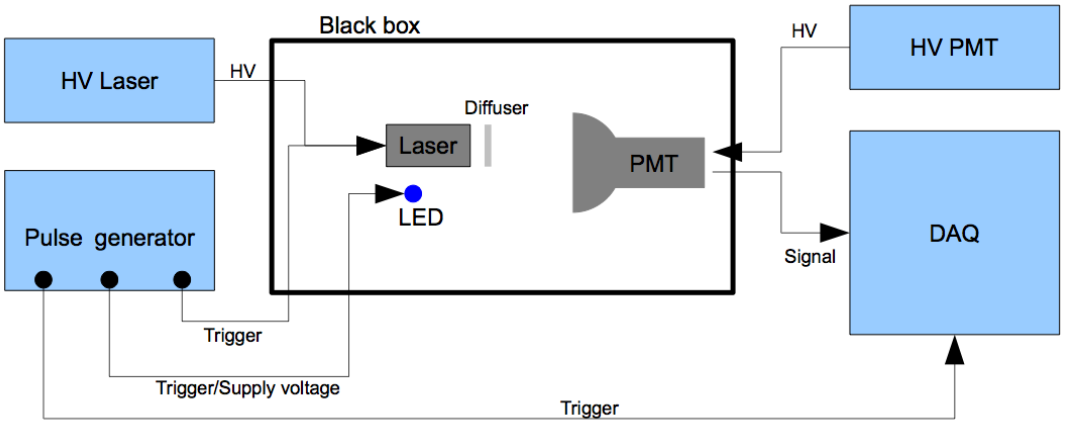

Figure 7.5: Set-up for a linearity measurement with laser and LED.

$$Lin_{diff}(P) = \frac{S(P+\epsilon) - S(P)}{S(\epsilon)} = \frac{dS}{dP} \tag{7.8}$$

$$S(P) = \int Lin_{diff}(P)dP \tag{7.9}$$

resulting in the absolute linearity

$$Lin_{abs}(P) = \frac{\int Lin_{diff}(P)dP}{P}. \tag{7.10}$$

In order to calculate this absolute linearity, Lin_{diff} must be known in functional form. To achieve this, the points of the linearity curve are fitted by a third order polynomial (Fig. 7.3). Using a polynomial to model $Lin_{diff}(P)$ allows for easy integration and division by P to derive the estimate of the absolute linearity (Fig. 7.4). All linearity tests have been conducted in a black box at room temperature. Laser, LED and DAQ have been triggered by the same BNC model 505 multichannel pulse generator. The length of the light pulses has been fixed to 1 µs. Measurements have been done with varying signal rates from 10 Hz to 1 kHz. Since the LED reacts about 0.2 µs slower to the pulse generator's signal than the laser, the trigger to the latter had to be delayed accordingly to ensure that the laser + LED signal is the actual sum of the two. This is furthermore ensured by not using a peak finding algorithm on the waveform recorded by the ADC but always integrating over the same region after the trigger from the pulse generator, corresponding to the position of the average laser signal.

The voltage of the LED has been supplied with the signal from the pulse generator which

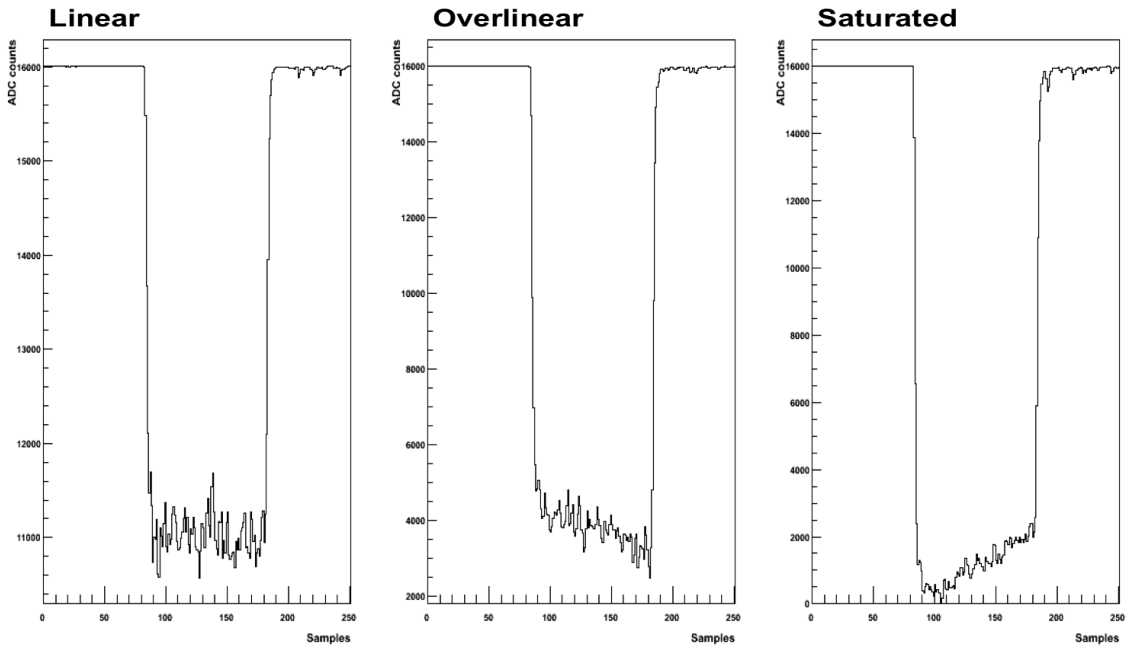

Figure 7.6: Typical waveforms in a linearity measurement from LED, laser and both at the same time.

has stayed unchanged throughout the measurement. It has been chosen high enough to result in a signal of several hundred photons in order to decrease the impact of statistical fluctuations. It has however been observed that the size of the LED signal can drift over time due to temperature changes. The LED signal has therefore been remeasured for each point of the linearity measurement.

The laser has been powered by an additional power supply and triggered from the pulse generator. Its voltage has been slightly increased for each point of the measurement, resulting in an accordant increase in its light output.

An example of the resulting waveforms is shown in Fig. 7.6. As long as the PMT is linear, the laser signal remains square shaped. Strong saturation can cause the signal to decrease already over the time of the signal, while strong overlinearity can lead to its growth (Fig. 7.7).

Several thousand events have been acquired with each setting. The signal area has then been integrated and the results filled into a histogram. The mean signal size for this

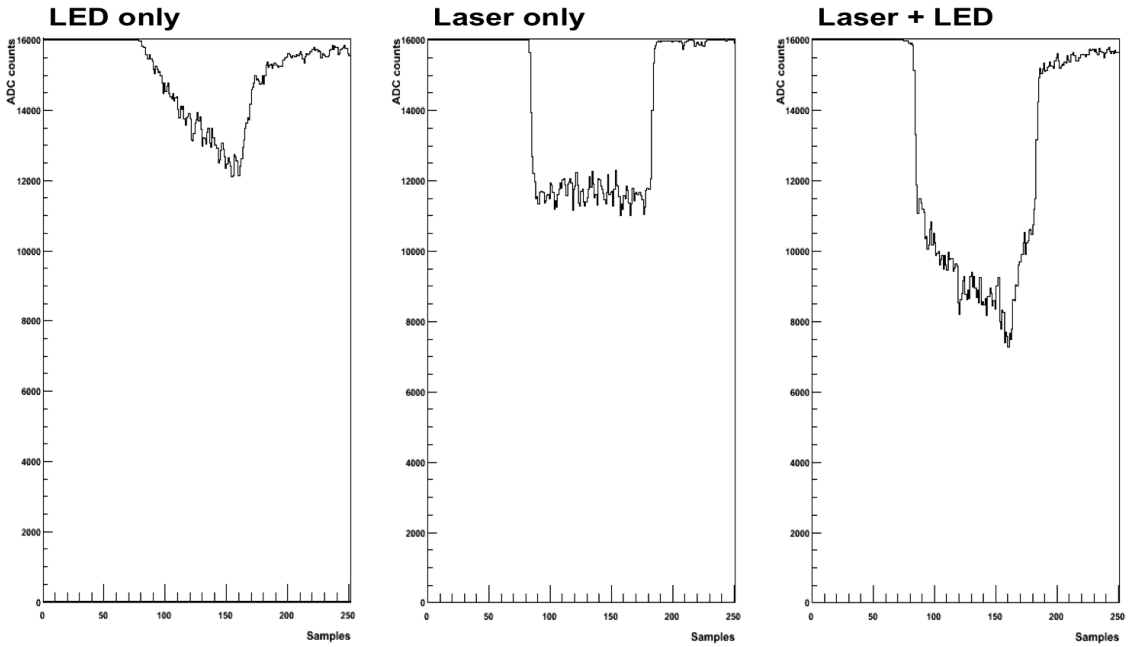

Figure 7.7: Waveform of a square shaped laser signal. As long as the PMT is linear the waveform stays square shaped (left). In case of overlinearity the signal appears to grow over time (centre). In case of saturation the signal appears to shrink over time (right).

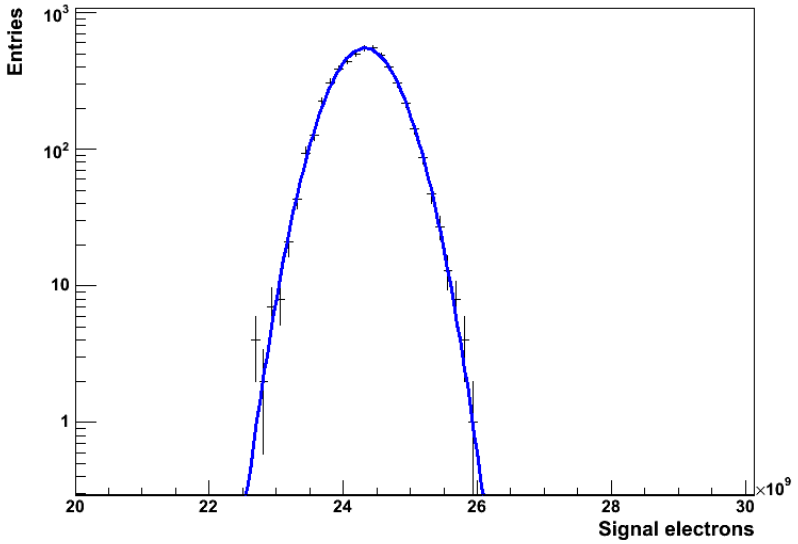

Figure 7.8: Example of the distribution of signal areas all taken with the same laser settings. The mean is determined by a fit with a Gaussian function (blue). In this example $\mu = (2.4 \cdot 10^{10} \pm 6.4 \cdot 10^{6})$ signal electrons.

setting has then been determined with a Gaussian fit (Fig. 7.8).

It should be mentioned that there exists a different method for measuring the linearity of a PMT that is employed both by Hamamatsu and the XENON group at UCLA. It uses two light sources of which one emmits light signals four times larger than the other. A rotating mask is then used together with an optical density filter to measure alternately the unfiltered big signal, the unfiltered small signal, the filtered big signal and the filtered small signal. As long as the PMT is linear the ratio between the signals of the two light sources should be constant for every filter. Linearity is then defined as

$$Lin_{frac} = \frac{S(P_4)}{S(P_1)} \cdot \frac{S(F(P_1))}{S(F(P_4))}, \tag{7.11}$$

where $S(P_4)$ is the mean area of the unfiltered big signal, $S(P_1)$ that of the unfiltered small signal, $S(F(P_4))$ that of the filtered big and $S(F(P_1))$ that of the filtered small signal. Cross-checks have been done between UCLA and UZH to compare the differences between the methods. It was found that the laser + LED method is much more sensitive to even tiny deviations from perfect linearity. This is the case because it investigates the linearity

of the addition of a very small light signal on top of a very big signal, compared to the linearity of a three times larger pulse on top of a relatively small one as done by the filters method. When the intensity of the light has just crossed the border to saturation, the effect on the whole signal will still be tiny, but it becomes visible with the method used here.

7.1.4 Optimisation of the Base Design in Terms of Linearity

The design of the base for the R11410 relies on the recommendations given by Hamamatsu for the voltage divider ratios for this PMT. The simplest design would thus consist of a chain of 14 resistors connecting the twelve dynodes, the photocathode and the anode. For the R11410 and R11410-10, the recommended ratio was [99]:

K/G - D1	D1 - D2	D2 - D3	D3 - D4	D4 - D5	D5 - D6	D6 - D7	D7 - D8	D8 - D9	D9 - D10	D10 - D11	D11 - D12	D12 - P
4	1.5	2	1	1	1	1	1	1	1	1	2	1

where K marks the photocathode, G the focusing grid that has to be connected to the photocathode, P the anode and D1 - D12 the twelve dynode stages. This ratio was used in the first iterations of the base design, but later adjusted to reflect the changes in the last two resistors for the R11410-20 version of the PMT [93]:

K/G - D1	D1 - D2	D2 - D3	D3 - D4	D4 - D5	D5 - D6	D6 - D7	D7 - D8	D8 - D9	D9 - D10	D10 - D11	D11 - D12	D12 - P
4	1.5	2	1	1	1	1	1	1	1	1	1.5	1.5

This change is due to a modified geometry of the last two dynode stages in the R11410-20 that is meant to improve the linearity of the PMT. This new ratio has already been used in the later iterations of the base development described here despite the fact that only R11410 and R11410-10 versions were available at the time.
While the ratio between the resistors is fixed, the absolute resistance does not influence the PMT's gain and can thus be chosen arbitrarily depending on the need of linearity and the tolerance for heat dissipation.
A general decision has to be made whether to ground the photocathode and supply positive high voltage or to ground the anode and supply negative high voltage. For XENON1T, as it is also the case in XENON100, anode grounding will be used. This makes the output of the PMT less susceptible to any fluctuations in the high voltage, as these will change the overall gain of the PMT, but not directly spill onto the signal. It also makes the

connection to the read-out electronics easier as it is on the same potential as the anode, and removes the need for an additional protective capacitor on the base which would otherwise contribute to the total radioactivity.
In this base design the anode is connected to ground via a 1 kΩ resistor which protects the system from possible damage by build-up charge.
When using negative high voltage one has however to be careful as it is not only applied to the photocathode but also to the metal body of the PMT. It is therefore necessary to ensure that the PMTs stay electrically insulated from the rest of the detector. In XENON this is ensured by holding the PMTs in a PTFE structure which offers electrical insulation. A protective mesh is used in front of the photocathode plane in order to shield the PMTs from the fields in the TPC and vice versa.
As explained earlier, capacitors play an important role in preventing saturation of the PMT for large signals. The necessary capacitance to be added to the last dynode stage can be calculated from the size of the largest expected signals:

$$C = \frac{P \cdot G \cdot e}{|V|}, \tag{7.12}$$

where P is the number of photoelectrons in the signal, G is the total gain of the PMT and V is the voltage between the last dynode and the anode. For 10^5 photoelectron pulses, a gain of $5 \cdot 10^6$ and a supply voltage of – 1500 V the minimum necessary capacitance would thus be

$$C = \frac{10^4 \cdot 5 \cdot 10^6 \cdot e}{1500V \cdot \frac{1\Omega}{18.5\Omega}} = 987.9 \text{ pF}. \tag{7.13}$$

This gives a rough estimation for the capacitor connected to the last dynode. The necessary capacitance for the previous dynode stages will generally be lower. For a first prototype base, three 10 nF capacitors have been used in a circuit based on 1 MΩ resistors (Fig. 7.9 A). 50 Ω damping resistors are used with the last dynodes to prevent "ringing", a high-frequency oscillation on the PMT output signal [85].
Linearity measurements with a NaI scintillator and various radioactive sources however showed the need for a fourth capacitor connected to the tenth dynode (Fig. 7.9 B) to reach good linearity for signals of at least 9000 photons – the full range provided by this test method (Figs. 7.1 and 7.2). To investigate the linearity on a larger scale, the laser + LED method has been used. Results showed that the base provided good linearity up to a signal current of $\sim$ 30 mA ($\approx$ 37500 PE in a 1 µs long signal with a gain of $5{\cdot}10^6$) before

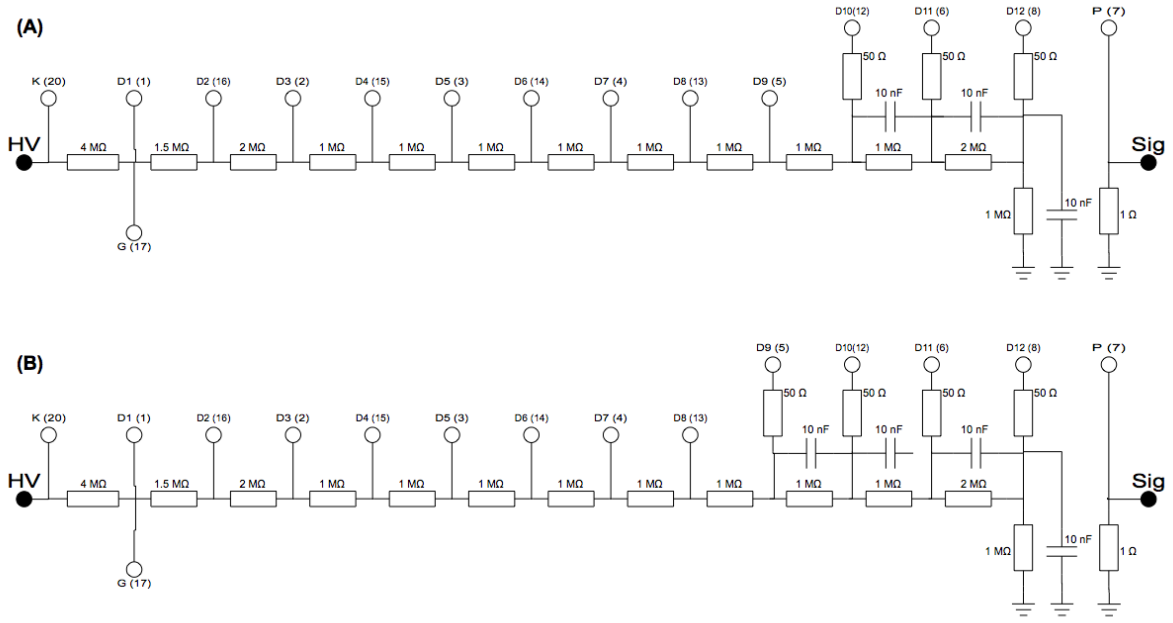

Figure 7.9: (A) First prototype for the R11410 PMT. (B) Modified base with additional capacitor after scintillator-based linearity tests.

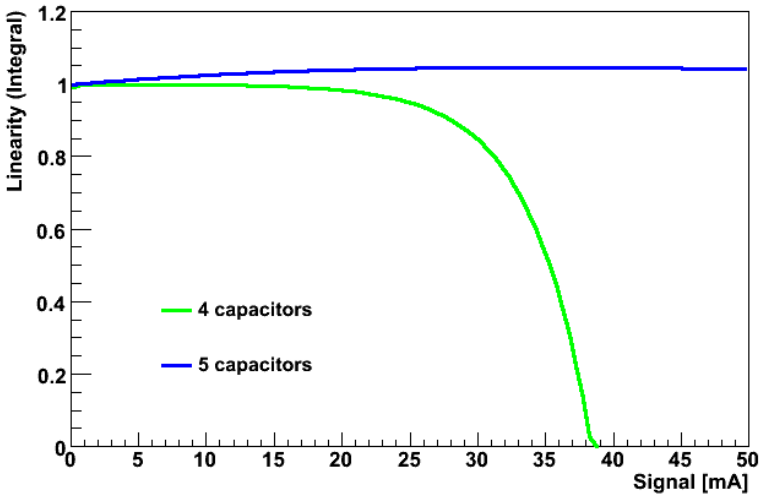

Figure 7.10: Comparison of the linearity of the same base with four (blue) and five (green) 10 nF capacitors at a signal rate of 10 Hz. The fifth capacitor is necessary to prevent saturation. In the absence of saturation slight overlinearity becomes apparent when using five capacitors.

saturating (see Fig. 7.10). This saturation threshold could not be increased even when using bigger capacitors up to 1 µF. It was found that the saturation occurred already on the eighth dynode stage and could be improved only by adding a fifth capacitor (Fig. 7.10). With this capacitor the base showed good linearity in the full range of the ADC, which now sets the limit for the signal range in XENON1T.

While the capacitors help to countervail saturation for single big signals, they cannot fight the overlinearity that comes from too high light influx, as the capacitors themselves need time to recharge after each signal. Even perfect linearity for large light pulses cannot ensure good linearity at high signal rates. As the requirements of the XENON1T detector do not allow for external voltage stabilisation measures such as Zener diodes or transistors, the only remaining parameter that can be optimised is the base current which is defined by the absolute resistance in the voltage divider chain. The R = 1 MΩ base has a total resistance of 18.5 MΩ. At the nominal supply voltage of – 1500 V a total power consumption of

$$P = N \cdot \frac{U^2}{R_{tot}} = 300 \cdot \frac{(-1500\ \mathrm{V})^2}{18.5\ \mathrm{M\Omega}} = 36.49\ \mathrm{W} \tag{7.14}$$

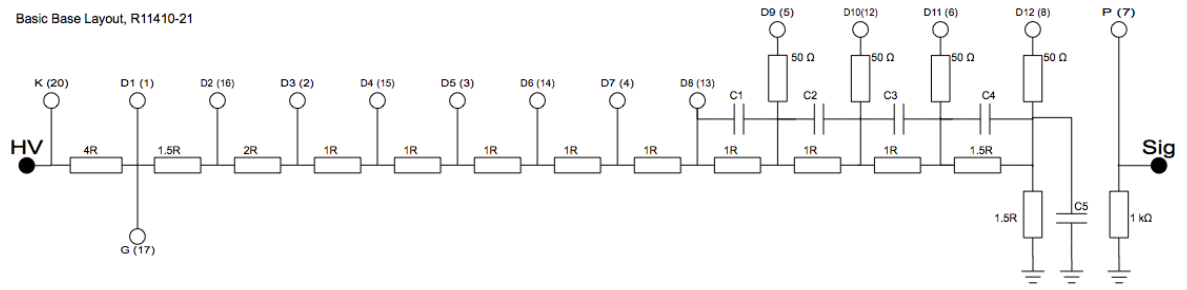

Figure 7.11: Basic base design with five capacitors. C1 has been added to the base design.

would be introduced into the detector from 300 PMTs. This is obviously far above the design goal of 5 W and even the maximum of 10 W allowed from the cryogenic system. Thus bases with higher resistance have been tested for their impact on the linearity. Resistors are not available with arbitrary values, especially with the reduced selection of cryogenic proof elements. The replacement of a desirable resistor by a series of available resistors adding up to the necessary resistance should be avoided because of the increased radioactivity this method would introduce. For this reason, only a few combinations for the different resistors in the voltage divider chain have been tested that are possible with readily available resistors at or close to the necessary ratios. Those are namely a design based on R = 7.5 MΩ and one with R = 5.1 MΩ (Fig. 7.12).

For good linearity, the anode current must amount to less than 1% of the total base current, and up to 10% for acceptable linearity [84]. So the maximal amount of photoelectrons P_{max} that can be measured linearly at a given repetition rate r can be estimated as:

$$P_{max} = \frac{U}{G \cdot e \cdot R_{tot} \cdot r \cdot 10} \tag{7.15}$$

where U is the PMT supply voltage, G the gain, R_{tot} the total resistance of the PMT base and e the electron charge. With the nominal supply voltage of $U = -1500$ V, the nominal gain of $G = 5 \cdot 10^6$ and a repetition rate of $r = 1$ kHz we expect $P_{max} \approx 10\,800$ for the 1 MΩ base, $P_{max} \approx 2\,120$ for the 5.1 MΩ base and $P_{max} \approx 1\,440$ for the 7.5 MΩ base. The worse linearity comes with an improvement in power consumption: 300 PMTs at – 1500 V would need 7.3 W with the 5.1 MΩ base and only 4.9 W with the 7.5 MΩ base. At 10 Hz signal rate no difference in linearity can be observed between the 5.1 MΩ base

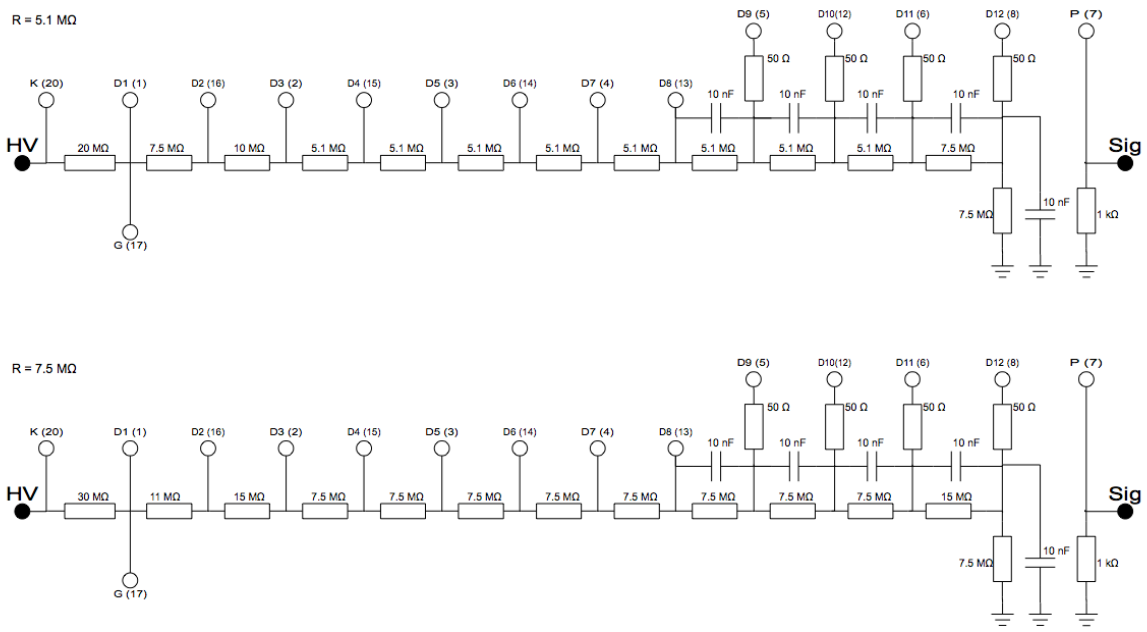

Figure 7.12: Base design with R = 5.1 MΩ and R = 7.5 MΩ.

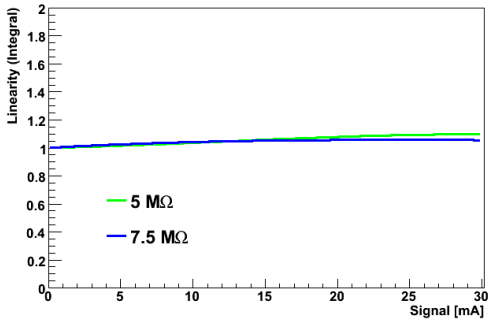

Figure 7.13: Integrated linearity of the 5.1 MΩ and the 7.5 MΩ base at 10 Hz signal rate.

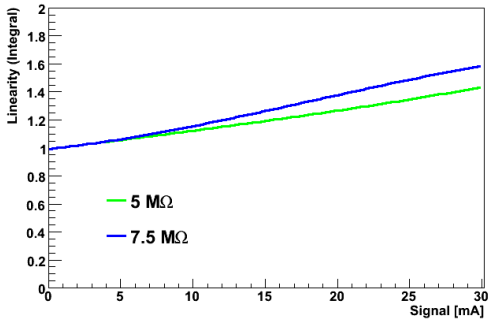

Figure 7.14: Integrated linearity of the 5.1 MΩ and the 7.5 MΩ base at 100 Hz signal rate.

and the 7.5 MΩ base over the range of the ADC (Fig. 7.13). But already at 100 Hz the linearity curves diverge, although both are showing overlinearity (Fig. 7.14). As the cryogenics can handle the additional heat, the 5.1 MΩ base has been selected as the final design.

7.1.5 Linearity of the Final Base Design

The final base layout can be found in Fig. 7.15. Some resistors diverge slightly from the ideal values due to the available low-radioactivity cryogen proof elements (see Section 7.3). The linearity of a base with this final layout has been tested at different signal rates. However, to ensure that the reduced capacitance at liquid xenon temperatures (see Fig. 7.28) does not cause saturation, the capacitors have been replaced by 5 nF capacitors for this black box test.

Additionally, an amplifier with a fixed gain of 10 (Phillips Model 776) has been used as such an amplifier will be used in XENON1T. The use of an amplifier allows to lower the voltage set to the PMT which in turn improves linearity and reduces heat production. In this test the voltage of the PMT was set to – 1200 V. The combined gain of the PMT and the amplifier was $3.6 \cdot 10^6$.

Figure 7.16 shows the measured linearity at different signal rates. The measurements have been done up to the point of ADC saturation. Due to the use of the amplifier this

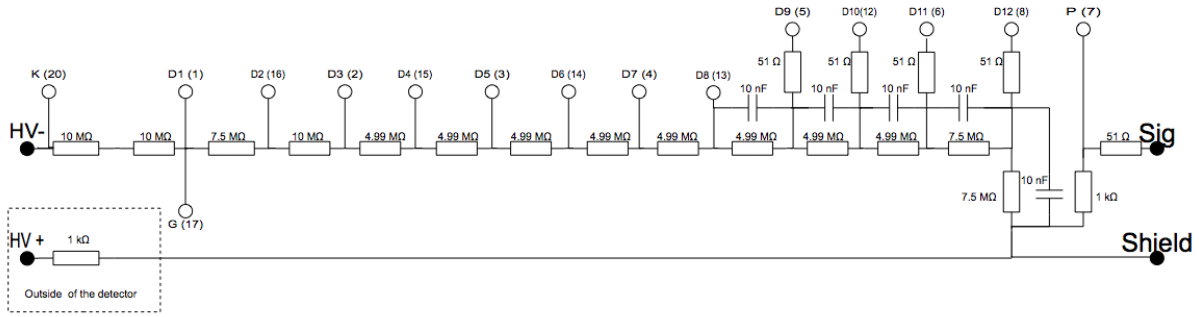

Figure 7.15: Final base design with the actual values of the resistors and capacitors that will be used.

upper bound corresponded to only a small signal current of $\sim$ 3.5 mA. As the PMT gain has been decreased accordingly, this corresponded to a signal size of $\sim$ 60 000 PE.
Good linearity has been observed over the whole range for signal rates of up to 250 Hz. At higher rates increased overlinearity has been observed. This is however unproblematic as calibration runs in XENON1T are expected to reach signal rates $<$ 300 Hz in individual PMTs.
No saturation has been observed at any point.
It seems that the base would provide good linearity even for larger signals than the ADC allows with this set-up. If electronic noise could be kept very low, it might be possible to decrease the PMT gain even further. Alternatively, one could use an amplifier with lower amplification gain in order to achieve a higher range of measurable signals. As discussed before (Section 7.1.3) the differential linearity measurement is especially sensitive to divergences of perfect linearity. An estimate of the ratio between the observed and the actual signal can be made by integration, but also measured with the fractional method. For this measurement a base has been sent to UCLA. The results are shown in Fig. 7.17. The measurements have been done at a bias voltage of – 1100 V, using a preamplifier. With this measurement the linearity seems to be good up to a signal current of $\sim$ 30 mA at a signal rate of 200 Hz. For the normal data taking in XENON1T the linearity of this base should be more than sufficient since large signals are expected to be a relatively rare occurence. Furthermore, the most important energy region will be that below 100 keV, or up to 3000 photoelectrons per PMT. But if the PMTs have to be biased with – 1500 V, non-linearity could be a problem during calibrations, which are

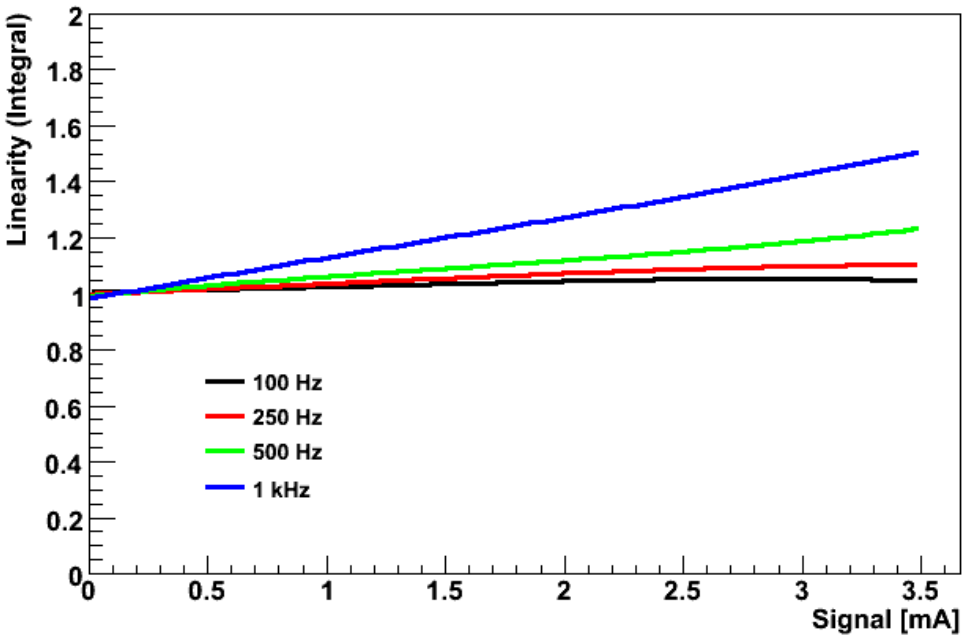

Figure 7.16: Integrated linearity of the final base design with reduced capacitance to simulate cold conditions measured at different signal rates. Good linearity is achieved up to 250 Hz.

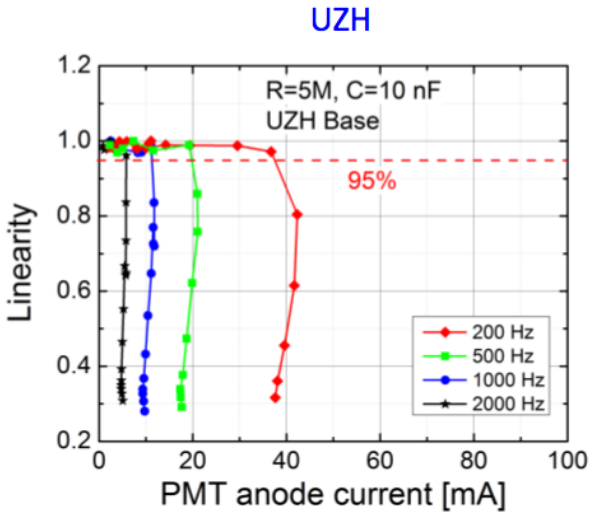

Figure 7.17: Fractional linearity of the final base design measured by A. Lyashenko at UCLA.

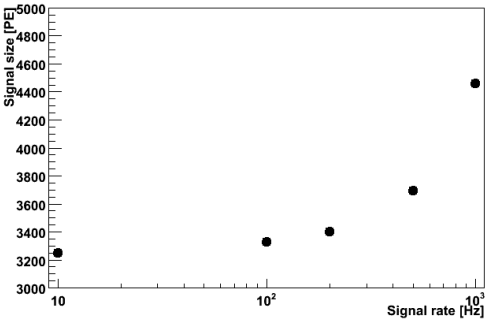

Figure 7.18: Apparent amplification of the laser signal size with increasing signal rate.

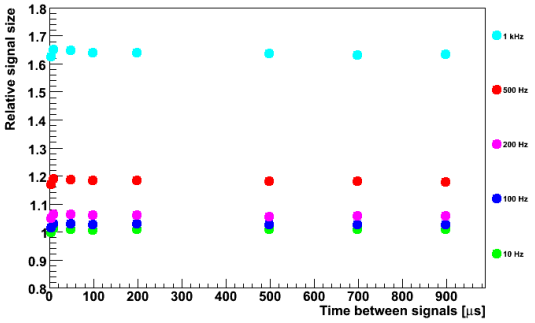

Figure 7.19: Apparent LED signal size at various time distances from the preceding laser pulse divided by the actual signal size.

likely to introduce a high-rate high-energy background. For this reason additional tests have been done in order to determine whether a small signal can still be measured linearly in the presence of a high rate of large signals. In the black box the laser has been set to emit light pulses of ≈ 3300 photoelectrons which would correspond roughly to a 110 keV signal in XENON1T. If the rate of the laser pulses is increased, overlinearity leads to an apparent amplification in the size of the laser pulses (Fig. 7.18). An LED signal of about 1650 photoelectrons (corresponding roughly to 55 keV signal in XENON1T) has now been emitted at a constant time between 4 and 900 μs after each laser signal. The mean size of the LED signals has been measured and compared to the true pulse size measured at 10 Hz without any preceding laser pulses. As can be seen in Fig. 7.19, the apparent size of the LED signal, like the laser signals, varied with the signal rate. This is expected since the high intra-PMT current produced by the high-rate laser pulses leads to an overall change of the PMT's gain. However, the LED signal size only depended on the time passed since the laser pulse for time distances $< 10\mu$s, where some saturation has been observed.

As the change in linearity seems to stem only from the average current flowing through the PMT rather than the individual preceding signals, it should be possible to get linear results even in a high-rate high-energy background environment as long as this background

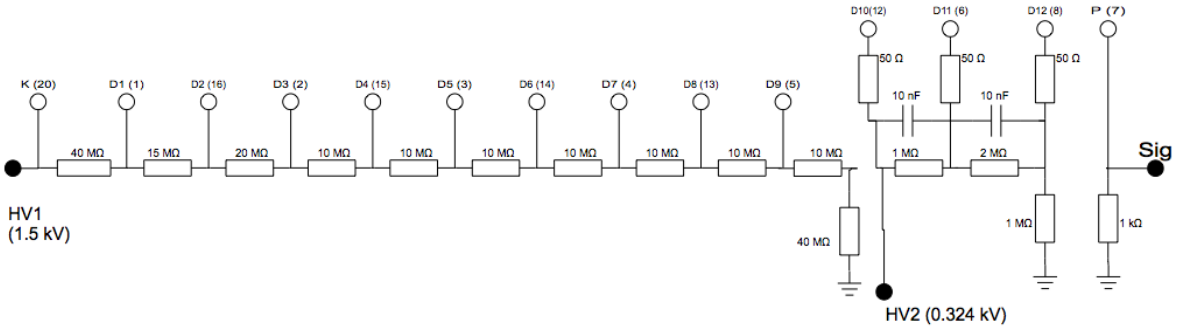

Figure 7.20: Base design with two separate voltage divider circuits for improved linearity at low power consumption.

rate is relatively stable and the gain has been measured under these conditions.

7.1.6 Alternative Approach with Two High Voltage Circuits

An alternative base design has been studied that employs a separate voltage divider circuit for the last three dynodes (Fig. 7.20). While the resistors connecting the first nine dynodes have been chosen in the order of 10 MΩ, the second circuit uses resistors in the order of 1 MΩ. This accounts for the fact that the current flowing inside the PMT is highest at the end of the dynode chain and the voltage stability in the last dynodes is therefore most relevant for the linearity of the base at high signal rates. The low resistance circuit allows high base currents to the last dynodes, but only over the much smaller voltage difference of the last dynode stages, while the main part of the total voltage difference is supplied with much smaller currents. Hence the linearity can be kept while reducing the total power consumption and thus the generated heat. At – 1500 V supply voltage the total power consumption for 300 PMTs would be 11.63 W. The current through the second resistor chain is 81.90 µA.

To keep the same high voltage dependence of the gain as in the usual base designs with only one circuit, both voltages have to be changed simultaneously. In order to reduce the amount of high voltage cables it was tested whether the gain could be adjusted by changing only the voltage on the last dynodes (the “low voltage”), which would allow to

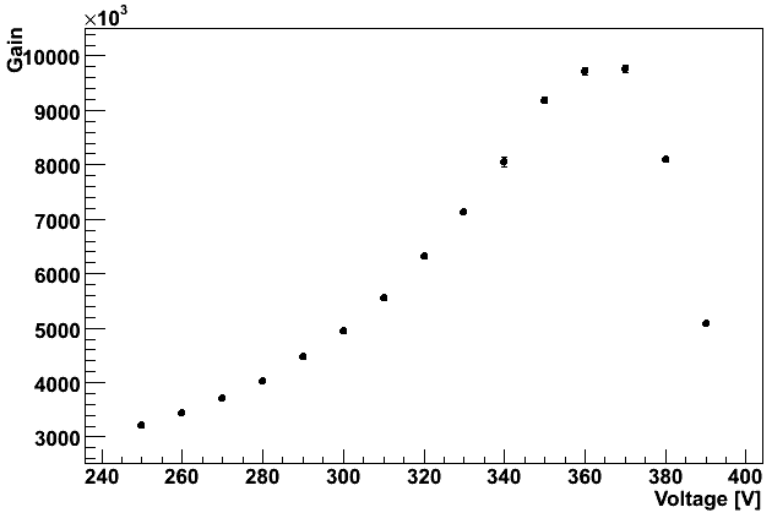

Figure 7.21: Gain with the double-circuit base for different low voltages with the high voltage constant at – 1600 V.

use a common high voltage for the first divider chain of all PMTs. As can be seen in Figure 7.21, this is indeed possible up to a certain point. If the low voltage is however increased too much, the voltage difference between dynode 9 (the last dynode of the high voltage chain) and dynode 10 (the first dynode of the low voltage chain) decreases until the electrons are no longer collected on dynode 10 and the gain drops steeply. Choosing a higher constant voltage applied to the first dynodes increases the gain range to which the PMT can be set.

Using two prototype bases with two voltage circuits, it has been shown that it is indeed possible to adjust the gain of two PMTs while using a common high voltage supplied to the first circuit of both PMTs (Fig. 7.22). While a common high voltage would solve the problem of extra cables necessary for this solution, it would make it impossible to switch off an individual PMT if necessary mid-operation of the experiment. Work on a double circuit base has therefore not been pursued further.

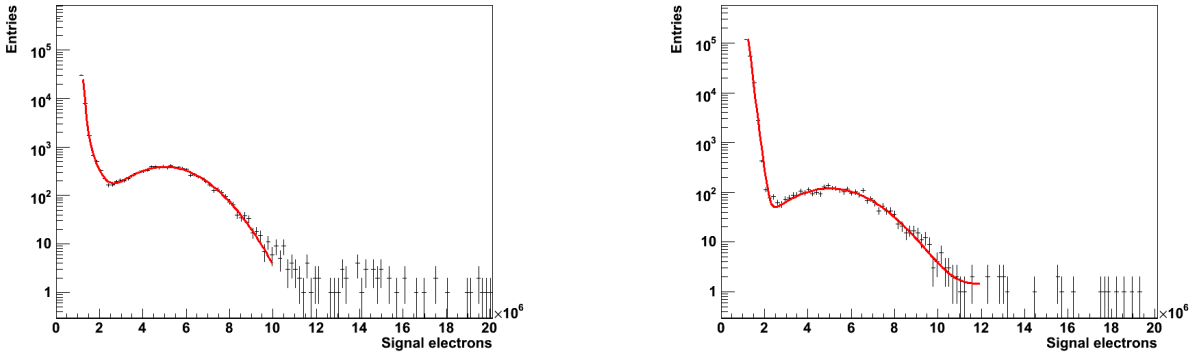

Figure 7.22: SPE spectra of two PMTs with a common constant high voltage of –1600 V adjusted to the same gain. Left: PMT ZK5626, low voltage –338 V, gain 5.00 $\cdot 10^6$. Right: PMT ZK5629, low voltage –302 V, gain 5.01 $\cdot 10^6$.

7.2 Signal Quality

7.2.1 Grounding

The grounding scheme for XENON1T can be found in Fig. 7.23. The HV return will be kept floating against ground to prevent grounding loops. Fluctuations might however be picked up as electronic noise on the shielding of the PMTs' signal cables as they are connected to the HV return on the base. To decouple this, an additional 1 kΩ resistor has been placed between the PMT ground used for signal shielding and the HV return (resistor R1 in Fig. 7.24). This resistor will be put however not on the base itself, but outside the detector lest it increases the overall radioactivity introduced by the base.

7.2.2 Impedance Matching

In the black box tests used in designing the base only short cables ($<$ 1m) have been used from base to read-out. However, in XENON1T the signal way will be several meters long, as the signal has to be lead out of the detector itself and through the water tank before it can be fed into any read-out electronics. In this case the impedance of the base signal output has to be matched with that of the cables. This is done by using an additional resistor (R2 in Fig. 7.24). It is not determined yet which type of cables will be used for the final assembly, but it is expected that they will have an impedance of 50 Ω.

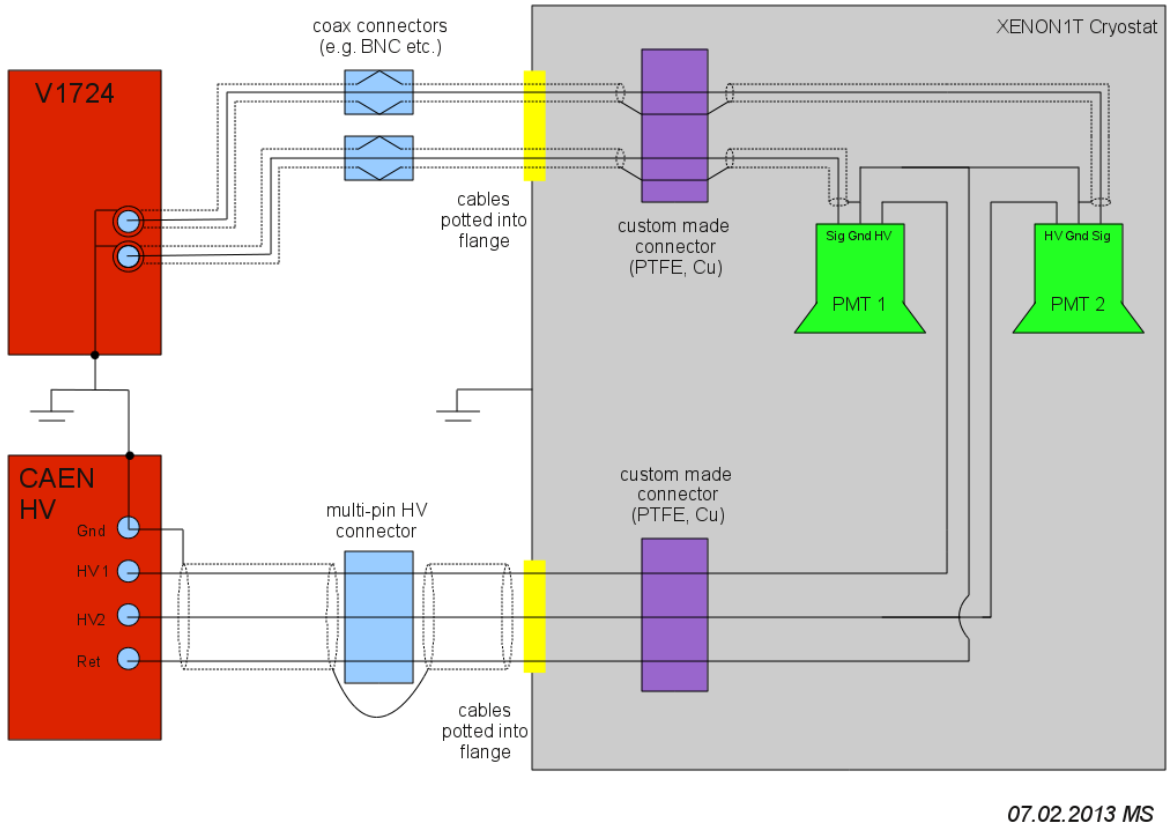

Figure 7.23: Grounding scheme for XENON1T. Drawing by Marc Schumann.

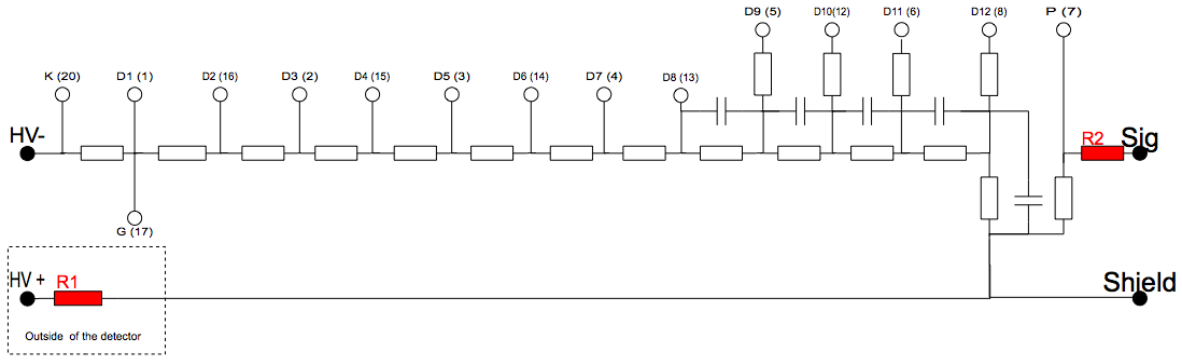

Figure 7.24: Two additional resistors ensure signal quality. R1 decouples the ground of the signal shielding from the HV return and is placed not on the base but outside the detector. R2 matches the impedance of the signal cable to prevent reflections.

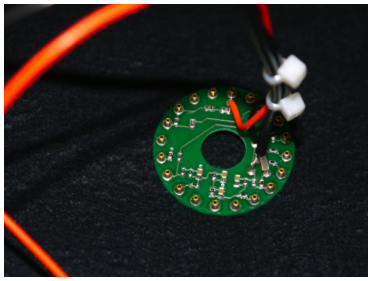

Figure 7.25: Test base made from FR4.

Figure 7.26: Test base made from PTFE.

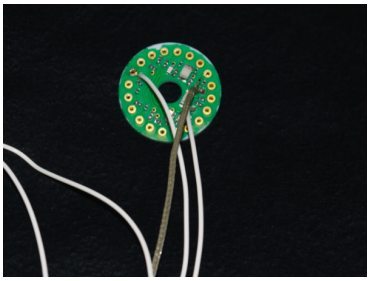

Figure 7.27: Test base made from CuFlon.

7.3 Material Selection

Numerous versions of the base have been built during the design process. For most prototypes standard FR4 printed circuits have been used (Fig. 7.25) with no special attention to the resistors and capacitors other than their resistance and capacitance values and the limiting voltage. The bases have been connected to the PMT's pins with spring-loaded sockets allowing frequent and quick changes. Standard coaxial cables have been used, with BNC-type connectors for the signal output and SHV connectors for the supply voltage.

Materials that have been used for tests in liquid xenon have been selected more carefully. These bases have been made from custom-made PTFE disks (Fig. 7.26), in which the same spring-loaded sockets have been inserted. Resistors and capacitors suitable for cryogenic temperatures have been soldered directly to these sockets. HV and signal have been connected via PTFE insulated cables screwed to the feed-throughs of the Dewar vessel.

For the final base used in XENON1T however every component needs to fulfil a strict list of requirements: In addition to the resistance to and longevity in liquid xenon temperatures the minimisation of the radioactive background introduced by the materials is of high importance.

As for all materials used in the XENON1T detector, all candidate elements for the PMT bases have been carefully screened by the XENON screening group (A. Ferella at LNGS, J. Schreiner at MPIK and F. Piastra at UZH) using the high sensitivity Germanium detectors Gator [95] and GeMPI [100].

7.3.1 Substrate

The substrate is the building material for the print on which all other components of the PMT base are mounted. As it might be necessary to exchange bases in situ during the construction and commissioning of the detector, the substrate should show enough rigidness to allow easy plugging of the base onto the PMT's pins. The shape should also be stable in cooling to liquid xenon temperatures. Furthermore, as for all components that enter the detector, the substrate should contribute as little as possible to the radioactive background. Outgassing should be low and no materials that are solvable in liquid xenon should be included.

Two material candidates have been examined: Cirlex and CuFlon. Screening of raw prints made from the two materials for unrelated PMT bases in different projects suggested that CuFlon could be the cleaner choice (Table 7.1).

CuFlon consists of a PTFE sheet plated with copper. As PTFE is quite flexible, the highest available standard thickness – 3.18 mm – was used for test bases (Fig. 7.27). However, it was found that even then the conductive paths can easily be separated from the substrate and break when the print is bent or cooled down quickly.

Due to this problem Cirlex has been selected for the bases in XENON1T. It is an adhesiveless polyimide laminate that has already been used with good results for the bases in XENON100. It is much stiffer than CuFlon, and the same thickness has been chosen as in XENON100, 0.06 inch (1.524 mm).

Name	^{238}U	^{226}Ra	^{228}Ra	^{228}Th	^{40}K	^{60}Co	^{137}Cs
Cirlex prints	<0.16 µBq	14.6 ± 1.7 µBq	<4.95 µBq	3.0 ± 1.0 µBq	33.0 ± 10.0 µBq	<0.98 µBq	<1.23 µBq
CuFlon	<6.43 µBq	<0.22 µBq	<0.51 µBq	<0.33 µBq	<1.90 µBq	<0.10 µBq	<0.10 µBq

Table 7.1: Screening results for raw Cirlex and CuFlon prints for unrelated bases for different PMTs, with unplated copper and without solder mask, per piece. Results provided by the XENON screening group.

7.3.2 Resistors

For the resistors, candidates from three different series (Table 7.2) have been screened, all of which fulfil the basic requirements regarding resistance to liquid xenon temperatures and the voltages applied to the base circuit. As some values are not readily available,

the 20 MΩ resistor is substituted by two 10 MΩ resistors, and instead of 5 MΩ resistors, resistors with slightly different nominal values (between 4.9 and 5.1 MΩ) can be used without noticeable changes in black box tests.
From the candidates, those with the lowest radioactive contamination (Table 7.3) have been selected for use in the final base. These are KTR03EZPF1005 (10 MΩ), CRCW08057-M50FKEA (7.5 MΩ), CRCW08054M99FKEA (5 MΩ), ERJ-2RKF1001X (1 kΩ) and ERJ-2RKF51R0X (51 Ω). In some cases the resistors with the lowest total radioactivity are not the ones using the least material, so that more space is needed in the print layout in order to accommodate the cleanest components.

Name	Manufacturer	Resistance	Size	Precision	Limiting voltage	Temperature coefficient
KTR03EZPF1005	Rohm Semiconductor	10 MΩ	0603	1%	350 V	100 ppm/°C
CRCW08057M50FKEA	Vishay Dale	7.5 MΩ	0805	1%	150 V	100 ppm/°C
KTR03EZPF7504	Rohm Semiconductor	7.5 MΩ	0603	1 %	350V	100 ppm/°C
CRCW08054M99FKEA	Vishay Dale	4.99 MΩ	0805	1 %	150 V	100 ppm/°C
KTR03EZPF5104	Rohm Semiconductor	5.1 MΩ	0603	1 %	350 V	100 ppm/°C
ERJ-3EKF1001V	Panasonic Electronic Components	1 kΩ	0603	1 %	75 V	100 ppm/°C
ERJ-2RKF1001X	Panasonic Electronic Components	1 kΩ	0402	1 %	50 V	100 ppm/°C
ERJ-3EKF51R0V	Panasonic Electronic Components	51 Ω	0603	1 %	150 V	100 ppm/°C
ERJ-2RKF51R0X	Panasonic Electronic Components	51 Ω	0402	1 %	100V	100 ppm/°C

Table 7.2: Resistor types that have been screened as candidates for the R11410 base to be used in XENON1T.

Name	^{238}U	^{226}Ra	^{228}Ra	^{228}Th	^{40}K	^{60}Co	^{137}Cs
KTR03EZPF1005	<40 µBq	5.4 ± 0.4 µBq	7.0 ± 0.7 µBq	5.7 ± 0.6 µBq	3.3 ±0.6 µBq	<0.1 µBq	<0.3 µBq
CRCW08057M50FKEA	<40 µBq	2.1 ± 0.5 µBq	<2.8µBq	<1.1 µBq	21.3 ±4.9 µBq	<0.5 µBq	<0.8µBq
KTR03EZPF7504	<1.5 µBq	7.9 ± 1.3 µBq	<5.5 µBq	4.6 ± 2.0 µBq	<17 µBq	<0.7 µBq	<0.7 µBq
CRCW08054M99FKEA	<40 µBq	2.1 ± 0.5 µBq	<2.8 µBq	<1.1 µBq	21.3 ± 4.9 µBq	<0.5 µBq	<0.8 µBq
KTR03EZPF5104	<115 µBq	9.6 ± 1.3 µBq	4.5 ± 2.2 µBq	5.3 ± 1.9 µBq	21.9 ± 5.4 µBq	<0.6 µBq	<1.0 µBq
ERJ-3EKF1001V	<208 µBq	7.4 ± 1.3 µBq	5.3 ± 2.2 µBq	<6.1 µBq	<16.4 µBq	<0.7 µBq	<1.0µBq
ERJ-2RKF1001X	<145 µBq	2.6 ± 1.1 µBq	<3.9 µBq	<4.0 µBq	<9.4 µBq	<0.8 µBq	<1.5 µBq
ERJ-3EKF51R0V	<322 µBq	<13.6 µBq	<12.1 µBq	<9.9 µBq	<14.1 µBq	<0.7 µBq	<1.1 µBq
ERJ-2RKF51R0X	<120 µBq	<1.5 µBq	3.1 ± 1.9 µBq	<2.6 µBq	<10 µBq	<0.9 µBq	<0.8 µBq

Table 7.3: Screening results for the resistors that have been candidates for the R11410 base to be used in XENON1T. Results provided by the XENON screening group.

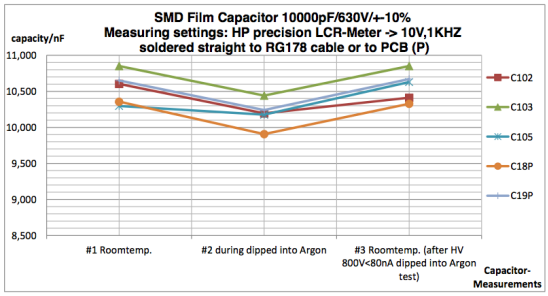

Figure 7.28: Measured capacitance of the 10 nF ceramics capacitors before, during and after cooling. Figure by K. Jaenner.

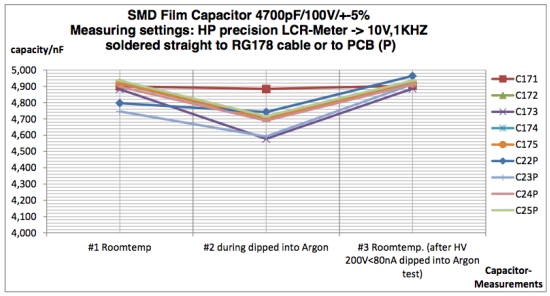

Figure 7.29: Measured capacitance of the 4.7 nF PEN capacitors before, during and after cooling. Figure by K. Jaenner.

7.3.3 Capacitors

Two types of capacitors have been tested: one 10 nF element made from X7R ceramics, and one 4.7 nF polyethylene naphthalate (PEN) film capacitor. It has been found in black box tests that the minimum capacitance for good linearity of the base for big signals is 3 nF for the last capacitor and 1 nF for the other capacitors. The capacitance is however reduced in cold temperatures, especially for ceramics. This has been tested by K. Jaenner at Max Planck Institute for Nuclear Physics (MPIK) in Heidelberg by measuring the capacitance of the candidate elements when dipped in liquid argon. The chosen capacities appear to be adequate for both capacitor types also in cold (Figs. 7.28 and 7.29).
Also the radioactive background for the two materials is comparable (Table 7.5). Both seem to be a good choice for the base. The PEN capacitors are however much bigger than the ceramics capacitors (4.8 mm x 3.3 mm instead of 0.6 mm x 0.3 mm), and there is already good experience using X7R in XENON100, therefore the 10 nF ceramics capacitors have been selected to be used in the bases.

Name	Manufacturer	Material	Capacitance	Size	Precision	Limiting voltage
C0603C103K2RACTU	Kemet	X7R	10 nF	0603	10%	200 V
ECWU2472KC9	Panasonic Electronic Components	PEN	4.7 nF	4.8 mm x 3.3 mm	10%	250 V

Table 7.4: Capacitor types that have been screened as candidates for the R11410 base to be used in XENON1T, per piece.

Name	^{238}U	^{226}Ra	^{228}Ra	^{228}Th	^{40}K	^{60}Co	^{137}Cs
C0603C103K2RACTU	<105 µBq	36 ± 2.7 µBq	26.4 ± 3 µBq	5.7 ± 1.9 µBq	<13.7 µBq	<0.4 µBq	<1.2 µBq
ECWU2472KC9	<69 µBq	<3.0 µBq	<3.6 µBq	70 ± 20 µBq	<11 µBq	<0.86 µBq	<0.82 µBq

Table 7.5: Screening results for the capacitors that have been candidates for the R11410 base to be used in XENON1T, per piece. Results provided by the XENON screening group.

7.3.4 Sockets

Sockets are used in order to connect the base to the pins of the PMT. This allows to quickly exchange a base or PMT in the testing phase before installation in case one is broken, and facilitates the installation process enormously as opposed to soldering the pins individually to the base. Spring loaded gold plated sockets ensure good contact. However, spring copper always contains beryllium, as it improves the elasticity of the copper. For this reason sockets have been chosen with a body of pure copper. Only the spring itself, making up for about half of the material of the socket, consists of qq-c-533 spring copper which is a mixture of 98% copper, 1.9% beryllium and 0.1% cobalt. The sockets are plated with gold over nickel. The screening results can be found in Table 7.6. The sockets have been found to provide reliable good connections both at room temperature and in liquid xenon even after frequent use. While the beryllium contamination is a concern, this system will be used also in XENON1T as it promises to vastly decrease the chances of wrong or bad connections that would come with in-situ soldering of all PMTs to their bases during installation.

Name	^{238}U	^{226}Ra	^{228}Ra	^{228}Th	^{40}K	^{60}Co	^{137}Cs
2-331677-6	96 ± 16 µBq	0.26 ± 0.09 µBq	0.89 ± 0.18 µBq	1.5 ± 0.2 µBq	3.1 ± 0.8 µBq	<0.083 µBq	<0.095 µBq

Table 7.6: Screening results for the sockets to be used on the R11410 bases in XENON1T, per piece. Results provided by the XENON screening group.

7.3.5 Cables

The bases will be connected with two cables, one for the high voltage and one for the read-out of the anode signal of the PMT. These cables must be suitable for use in liquid xenon and provide good signal quality. Selecting the cable type also involves consideration

of grounding issues and how the cables will be connected. It is important to also take into account the installation process, as the cables will be guided through both the cryostat and the surrounding water tank. One possibility would be to use a short cable on the base, which can be linked to a longer cable by a dedicated connector. It might also be possible to connect the cable to the base with the same type of socket as used for plugging the base onto the PMT. At time of production of the base it was not clear yet which type of cable will be used. For this reason only generic solder eyelets have been foreseen for the installation of the cables.

7.3.6 Assembly

The complete bases will consist of ring-shaped Cirlex prints that will be populated with the selected elements. The prints have a diameter of 35 mm and a thickness of 1.524 mm. At the centre a hole with a diameter of 9.5 mm gives room for the PMT bulb stem. The conductive paths will be made from copper, plated with lead-free tin solder leveling. No solder mask will be used. In order to prevent accidental solder bridges the layout has been designed in a way that maximises the distance at the critical points.
A total of 20 resistors (and one additional resistor outside of the detector), 5 capacitors and 15 sockets will be used for each base. The projected total radioactivity of the base can be found in Table 7.7.

Component	^{238}U	^{226}Ra	^{228}Ra	^{228}Th	^{40}K	^{60}Co	^{137}Cs
Cirlex print	<0.22 µBq	20 ± 6.84 µBq	<6.84 µBq	4.14 ± 1.38 µBq	45.59 ± 13.81 µBq	<1.35 µBq	<1.70 µBq
Resistors	<1189.5 µBq	<43.64 µBq	<63.22 µBq	<43.29 µBq	<243.3 µBq	<9.68 µBq	<12.87 µBq
Capacitors	<525 µBq	315.0 ± 13.5 µBq	132 ± 15 µBq	28.5 ± 9.5 µBq	<68.5 µBq	<2 µBq	<6 µBq
Sockets	1440 ± 240 µBq	3.90 ± 1.35 µBq	13.35 ± 2.70 µBq	22.5 ± 3.0 µBq	46.5 ± 12.0 µBq	<1.25 µBq	<1.43 µBq
Total base	<3.15 mBq	<0.38 mBq	<0.22 mBq	<0.10 mBq	<0.40 mBq	<0.01 mBq	<0.02 mBq

Table 7.7: Projected total radioactivity of the PMT base.

Chapter 8

Conclusions

The XENON100 detector has been taking science data for more than three years. It did not detect dark matter and was able to set the most stringent exclusion limit on spin-independent WIMP-nucleon scattering to date. The nature of dark matter is therefore still unknown. A new detector, XENON1T, is now being built that will hopefully help to solve this mystery.

The light detectors in the XENON TPC play a crucial role for the success of the experiment. In XENON100, weekly calibrations with LED light were used to monitor the PMTs' properties. The PMTs have been found to be generally very stable, and the gain calibrations have allowed to promptly adjust for any changes.

The electromagnetic background spectrum in the 2011/2012 science run has been fitted with data from Monte Carlo simulations. While this method is useful for cross-checks, it is not as precise in determining the amount of krypton and radon in the liquid xenon as other methods, such as direct spectroscopy measurements or delayed coincidence counting. However, these studies also led to the discovery that the position-dependent correction of the S2 signals used in the 2011/2012 science run was not accurate. A new correction map improves the resolution especially for high-energy signals.

The Hamamatsu R11410 PMTs have been evaluated as a candidate for the instrumentation of the XENON1T detector (Chapter 6). It has been found to be very stable both in continuous operation for more than four months in liquid xenon and during five consecutive cooling cycles. Furthermore, no problems have been observed while operating three PMTs together in gaseous xenon in the presence of electric fields. Due to their

high quantum efficiency, their high gain and good single photoelectron resolution, their low radioactivity and their stability during long-time operation in liquid xenon, they have been selected as light sensors for the XENON1T experiment.

The PMTs need to fulfil several requirements of which many depend not only on the PMT itself but also on its voltage divider base. It needs to provide high gain and good single photoelectron resolution while staying linear for light signals up to $\sim$ 100000 photoelectrons at signal repetition rates of $\sim$ 300 Hz. At the same time the total power consumption for all 248 PMTs needs to stay below 10 W, so it does not introduce too much heat into the liquid xenon. The PMT's gain should be adjustable via the supplied voltage, and it is required that individual PMTs can be switched off should they break. In order to keep the overall radioactive background as low as possible, the total amount of elements needs to be kept at a minimum, and all material needs to be not only suitable for the use in liquid xenon but also selected for low radioactive contamination.

The design of the voltage divider base for the R11410 PMT has been described in Chapter 7. This base is optimised regarding all those requirements, with the necessity of a compromise especially between linearity and power consumption. Whether the R11410 PMTs in the XENON1T detector will be able to use the full signal range in which they are linear will now depend on the choices for the read-out electronics, as also the ADC can saturate for larger signals if an additional preamplifier is used.

Acknowledgements

I want to thank the many people without whom this thesis would not have possible.
My gratitude goes to Prof. Dr. Laura Baudis who gave me the opportunity to work in the exciting field of direct dark matter detection. Thank you for the possibility to work on interesting projects both with hardware and with data analysis.
I would also like to thank all people involved in the XENON collaboration.
Special thanks go to Prof. Dr. Marc Schumann, Dr. Alfredo Ferella and Prof. Dr. Rafael Lang from whom I learned a lot through all the years that I was involved with the XENON project.
I am grateful to Dr. Alex Kish and Dr. Ali Askin for the nice times we spent together in Italy, for introducing me to the operation of the XENON100 detector and to the analysis of the XENON100 data.
I would like to thank the XENON screening group, Dr. Alfredo Ferella, Dr. Jochen Schreiner and Francesco Piastra for all the work they did screening the various elements I considered for the use on the XENON1T PMT bases.
I am thankful to Prof. Dr. Katsushi Arisaka and Dr. Peter Shagin for providing me with their knowledge of PMTs and the bases that were used in XENON100.
Thanks go to Gaudenz Kessler for taking over the weekly gain calibration of the XENON100 PMTs and for looking after the long-time stability test of the R11410 PMT while I was attending a winter school. Thanks also go to Dr. Aaron Manalaysay who rushed to help me finding emergency nitrogen for the MarmotX detector on a Sunday night. Special thanks to Andreas James who contributed to all operation in the Zurich lab in so many ways.
I am very thankful to Dr. Martin Auger, Dr. Teresa Marrodán Undagoitia and Daniel Mayani for reading the manuscript of this thesis and providing me with helpful comments.

I want to thank all other past and present members of my group: Dr. Sebastian Arrenberg, Dr. Tobias Bruch, Dr. Francis Froborg, Dr. Kiran Kumar Guthikonda, Dr. Marijke Haffke, Dr. Roberto Santorelli, Dr. Michal Tarka, Dr. Eirini Tziaferi, Peter Barrow, Giovanni Benato, Payam Pakarha and Manuel Walter.
I am also grateful to the people of our institute that have helped me throughout my time here: Roland Bernet, Monika Röllin, Ruth Halter, Carmelina Genovese, Tiziano Crudeli, Kurt Bösinger and all other people working in the workshop and in the electronics workshop. My deep gratitude goes to Daniel Florin who helped me times and times again in designing the circuit layout for the R11410 base, selecting suitable components and soldering so many test bases.
I want to thank the University of Zurich for funding my thesis with a Forschungskredit scholarship.
Finally, I want to thank my parents, my sister and especially Albert Bursche for all their support and encouragement.

List of Figures

List of Tables

Bibliography

[1] F. Zwicky. Die Rotverschiebung von extragalaktischen Nebeln. *Helv. Phys. Acta*, 6:110–127, 1933.

[2] F. Zwicky. On the Masses of Nebulae and of Clusters of Nebulae. *ApJ*, 86:217–246, 1937.

[3] S. Smith. The mass of the Virgo Cluster. *ApJ*, 83:23–30, 1936.

[4] M. L. Humason and H. D. Wahlquist. Solar motion with respect to the local group of nebulae. *AJ*, 60:254–258, 1955.

[5] M. S. Roberts. A high-resolution 21-cm hydrogen-line survey of the andromeda nebula. *ApJ*, 144:639–356, 1966.

[6] V. C. Rubin et al. Rotational properties of 21 Sc galaxies with a large range of luminosities and radii, from NGC 4605 (R = 4 kpc) to UGC 2885 (R = 122 kpc). *ApJ*, 238:471–487, 1980.

[7] T. S. van Albade et al. Distribution of dark matter in the spiral galaxy NGC 3198. *ApJ*, 295:305–313, 1985.

[8] D. Clowe et al. A direct empirical proof of the existence of dark matter. *ApJL*, 648:L109–L113, 2006.

[9] M. Milgrom. A modification of the Newtonian dynamics as a possible alternative to the hidden mass hypothesis. *ApJ*, 270:365–370, 1983.

[10] C. L. Bennett et al. 4-Year COBE DMR Cosmic Microwave Background Observations: Maps and Basic Results. *ApJ*, 464:L1–L4, 1996.

[11] E. Komatsu et al. Seven-year Wilkinson Microwave Anisotropy Probe (WMAP) observations: cosmological interpretation. *ApJS*, 192, 2011.

[12] P. A. R. Ade et al. (Planck collaboration). Planck 2013 results. XVI. Cosmological parameters. *arXiv:1303.5076*, 2013.

[13] K. Garrett and Gintaras Dūda. Dark Matter: A Primer. *Adv. Astron.*, page 968283, 2011.

[14] M. Ackermann et al. Search for Gamma-ray Spectral Lines with the Fermi Large Area Telescope and Dark Matter Implications. *arXiv:1305.5597*, 2013.

[15] J. Aleksic et al. (MAGIC Collaboration). Searches for Dark Matter annihilation signatures in the Segue 1 satellite galaxy with the MAGIC-I telescope. *JCAP*, 2011.

[16] A. Abramowski et al. (H.E.S.S. Collaboration). Search for a Dark Matter annihilation signal from the Galactic Center halo with H.E.S.S. *PRL*, 106:161301, 2011.

[17] M. G. Aartsen et al. (IceCube Collaboration). Search for Dark Matter Annihilations in the Sun with the 79-String IceCube Detector. *PRL*, 110:131302, 2013.

[18] S. Adrián-Martínez et al. First Search for Dark Matter Annihilation in the Sun Using the ANTARES Neutrino Telescope. *arXiv:1302.6516*, 2013.

[19] O. Adriani et al. The cosmic-ray positron energy spectrum measured by PAMELA. *arXiv:1308.0133*, 2013.

[20] M. Aguilar et al. (AMS Collaboration). First Result from the Alpha Magnetic Spectrometer on the International Space Station: Precision Measurement of the Positron Fraction in Primary Cosmic Rays of 0.5 - 350 GeV. *PRL*, 110:141102, 2013.

[21] ATLAS Collaboration. Search for Dark Matter Candidates and Large Extra Dimensions in events with a photon and missing transverse momentum in *pp* collision data at $\sqrt{s}$=7 TeV with the ATLAS detector. *PRL*, 110:011802, 2013.

[22] CMS Collaboration. Search for New Physics with a Mono-Jet and Missing Transverse Energy in pp Collisions at $\sqrt{s}$=7 TeV. *PRL*, 107:201804, 2011.

[23] D. G. Cerdeño and A. M. Green. Direct Detection of WIMPs. In G. Bertone, editor, *Particle Dark Matter*. Cambridge University Press, 2010.

[24] J. D. Lewin and P. F. Smith. Review of mathematics, numerical factors, and corrections for dark matter experiments based on eleastic nuclear recoil. *Aph*, 6:87–112, 1996.

[25] F. J. Kerr and D. Lynden-Bell. Review of galactic constants. *Mon. Not. R. ast. Soc.*, 221:1023–1038, 1986.

[26] A. K. Drukier et al. Detecting cold dark-matter candidates. *PRD*, 33:3495–3508, 1986.

[27] K. Freese et al. Annual modulation of dark matter: A review. *arXiv:1209.3339*, 2012.

[28] M. C. Smith et al. The RAVE survey: constraining the local galactic escape speed. *Mon. Not. R. Astron. Soc.*, 379:755–772, 2007.

[29] G. Jungman et al. Supersymmetric Dark Matter. *Phys. Repts.*, 267:195–373, 1996.

[30] R. Bernabei et al. The DAMA/LIBRA apparatus. *NIM A*, 592:297–315, 2008.

[31] C. E. Aalseth et al. (CoGeNT Collaboration). CoGeNT: A Search for Low-Mass Dark Matter using p-type Point Contact Germanium Detectors. *PRD*, 88:012002, 2013.

[32] R. Agnese et al. (CDMS Collaboration). Silicon detector results from the first five-tower run of CDMS II. *PRD*, 88:031104(R), 2013.

[33] E. Armengaud et al. (EDELWEISS Collaboration). Final results of the EDELWEISS-II WIMP search using a 4-kg array of cryogenic germanium detectors with interleaved electrodes. *Phys. Let. B*, 702:329–335, 2011.

[34] E. Armengaud et al. (EDELWEISS Collaboration). A search for low-mass WIMPs with EDELWEISS-II heat-and-ionization detectors. *PRD*, 86:051701(R), 2012.

[35] R. Agnese et al. (CDMS Collaboration). Dark Matter Search Results Using the Silicon Detectors of CDMS II. *arXiv:1304.4279*, 2013.

[36] G. Angloher et al. Results from 730 kg days of the CRESST-II Dark Matter search. *EPJ C*, 72, 2012.

[37] S. Archambault et al. Dark Matter Spin-Dependent Limits for WIMP Interactions on 19-F by PICASSO. *Phys. Let. B*, 682:185–192, 2009.

[38] M. Felizardo et al. (The SIMPLE Collaboration). Final Analysis and Results of the Phase II SIMPLE Dark Matter Search. *PRL*, 108:201302, 2012.

[39] E. Behnke et al. (COUPP Collaboration). Improved Limits on Spin-Dependent WIMP-Proton Interactions from a Two Liter CF3I Bubble Chamber. *PRL*, 106:021303, 2010.

[40] K. Abe. Light WIMP search in XMASS. *Phys. Let. B*, 719:78–82, 2013.

[41] M. G. Boulay. DEAP-3600 Dark Matter Search at SNOLAB. *Proceedings of the TAUP2011 Conference*, 2012.

[42] A. Hime. The MiniCLEAN Dark Matter Experiment. *Proceedings of the DPF-2011 Conference*, 2011.

[43] E. Aprile et al. (XENON100). Dark Matter Results from 225 Live Days of XENON100 Data. *PRL*, 109:181301, 2012.

[44] E. Aprile et al. (XENON100). Limits on spin-dependent WIMP-nucleon cross sections from 225 live days of XENON100 data. *arxiv:1301.6620*, 2013.

[45] D. Yu. Akimov et al. WIMP-nucleon cross-section results from the second science run of ZEPLIN-III. *Phys. Let. B*, 709:14–20, 2012.

[46] D. S. Akerib et al. The Large Underground XENON (LUX) Experiment. *NIM A*, 704:111–126, 2013.

[47] A. Wright. The DarkSide Program at LNGS. *Proceedings of the DPF-2011 Conference*, 2011.

[48] E. Aprile et al. (XENON100). The XENON100 Dark Matter Experiment. *Astropart. Phys.*, 35:573–590, 2012.

[49] E. Aprile and T. Doke. Liquid xenon detectors for particle physics and astrophysics. *Rev. Mod. Phys.*, 82:2053, 2010.

[50] E. Aprile et al. Simultaneous Measurement of Ionization and Scintillation from Nuclear Recoils in Liquid Xenon for a Dark Matter Experiment. *Phys. Rev. Lett.*, 97:081302, 2006.

[51] E. Aprile et al. (XENON100). Dark Matter Results from 100 Live Days of XENON100 Data. *PRL*, 107:131302, 2011.

[52] E. Aprile et al. (XENON100). Analysis of the XENON100 Dark Matter Search Data. *arxiv:1207.3458*, 2012.

[53] R. Brun and F. Rademakers. ROOT – An object oriented data analysis framework. *NIM A*, 289:81–86, 1997.

[54] E. Aprile et al. (XENON100). First Dark Matter Results from the XENON100 Experiment. *PRL*, 105:131302, 2010.

[55] C. Savage et al. Compatibility of DAMA/LIBRA dark matter detection with other searches. *JCAP*, 0904:010, 2009.

[56] C. E. Aalseth et al. (CoGeNT Collaboration). Results from a Search for Light-Mass Dark Matter with a P-type Point Contact Germanium Detector. *PRL*, 106:131301, 2011.

[57] Z. Ahmed et al. (CDMS Collaboration). Results from the Final Exposure of the CDMS II Experiment. *Science*, 327:1619, 2010.

[58] Z. Ahmed et al. (CDMS Collaboration). Results from a Low-Energy Analysis of the CDMS II Germanium Data. *PRL*, 106:131302, 2011.

[59] J. Angle et al. (XENON10 Collaboration). Search for Light Dark Matter in XENON10 Data. *PRL*, 107:051301, 2011.

[60] J. Behnke et al. (COUPP Collaboration). First dark matter search results from a 4-kg CF_3I bubble chamber operated in a deep underground site. *PRD*, 86:052001, 2012.

[61] A. Fowlie et al. (The BayesFITS Group). Constrained MSSM favoring new territories. The impact of new LHC limits and a 125 GeV Higgs boson. *PRD*, 86:075010, 2012.

[62] O. Buchmueller et al. Higgs and Supersymmetry. *arXiv:1112.3564*, 2011.

[63] C. Strege et al. Updated global fits of the cMSSM including the latest LHC SUSY and Higgs searches and XENON100 data. *JCAP*, 1203:030, 2012.

[64] J. Menéndez et al. Spin-dependent WIMP scattering off nuclei. *PRD*, 86:103511, 2012.

[65] The XENON Collaboration.

[66] P. Beltrame. Direct Dark Matter search with the XENON program. *Proceedings of the Moriond 2013 EW Session*, 2013.

[67] L. Baudis. DARWIN: dark matter WIMP search with noble liquids. *PoS (IDM2010)*, 122, 2010.

[68] A. Badertscher et al. ArDM: first results from underground commissioning. *JINST*, 8:C09005, 2013.

[69] A. Manalaysay. *Response of liquid xenon to low-energy ionizing radiation and its use in the xenon10 dark matter search.* PhD thesis, University of Florida, 2009.

[70] S.-C. Wu. Nuclear Data Sheets for A = 214. *Nuclear Data Sheets*, 110:681–748, 2009.

[71] A. L. Nichols. Tl-208. *Table of Radionuclides*, 2:147–154, 2004.

[72] R. G. Helmer and V. P. Chechev. Cs-137. *Table of Radionuclides*, 3:91–98, 2006.

[73] R. G. Helmer and E. Schönfeld. Mn-54. *Table of Radionuclides*, 1:71–76, 2004.

[74] A. Pearce. Ac-228. *Table of Radionuclides*, 6:139–164, 2011.

[75] R. G. Helmer. Co-60. *Table of Radionuclides*, 3:23–28, 2006.

[76] X. Mougeot and R. G. Helmer. K-40. *Table of Radionuclides*, 5:7–12, 2010.

[77] Yu. Khazov et al. Nuclear Data Sheets for A = 131. *Nuclear Data Sheets*, 107:2715–2930, 2006.

[78] Y. Tendow. Nuclear Data Sheets for A = 129. *Nuclear Data Sheets*, 77:631–770, 1996.

[79] E. Aprile et al. (XENON100). Study of the electromagnetic background in the XENON100 experiment. *PRD*, 83:082001, 2011.

[80] A. Kish. *Dark Matter Search with the XENON100 Experiment.* PhD thesis, Universität Zürich, 2011.

[81] E. Aprile et al. (XENON100). Material screening and selection for XENON100. *Astropart.Phys.*, 35:43–49, 2011.

[82] N. Ackerman et al. (EXO collaboration). Observation of Two-Neutrino Double-Beta Decay in ^{136}Xe with the EXO-200 Detector. *PRL*, 107:212501, 2011.

[83] Burle Industries Inc. Photomultiplier Handbook, 1989.

[84] Hamamatsu Photonics K. K. Photomultiplier Tubes, Basics and Applications, edition 3a, 2007.

[85] Photonis. Photomultiplier tubes basics.

[86] A. Einstein. Über einen die Erzeugung und Verwandlung des Lichtes betreffenden heuristischen Gesichtspunkt. *Ann. Phys.*, 322:132–148, 1905.

[87] L. Austin and H. Starke. Ueber die Reflexion der Kathodenstrahlen und eine damit verbundene neue Erscheinung secundärer Emission. *Ann. Phys.*, 314:271–292, 1902.

[88] L. Baudis et al. Performance of the Hamamatsu R11410 Photomultiplier Tube in Cryogenic Xenon Environments. *JINST*, 8:P04026, 2013.

[89] R. Santorelli et al. Characterization of the metal channel photomultipliers for the XENON100 detector. XENON100 internal note, not published.

[90] E. Brown. *Search for Low Mass Dark Matter with the XENON100 Experiment and Simulations for 1 ton and 10 ton Dark Matter Detectors*. PhD thesis, University of California, Los Angeles, 2010.

[91] HAMAMATSU. Photomultiplier Tube R8520-06-al. Data sheet.

[92] M. Schumann. Estimation of Pile-Up Background. XENON100 internal note, not published.

[93] HAMAMATSU. Private communication.

[94] K. Lung et al. Characterization of the Hamamatsu R11410-10 3-Inch Photomultiplier Tube for Liquid Xenon Dark Matter Direct Detection Experiments. *arxiv:1202.2628*, 2012.

[95] L. Baudis et al. Gator: a low-background counting facility at the Gran Sasso Underground Laboratory. *JINST*, 6:P08010, 2011.

[96] A. J. Melgarejo Fernandez. PMT linearity. XENON100 internal note, not published.

[97] T. Marrodán Undagoitia. Requirements for the R11410 base design. XENON1T internal note, not published.

[98] M. Friend et al. An LED pulser for measuring photomultiplier linearity. *arXiv:1108.3096*, 2011.

[99] HAMAMATSU. Photomultiplier Tube R11410. Data sheet.

[100] H. Neder et al. Low level γ-ray germanium-spectrometer to measure very low primordial radionuclide concentrations. *Applied Radiation and Isotopes*, 53:191–195, 2000.